Influence of Chemical Modifications on Intermolecular Ordering and Orientation in Semiconducting Polymers

Dissertation

zur Erlangung des
Doktorgrades der Naturwissenschaften (Dr. rer. nat.)

der
Naturwissenschaftlichen Fakultät II
Chemie, Physik und Mathematik

der Martin-Luther-Universität
Halle-Wittenberg,

vorgelegt von

Robert Thomas Kahl

geb. am - in -

Contents

1. Introduction

The discovery of semiconductivity in the conjugated polymer polyacetylene by Shirakawa and coworkers in 1977 [1] was the starting point for a whole new field of research: organic semiconducting polymers. For their groundbreaking discovery and their further research in this field Shirakawa, MacDiarmid and Heeger were awarded with the Nobel Prize in Chemistry in the year 2000. The significant interest in semiconducting polymers is motivated by their unique combination of chemical, mechanical and electrical properties that make them suitable for many different applications. Some of these applications are organic field effect transistors (OFET) [2, 3, 4], organic photovoltaic (OPV) devices [5, 6], organic electrochemical transistors (OECT) [7, 8] and organic light emitting diodes (OLED) [9, 10]. For these applications semiconducting polymers are regarded as a promising material to at least partially replace the classical semiconductors such as silicon and germanium due to their drastically lower melting temperatures and their solution processability that result in a significant decrease in production costs. Additionally their mechanical properties, such as light weight and flexibility, have opened new potential applications in the form of flexible and wearable electronics [11, 12, 13].

In all these applications the efficiency of the final device is strongly influenced by the charge carrier mobility in the semiconducting polymer material [14, 15]. The charge carrier mobility in turn is strongly influenced by the intermolecular ordering of the polymer chains. As described in more detail in section 2.1.2, polymers typically do not crystallize completely but instead form alternating regions of amorphous and crystalline material. The charge transport in semicrystalline conjugated polymers is mostly determined by the crystalline regions and their interconnection through so called tie chains enabling the charge transport from one crystalline region to the next [16, 17, 18].

Most semiconducting polymers have a similar chemical architecture consisting of a conjugated backbone comprised of ring or fused-ring structures, responsible for the conductive properties, and attached alkyl side chains that make the polymer soluble. Based on the similarities of their chemical structures, semiconducting polymers often also share similar motifs of intermolecular ordering. The flat and rather stiff backbones tend to stack on top of one another facilitated through π-π interactions between the aromatic rings of neighboring chains and these stacks are then separated by layers of the more flexible side chains [19, 20, 21, 22]. While the general packing motifs are similar, the specific details of the molecular arrangement, especially regarding the stacking of the backbones, can have a significant effect on the charge carrier mobility and other properties [23, 24, 25, 26]. Additionally, as the charge transport in the crystalline regions of semiconducting polymers is highly anisotropic and most of the applications

are thin film devices, the orientation of the crystals with regard to the film normal has a strong influence on the device performance [19, 27]. The most common crystal orientations found in semiconducting polymers are the so called edge-on and face-on orientations. In the edge-on orientation the side chains of the polymers are oriented parallel to the film normal, while in the face-on orientation the π-π stacking direction is parallel to the film normal. The edge-on orientation is favorable in applications that require horizontal charge transport, such as OFET devices. In contrast, the face-on orientation is more suitable for applications requiring vertical charge transport, such as OPV devices [27].
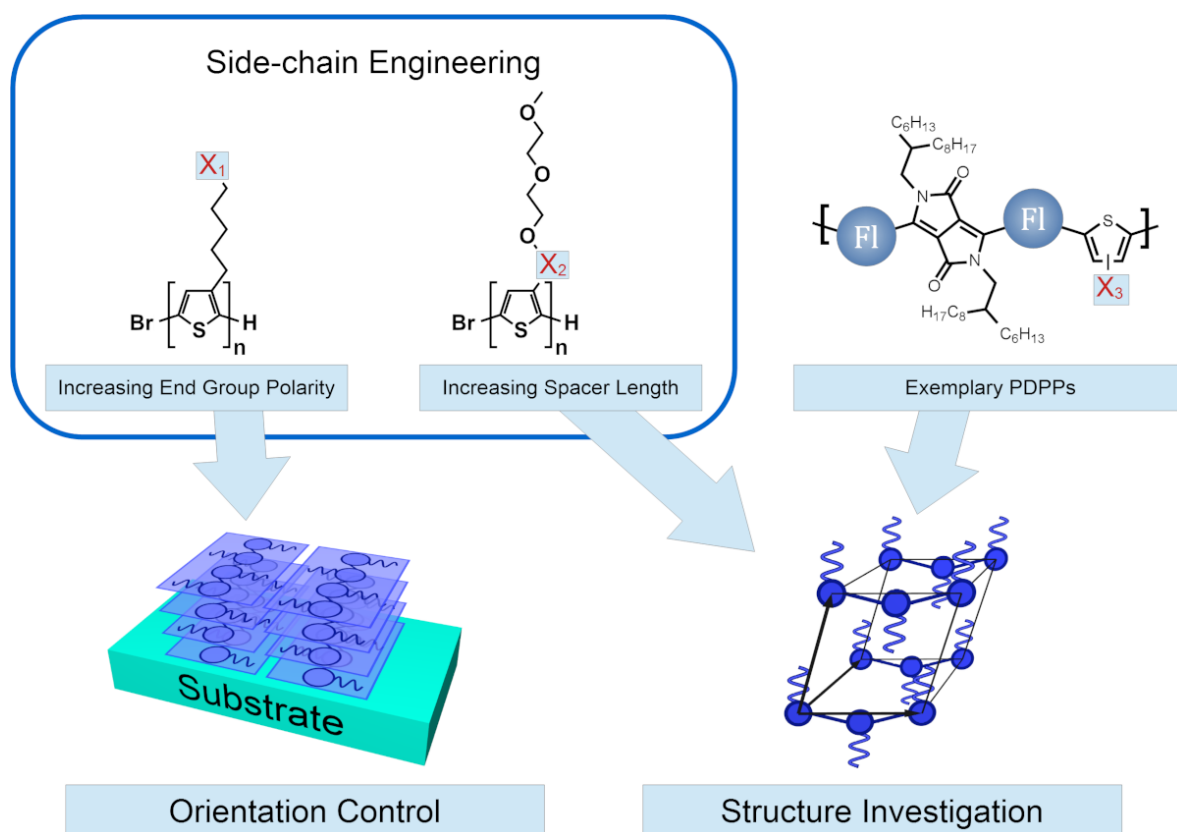
Figure 1.1.: Sketch of the chemical structure of the three investigated series of semi-conducting polymers. a) Series of P3HT derivatives with increasingly polar end groups to investigate whether the crystal orientation in thin films can be controlled by modifying the surface energy. b) Series of polythiophenes with a DEG side chain to investigate how the length of the alkyl spacer between backbone and DEG side chain influences the ordering in these polymers. c) Series of exemplary PDPPs to investigate to which extend chemical modifications influence the ordering in PDPPs.

Poly(3-hexylthiophene) (P3HT) is one of the most studied semiconducting polymers and is regarded as a good model system owing to its high thermal and chemical stability and the well established synthesis routes allowing for well defined polymers [27, 28]. Due to its low cost and constant improvements in the efficiency of P3HT based devices

[29, 30], P3HT even retains a certain relevance for commercial applications despite the fact, that by today many other semiconducting polymers exist that have significantly higher charge carrier mobilities. In chapters 4 and 5 polythiophenes are used as a model system to investigate the effect different chemical modifications of the side chains can have on the crystal structure and orientation in thin films. The first investigated series, sketched in the top left of figure 1.1, aims to introduce chemical modifications that change the preferred crystal orientation of P3HT in thin films to face-on orientaion, as strongly face-on oriented films are required for efficient OPV devices. As reported in literature, P3HT has a certain preference for edge-on orientation in thin films [19] which is induced by the interface to vacuum [31]. While certain substrates, such as graphene, can be used to induce face-on orientation in thin P3HT films, the influence of the vacuum interface always results in a certain amount of edge-on oriented crystals [32, 33, 34]. In an attempt to find an approach to suppress the formation of edge-on crystals at the interface to vacuum by increasing the surface energy associated with edge-on crystals, a series of polythiophenes with increasing polarity of the end group of the alkyl side chain is investigated. As presented in section 4, this approach is highly successful, resulting in complete face-on oriented films of up to $100\,\mathrm{nm}$ thickness on graphene substrates.

The second investigated series, sketched in the top mid of figure 1.1, consists of polythiophenes with ethylene glycol (EG) side chains intended for use in OECT devices. In this series the influence of the length of the alkyl linker connecting the EG side chain to the backbone on the crystal structure and device performance is investigated. The results presented in section 5 show that order and performance increase significantly with increasing linker length.

A group of polymers that are particularly promising for practical applications are diketopyrrolopyrrole (DPP) based copolymers as they exhibit significantly higher charge carrier mobilities than P3HT. For several PDPPs charge carrier mobilities greater than $10\,\mathrm{cm^2\,V^{-1}\,s^{-1}}$ have been reported [35, 36]. As sketched in the upper right of figure 1.1, the chemical structure of PDPP copolymers commonly consists of a DPP core with side chains enclosed by flanking units on both sides and a comonomer. Compared to P3HT, the modularity of the chemical structure of the PDPPs offers a large chemical versatility allowing to adjust their properties in a broad range by modifying flanking units, side chains, or comonomers. Within recent years a vast variety of different PDPPs has been synthesized and investigated [37]. But despite the known influence of the molecular ordering on the charge carrier mobility, structural investigations to determine the crystal lattice or liquid crystalline structure are only reported in a few cases [38, 39]. Especially the influence of the various chemical modifications on the molecular ordering is rarely addressed. Therefore, chapter 6 presents a detailed investigation of the intermolecular ordering in a series of three different PDPPs using x-ray scattering measurements.

2. Basic Concepts

This chapter is meant to give a short introduction to a series of basic concepts relevant to this dissertation. In section 2.1 the ordering of semiconducting polymers at different lengths scales is discussed. Section 2.2 gives a short overview of different processes related to ordering induced by interfaces. Finally, in section 2.3, some applications of semiconducting polymers are discussed.

2.1. Ordering in Semiconducting Polymers

2.1.1. Intermolecular Ordering

Most semiconducting polymers share a rather similar molecular architecture consisting of a usually stiffer backbone with attached flexible side chains. The conjugated backbone is responsible for the semiconducting properties of the polymer and often consists of ring or fused ring structures. The side chains are necessary to increase the solubility of the polymers and often consist of short alkyl or ethylene glycol chains that can be linear or branched. The backbone is usually much thinner than it is wide, thus giving the polymer a rather flat cross section. In combination with their chain like nature, semiconducting polymers therefore have a ribbon or "board-like" shape.

As reported in literature, "board-like" polymers can arrange in different phases ranging from biaxial nematic liquid crystalline phases (N_b) to various sanidic liquid crystalline phases (Σ) to complete 3D crystalline [40, 41, 42]. The sanidic liquid crystalline phases were first observed and classified by Ringsdorf and coworkers while investigating polyesters and polyamides [43, 44, 45]. However, it has recently been shown both through experiments [46, 42] and simulations [47, 48, 49] that the same kind of liquid crystalline mesophases can also be found in "board-like" conjugated polymers.

Sketches of the ordered arrangement of "board-like" polymer chains in the different sanidic liquid crystalline phases in comparison to the biaxial liquid crystalline and the crystalline phase are shown in figure 2.1.

In the crystalline state the "board-like" backbones of the polymers are stacked on top of one another. The regular stacking of the backbones is facilitated by π-π-interactions between π-orbitals of neighboring backbones and is therefore commonly referred to as π-π-stacking. Neighboring "stacks" of backbones are separated by layers of side chains. In the crystalline state, any shifts between neighboring "stacks" against one another are regular and periodic. In contrast, in the sanidic rectangular liquid crystalline phase neighboring "stacks" are shifted randomly against one another. Thus, while there is still a periodic arrangement of "stacks" of backbones separated by layers of side chains,
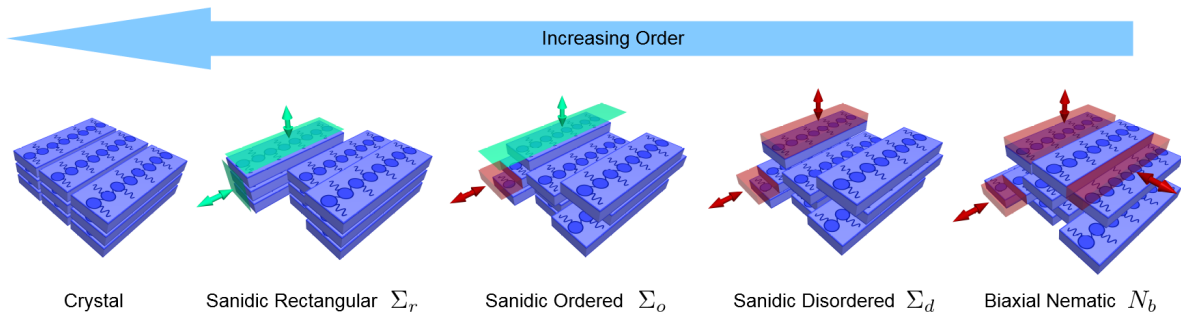
Figure 2.1.: Sketches illustrating the intermolecular arrangement of "board-like" polymers in the crystalline phase and in various liquid crystalline mesophases. In all illustrated phases, except for the biaxial nematic phase, the backbones of the chains stack on top of one another. The regularity of the arrangement of neighboring "stacks" and of neighboring chains within the same "stack" vary in the different phases. Green arrows indicate random shifts of neighboring "stacks" against one another. Red arrows indicate random shifts of chains within the same "stack" against one another.

there is no positional correlation of chains in different "stacks". However, chains within the same stack are arranged in a periodic fashion basically forming a two dimensional crystal.

In the sanidic ordered phase the regular arrangement of chains within the same stack is partially lost. While the chains within the same stack are still regularly spaced in the stacking direction, they are randomly shifted against one another in chain direction.

In the sanidic disordered phase the backbones of the chains are still arranged in layers but the regular spacing in stacking direction is lost. Thus, while there is still a periodic arrangement of alternating side chain and backbone layers, the positions of neighboring backbones within one layer are completely uncorrelated.

In the biaxial nematic phase the backbones are no longer arranged in "stacks" or layers and neighboring chains are shifted against one another by a random distance in all three dimensions. Thus, the ordering is purely orientational as the "board-like" backbones are still parallel to one another and are oriented in the same direction. As shown by Ebert at al. the different forms of sanidic mesophases can be differentiated based on their x-ray scattering pattern [45].

2.1.2. Semicrystalline Morphology in Polymers

This section is intended to give a short introduction to the semicrystalline morphologies found in semicrystalline polymers on different length scales. A more in-depth discussion of these morphologies and related aspects can be found in various textbooks, for example in the references [50, 51, 52] on which this section is based on.

As sketched in figure 2.2a) polymer chains in the molten state adopt a coil conformation. The contour of an individual chain in the melt can be described by a random
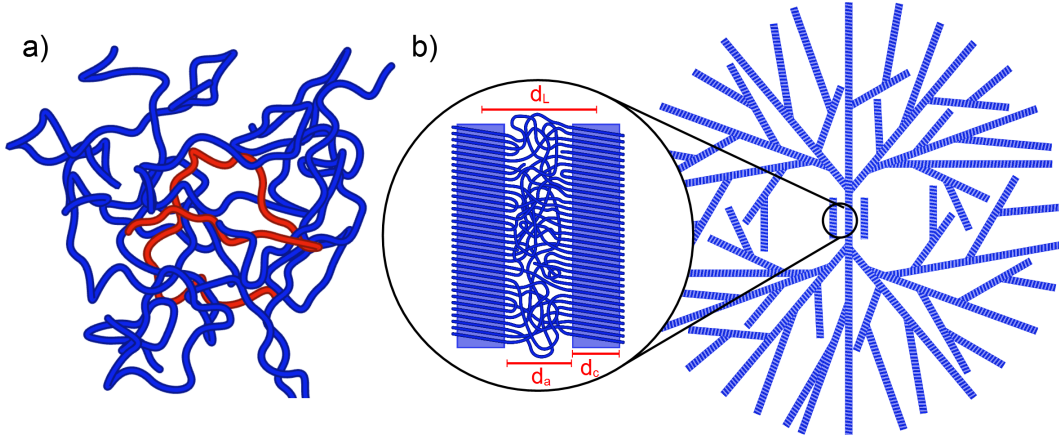
Figure 2.2.: Sketch of a) coiled state of polymers in melt and b) semicrystalline morphology and spherulite superstructures that can be found in crystallizable polymers. For better visibility a single chain in a) is highlighted in red.

walk. As seen from the sketch, the coils of different chains in the melt are spatially not separated and instead mutually interpenetrate each other.

Upon cooling a polymer melt below the melting temperature, the polymer may crystallize. However, unlike small molecules, polymers do not crystallize completely and instead form a lamellar morphology of multiple parallel crystalline lamellae separated by amorphous layers as depicted in the circle in figure 2.2b). A completely crystalline polymer sample would require all chains to disentangle, fully extend and arrange in parallel. During the crystallization there is typically not enough time for the chains to resolve all entanglements. Additionally, polymers are usually polydisperse and thus all polymer samples typically contain chains of many different lengths, further preventing a complete crystallization. Furthermore, chain ends and chemical defects usually cannot be included into a regular crystalline structure and thus have to be expelled into the amorphous regions upon crystallization. The resulting lamellar structure can be characterized by the thickness of the amorphous layer d_a, the thickness of the crystalline layer d_c and the resulting long period d_L:

$$d_L = d_c + d_a \qquad (2.1)$$

The long period is usually in the order of a few $10\,\mathrm{nm}$. The lamellar morphology can therefore be observed in atomic force microscopy (AFM) measurements.

The degree of crystallinity χ_c of a polymer sample can be expressed in terms of a mass fraction:

$$\chi_c = \frac{m_c}{m} \qquad (2.2)$$

where m_c is the mass of the crystalline parts of the sample and m is the total mass of the sample.

The growth of crystalline lamellae generally occurs in the lateral directions. In comparison, the thickness of the lamellae stays rather constant, although a certain limited

thickening of lamellae can occur in some cases [53, 54]. Additionally, there is a tendency of new crystal lamellae forming parallel to already existing ones resulting in stacks of lamellae [55, 56]. Branching and splaying upon further growth of the crystalline lamellae results in the formation of spherical superstructures, so-called spherulites (cf. fig. 2.2b). Spherulites are optically anisotropic and can grow upto several μm in size. In polarized optical microscopy (POM) images spherulites show characteristic Maltese cross patterns.

2.1.3. Crystal Orientation in Thin Films

Organic electronic devices employing semiconducting polymers as active material are typically thin film devices supported on some kind of substrate. Owing to the anisotropy of the crystal structures, the charge transport properties of semiconducting polymers in the crystalline state are also anisotropic. Consequently, the orientation of the crystals of the semiconducting polymers in the active layer of the electronic devices can have a significant influence on the performance of these thin film devices [19].
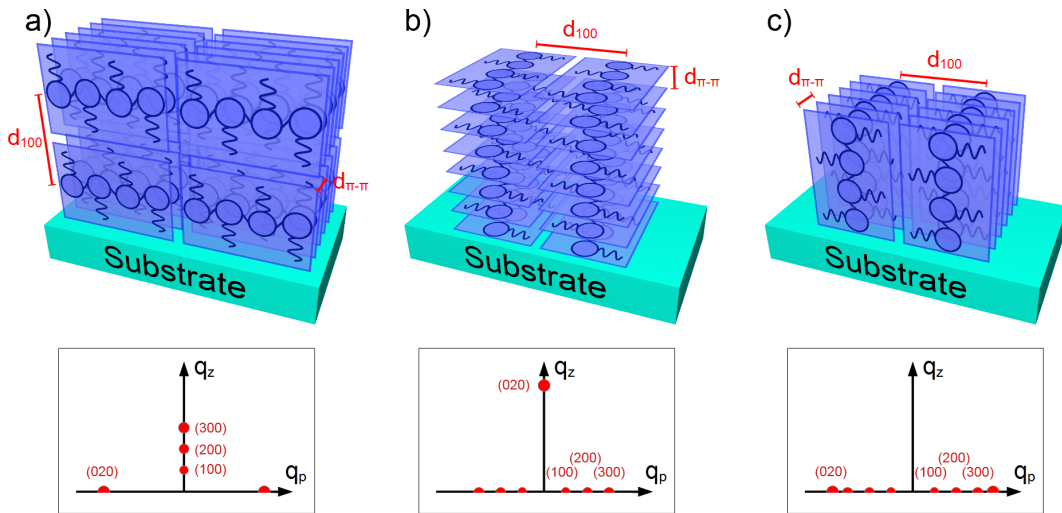
Figure 2.3.: Sketch of the three distinct crystal orientations found in thin films of conjugated polymers and corresponding scattering patterns in reciprocal space as would be observed in GIWAXS measurements. a) In edge-on orientation the side chains are oriented normal to the substrate. b) In face-on orientation the π-π-stacking direction is oriented normal to the substrate. c) In chain-on orientation the polymer backbone is oriented normal to the substrate.

Due to the large surface to volume ratio found in thin films, the distribution of crystal orientations in thin films is often defined by interface induced crystallization phenomena (cf. section 2.2). As sketched in figure 2.3 one typically differentiates between three different crystal orientations. In the edge-on orientation the polymer backbones are parallel to the substrate while the side chains are roughly perpendicular to the substrate. In the face-on orientation both the backbones and the side chains are parallel to the substrate, while in the chain-on orientation the backbones are perpendicular to the

substrate. The different crystal orientations can be identified by performing grazing incidence wide angle x-ray scattering (GIWAXS) measurements as described in section 3.4.4. The scattering patterns that would be observed for the different orientations in GIWAXS measurements are also illustrated in figure 2.3.

In general the charge transport in semiconducting polymers can be separated into intrachain and interchain transport. The intrachain transport occurs along the conjugated backbone, while the interchain transport occurs along the π-π-stacking direction enabled by overlap of electronic orbitals of neighboring chains [57]. The charge transport along the backbone has been shown to be significantly faster than the transport along the π-π-stacking direction [58, 59]. Consequently, for applications that require horizontal charge transport the edge-on crystal orientation is ideal as in this orientation both the backbones and the π-π-stacking direction are parallel to the substrate. While the chain-on orientation would be beneficial for applications requiring vertical charge transport, it is rarely observed and considered rather difficult to induce [57, 60, 61]. Therefore, one typically strives to achieve a dominant face-on orientation instead when vertical charge transport is required [60].

2.2. Interface Induced Crystallization

In most cases crystallization of a melt occurs at the interface to a foreign substance. Interfaces can induce crystallization either by heterogeneous nucleation, by prefreezing or by surface freezing. This section is intended to give a short overview over these different mechanisms. A more thorough discussion of classical nulceation theory can for example be found in the books by Markov [62] and Kalikmanov [63], while a discussion of prefreezing and surface freezing can be found in references [64] and [65] respectively.

2.2.1. Classical Nucleation Theory

If the melt of a crystallizable material is cooled below the melting temperature T_m, the crystalline phase will have a lower free energy than the melt. The formation of a small crystal within the bulk of the melt is called homogeneous nucleation. As illustrated in figure 2.4a), any local formation of a new crystalline phase, i.e. a nucleus, within the melt also results in the formation of an interface between the crystalline phase and the melt. Consequently, the change in free energy ΔG upon the formation of a nucleus of spherical shape has a contribution that is proportional to the volume and a contribution that is proportional to the surface area:

$$\Delta G = -\frac{4}{3}\pi r^3 \Delta g + 4\pi r^2 \gamma_{cm} \tag{2.3}$$

where r is the radius of the nucleus, Δg is the difference in free energy per unit volume between crystal and melt and γ_{cm} is the interfacial energy of the interface between crystal and melt. A plot of ΔG and its individual contributions as functions of r are shown in 2.4c). As seen from the plot, $\Delta G(r)$ has a maximum of height ΔG^* that acts
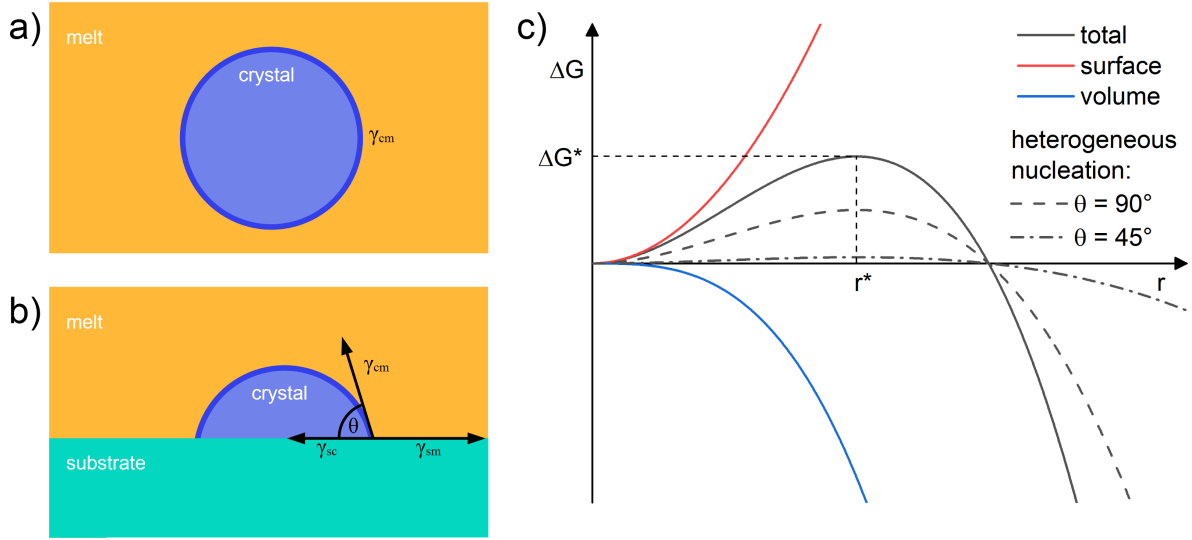
Figure 2.4.: Sketch of a) homogeneous and b) heterogeneous nucleation modeled by a spherical cap on a flat substrate. c) Graph of the free energy change ΔG upon formation of a nucleus with a certain radius r. The red and blue curves show the surface and volume contributions to the total ΔG respectively. The dashed lines show the total free energy change for heterogeneous nucleation for two different contact angles.

as an energy barrier for crystallization. Nuclei with a radius r smaller than the critical radius r^* are inherently unstable and can not grow, as any small increase in r would result in an increase of ΔG. In contrast, nuclei with $r > r^*$ can grow freely, as any further growth will result in a reduction of ΔG.

The height of the energy barrier can be reduced by nucleation at at the interface to a solid substrate. A scheme of this so-called heterogeneous nucleation is shown in figure 2.4b). For heterogeneous nucleation the nucleus can be modeled as a spherical cap and has a certain contact angle Θ with the substrate. According to Young's equation the contact angle is determined by:

$$\gamma_{sm} = \gamma_{sc} + \gamma_{cm} \cos(\Theta) \tag{2.4}$$

where γ_{sm} is the interfacial energy of the interface between the substrate and the melt and γ_{sc} is the interfacial energy of the interface between substrate and crystal. For heterogeneous nucleation on a flat substrate, the height of the energy barrier ΔG^*_{het} is given by [63]:

$$\Delta G^*_{het} = \Delta G^*_{hom} \frac{2 - 3\cos(\Theta) + \cos^3(\Theta)}{4} \tag{2.5}$$

where ΔG^*_{hom} is the height of the energy barrier in the case of homogeneous nucleation. The value of the fraction in equation 2.5 varies between 0 and 1 depending on the contact angle Θ. In case of nonwetting ($\Theta = 180°$) the fraction is equal to 1 and the energy barrier is the same as in the case of homogeneous nucleation. All contact angles

$\Theta < 180°$ lead to a reduction of ΔG_{het}^*. The plots of $\Delta G(r)$ for $\Theta = 90°$ and $\Theta = 45°$ are also shown in 2.4c). In general, the reduction of the energy barrier results in an increased nucleation rate. As the extent of the reduction depends on Θ which in turn is defined by the relationship of the different interfacial energies, the nucleation rate in the case of heterogeneous nucleation also depends on the interfacial energies.

2.2.2. Prefreezing and Surface Freezing

Another crystallization phenomenon observed at the interface to a solid substrate is the so-called prefreezing. Prefreezing describes the stabilization of a thin crystalline layer at the interface to a solid substrate to temperatures above the bulk melting point T_m [66]. The formation of a prefrozen layer on a substrate results in the replacement of the single substrate-melt interface with a substrate-crystal and a crystal-melt interface. As the crystal phase is thermodynamically unfavorable for $T > T_m$ prefreezing can only occur when the replacement of the melt-substrate interface by the two other interfaces is energetically favorable:

$$\gamma_{sm} > \gamma_{sc} + \gamma cm \qquad (2.6)$$

where γ_{sm}, γ_{sc} and γcm are the interfacial energies of the substrate-melt, substrate-crystal and a crystal-melt interfaces respectively. The difference between the interfacial energies $\Delta\gamma = \gamma_{sm} - (\gamma_{sc} + \gamma cm)$ determines both the maximum temperature T_{max} at which the crystal layer is stable and the thickness of the crystal layer [64]. Also note, that unlike heterogeneous nucleation, which is an activated process, prefreezing is an equilibrium phenomneon.

Observations somewhat similar to prefreezing have been reported in films of short normal alkanes and alcohols, where the vacuum interface induces the formation of a thin crystalline layer on top of the melt above the bulk freezing temperature [67, 68, 69]. This phenomenon has been termed surface freezing. Furthermore, a layer of increased order at the interface to vacuum has also been observed in polyacrylates [70, 71, 72, 73].

Tkachenko and Rabin proposed that the thin crystalline layer observed at the interface to vacuum in surface freezing is stabilized mainly by an energy gain Δ associated with disorder or fluctuations of the molecules in this layer, as they are less constrained than in the bulk [74, 75, 76]. According to their theory, surface freezing occurs if $\delta\gamma - \Delta < 0$, where $\delta\gamma = \gamma_{sv} + \gamma_{sl} - \gamma_{lv}$ is the difference of the surface free energies of the solid-vapor (γ_{sv}), the solid-liquid(γ_{sl}) and the liquid-vapor (γ_{lv}) interfaces. In contrast, Sirota et al. proposed to model surface freezing as a wetting of the melt by a crystalline layer [77]. According to their model surface freezing occurs when $\delta\gamma < 0$ and thus only depends on the surface free energies. The debate regarding these two models of surface freezing is still ongoing [65]. In any case, the occurrence of surface freezing at the interface to vacuum clearly depends on the relation of the involved surface free energies.

2.3. Applications of Semiconducting Polymers

This section aims to give a short introduction to the various organic electronic devices mentioned throughout this dissertation. These are organic photovoltaic (OPV) devices, organic field effect transistors (OFET) and organic electrochemical transistors (OECT). A more in depth discussion of the different devices can be found in the different textbooks and review papers the following sections are based on (OPV: [78, 79, 27, 80],OFET: [78, 79, 27],OECT: [7, 81]).

2.3.1. Organic Photovoltaic Devices

The active layer of organic photovoltaic (OPV) devices typically consists of two different organic materials: an electron-rich (donor) and an electron-poor (acceptor) semiconducting material. In organic semiconductors the photoexcitation by incident light creates tightly bound exciton states instead of free charge carriers. These excitons can be effectively separated into holes and electrons at the interface between donor and acceptor materials. The excitons have a relatively short life time before recombining (ps to ms). Thus, efficient charge generation requires, that for all positions throughout the active layer the distance to the nearest donor-acceptor interface is comparable to the exciton diffusion length. Such nanostructured morphologies are commonly achieved through phase separation of a mixture of two different materials. The spontaneous phase separation of the donor and acceptor materials ideally results in the self-assembly of the two materials into a bicontinuous interpenetrating network with structures on the length scale of 10 nm to 20 nm. These phase separated structures are commonly referred to as bulk heterojunctions (BHJ).
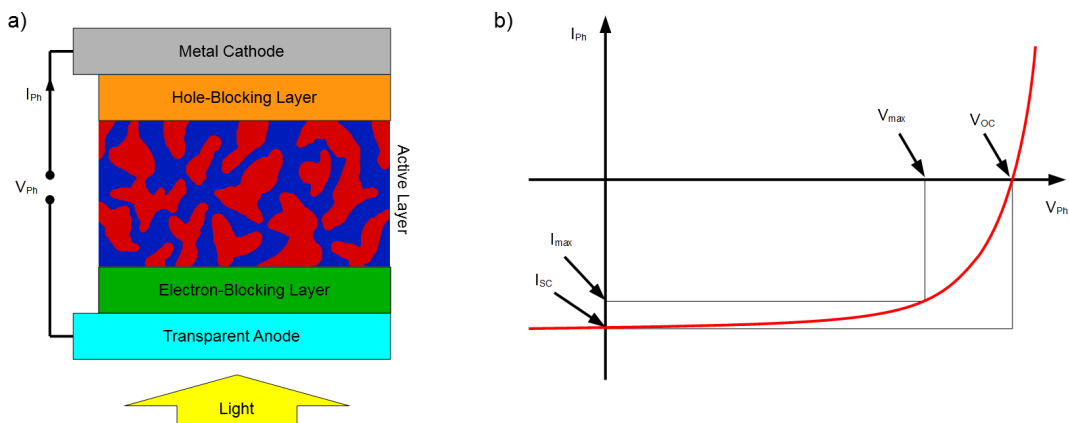

Figure 2.5.: a) Sketch of a bulk heterojunction organic photovoltaic device. b) Current versus voltage plot for an organic photovoltaic device. I_{max} and V_{max} are defined by the point on the curve that results in the largest power output $P_{max} = I_{max} \cdot V_{max}$. The short-circuit current density I_{SC} and the open-circuit voltage V_{OC} are indicated as well.

A sketch of a BHJ organic photovoltaic device is given in figure 2.5a). In the simplest case an organic photovoltaic devices consist of a layer of active material sandwiched in between a transparent anode, often made from indium tin oxide (ITO) coated glass, and a metal cathode. Inserting additional interfacial layers between the active material and the electrodes can have various beneficial effects [82, 83]. For example, the addition of hole- and electron-blocking layers will increase the charge selectivity of the electrodes and thereby improve the charge extraction as the flow of charge carriers in the unfavored direction is hindered. Furthermore, interfacial layers can minimize the energy barrier for charge injection and extraction.

As seen from the sketch, OPV devices require vertical charge transport within the active layer and therefore benefit from a dominant face-on crystal orientation [84, 85]. Figure 2.5b) shows a typical current versus voltage curve of an OPV device and indicates some of the important parameters. The maximum power point is the point (V_{max}, I_{max}) along the curve for which the produced power becomes maximum. The short circuit current I_{SC} depends on the quantum efficiency of charge separation and the amount of charge carriers that reach the electrodes. Hence, the I_{SC} also depends on the mobility μ of the charge carriers and their lifetime τ before recombination [86, 79]. The open circuit voltage V_{OC} depends on the electronic structure of the donor and acceptor materials [79].

The ratio of the two areas in the I/V-curve defined by $V_{OC} \cdot I_{SC}$ and $V_{max} \cdot I_{max}$ defines the so called fill factor (FF):

$$FF = \frac{I_{max} \cdot V_{max}}{I_{SC} \cdot V_{OC}} \tag{2.7}$$

Based on the fill factor, the power conversion efficiency (PCE) of an OPV device can be expressed as:

$$PCE = \frac{P_{out}}{P_{in}} = \frac{I_{SC} \cdot V_{OC} \cdot FF}{P_{in}} \tag{2.8}$$

where P_{in} is the power of the incident light and P_{out} is the electrical power produced by the photovoltaic cell.

Within the last few years the PCEs of OPV devices have increased significantly and are currently approaching 20% for small area cells ($<1\,cm^2$) and reaching 14.5% for large area cells ($>200\,cm^2$) [87, 88].

While the PCEs of OPV devices are still lower than the PCEs of their inorganic counterparts, they potentially offer many other advantages. For example flexibility, lower weight and potentially significantly lower production costs if solution based printing processes can be realized.

2.3.2. Organic Field Effect Transistors

Organic field effect transistors (OFET) are thin film transistors (TFT) in which a thin film of an organic semiconducting material (e.g. a conjugated polymer) forms
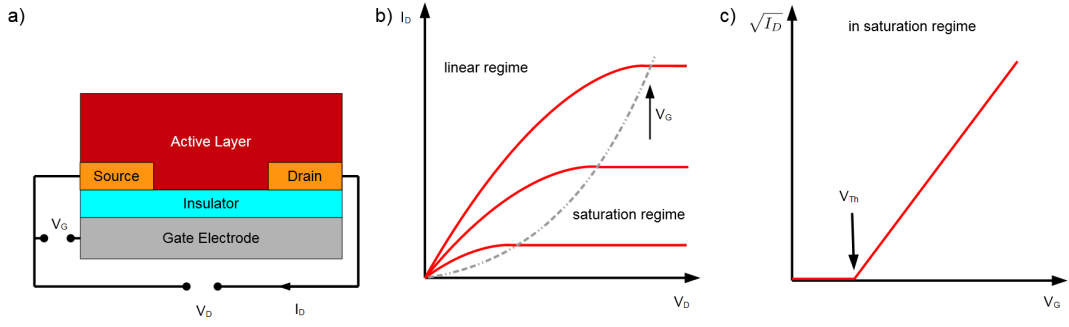
Figure 2.6.: a) Sketch of an organic field effect transistor (OFET) in bottom gate/bottom contact geometry. b) Output characteristics of an OFET. The dashed line indicates the beginning of the saturation regime, in which the source-drain current I_D is independent of the drain voltage V_D. c) Plot of the square root of the source-drain current I_D in the saturation regime as a function of the gate voltage V_G.

the active layer. Figure 2.6a) shows a sketch of an OFET in bottom gate/bottom contact geometry. As seen from the sketch, both gate voltage V_G and drain Voltage V_D are defined with respect to the source electrode. Applying a gate voltage V_G to the device, an accumulation layer develops at the interface between insulator and organic semiconductor, resulting in the formation of a conducting channel between source and drain electrode. Note that the accumulation layer usually only extends a few molecular layers from the insulator-semiconductor interface. However, typically there is a finite number of trap states that has to be filled up first before a conducting channel can form. Consequently, there is a certain threshold voltage V_{th} that the gate voltage V_G has to surpass before a noteworthy source-drain current I_D can flow.

Figure 2.6b) shows typical output characteristics of an OFET at different applied gate voltages $V_G > V_{Th}$. For drain voltages $V_D << V_G$ the source-drain current I_D is proportional to V_D. This is the so-called linear regime. In the linear regime the source-drain current is approximately given by the following equation:

$$I_D = \frac{W}{L} \cdot C_i \cdot \mu \cdot (V_G - V_{Th}) \cdot V_D \tag{2.9}$$

where W and L are the width and length of the channel, C_i is the insulator capacitance per unit area and μ is the charge carrier mobility. If the drain voltage is increased until $V_D > V_G - V_{Th}$ a depletion region is formed near the drain contact and the conducting channel is "pinched off" and the OFET operates in the so-called saturation regime. In the saturation regime the source-drain current is independent of the drain voltage V_D:

$$I_D = \frac{W}{2L} \cdot C_i \cdot \mu \cdot (V_G - V_{Th})^2 \tag{2.10}$$

By plotting the square root of I_D in the saturation region as a function of the gate voltage V_G, as shown in figure 2.6c), the charge carrier mobility μ can be extracted from

the slope of the resulting curve. Additionally, the threshold voltage V_{Th} is given by the intersect of the curve with the x-axis. However, in real devices the curve is typically rounded off in the region around V_{Th} and V_{Th} has to be determined by interpolating the linear part of the curve to $\sqrt{I_D} = 0$. Another important parameter in the operation of an OFET is the transconductance g_m that describes the response of I_D to a change in V_G. In the saturation regime the transconductance is given by:

$$g_m = \frac{\partial I_D}{\partial V_G} = \frac{W}{L} \cdot C_i \cdot \mu \cdot (V_G - V_{Th}) \tag{2.11}$$

While OFETs have slower switching speeds and lower charge carrier mobilities than their inorganic counterparts, they offer similar advantages as the ones also mentioned for OPVs, i.e. mechanical flexibility, lower weight and solution-based processing of devices [4, 89].

2.3.3. Organic Electrochemical Transistors
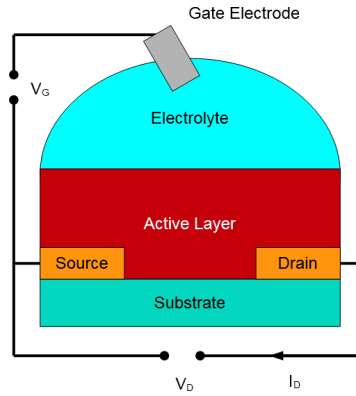
Figure 2.7.: Sketch of an organic electrochemical transistor (OECT).

Figure 2.7a) shows a sketch of an organic electrochemical transistor (OECT). Similar to OFETs, OECTS also feature a thin film of a semiconducting organic material supported on a substrate and contacted through source and drain electrodes. In contrast to OFETs, the gate electrode in OECTs is immersed in an electrolyte which in turn is in contact with the semiconducting layer. Upon application of a gate voltage V_G ions are injected from the electrolyte into the active layer, which changes the doping state and thus also the conductivity of the active layer. Therefore, the active layer in OECTs requires an organic mixed ionic-electronic conductor (OMIEC) that efficiently transports both ionic and electronic charges [90]. Furthermore, the active material should not dissolve in water as most applications of OECTs are in aqueous environment.

In OECTs the doping changes of the active film caused by ion injection occur throughout the entire volume of the channel and thus the whole volume of the channel contributes to the source-drain current I_D when a drain voltage is applied V_D. This is in stark contrast to OFETs where only a thin layer of the channel at the interface between

organic semiconductor and insulator is affected by an applied gate voltage. As the transconductance of OECTs scales with width and thickness [91, 92] of the channel, OECTs can achieve significantly larger transconductance values than OFETs in similar sized devices.

Interestingly, despite the different working mechanisms of OFETs and OECTs, the overall behavior of OFETs and OECTs is quite similar. For example, the output characteristics of OFETs and OECTs show similar trends. According to the model proposed by Bernards and Malliaras [93], the electronic charge transport in OECTs can be described with the same equations also used for OFETs as long as the interfacial capacitance C_i is replaced with the volumetric capacitance C^* [81]. Consequently, the transconductance g_m of an OFET in saturation regime is given by:

$$g_m = \frac{\partial I_D}{\partial V_G} = \frac{W \cdot d}{L} \cdot C^* \cdot \mu \cdot (V_{Th} - V_G) \tag{2.12}$$

where W, L and d are the channel width, length and thickness respectively, C^* is the volumetric capacitance and μ is the charge carrier mobility. As g_m depends on the charge carrier mobility μ and the volumetric capacitance C^*, both of which are parameters of material used in the active layer, the product $\mu \cdot C^*$ is considered a figure of merit for organic mixed conductors used in OECTs [92]. The $\mu \cdot C^*$ product of a material can in principal be determined from the measured g_m of a single OECT device if the device geometry (i.e. W, L and d) is known. However, measuring multiple devices with different geometries is statistically more reliable and additionally allows to verify that devices based on the investigated material actually show a linear scaling of g_m with the channel volume. By plotting the measured g_m values against $W \cdot d \cdot L^{-1} \cdot (V_G - V_{Th})$, the $\mu \cdot C^*$ product is given by the slope of the resulting linear curve.

Resulting from the combination of ionic and electronic conduction OECTs have many different applications in bioelectronics [7, 94] such as for example stimulation and recording of electrogenic cells [95, 96] and sensing ions [97, 98], enzymes [99], glucose [100, 101] or DNA [102].

3. Experimental Methods and Sample Preparation

This chapter introduces the different experimental methods used throughout this dissertation to study the properties of the investigated semiconducting polymers in bulk and thin films. Additionally, the sample preparation procedure of thin film samples is described. The experimental methods presented here are: differential scanning calorimetry (DSC), polarized optical microscopy (POM), atomic force microscopy (AFM), wide angle x-ray scattering (WAXS) and grazing incidence wide angle x-ray scattering (GI-WAXS).

3.1. Differential Scanning Calorimetry

Differential scanning calorimetry (DSC) is a thermal analysis technique that measures the heat flow into or out of a sample allowing to identify and characterize phase transitions that occur in the sample during heating or cooling. In general one distinguishes between two different types of DSCs: heat flux DSC and power compensation DSC. As within the context of this thesis only power compensation DSCs were used, the following section focuses on this type of DSC. This sections is based on the book by Wunderlich [103] and the book by Höhne [104].
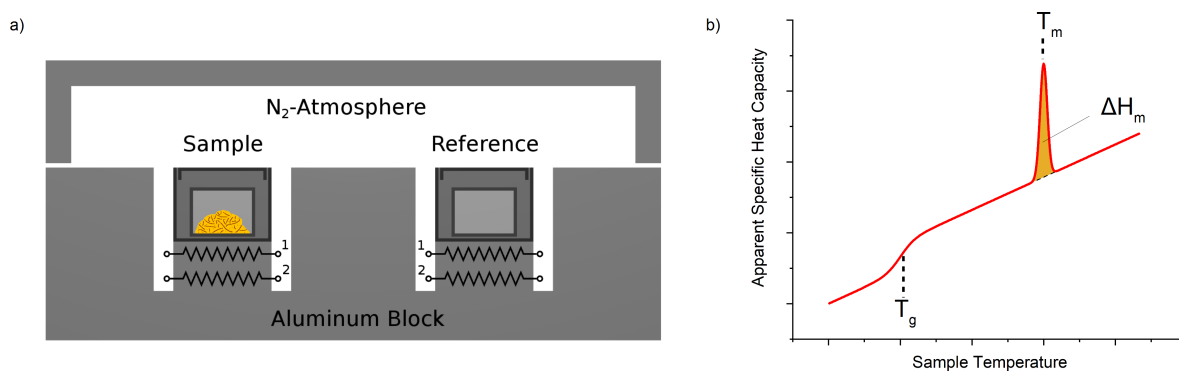
Figure 3.1.: a) Schematic drawing of a power compensation DSC. 1 - resistance thermometer, 2 - heating wire b) Sketch of a typical apparent specific heat capacity curve of a semicrystalline polymer observed during a heating run. The sketched curve shows a glass transition and a melting process.

Figure 3.1a) shows a schematic drawing of a power compensation DSC. The instrument consists of two identical, thermally decoupled microfurnaces each having their

own temperature sensor and heating resistor. The sample is encapsulated in an aluminum pan and placed in one of the microfurnaces. The other microfurnace contains a second aluminum pan with a reference material inside. The reference material should be chosen such, that it does not undergo a phase transition within the investigated temperature range. For the measurements in the context of this thesis, the reference aluminum pan was simply empty. Both furnaces are kept in an inert nitrogen atmosphere.

During a measurement the heating power of both furnaces is regulated by a controller so that their temperature follows a user defined temperature program (often simply a constant cooling or heating rate). The difference between the heating powers applied to sample and reference furnace is proportional to the additional heat flow rate ϕ into the sample furnace that is required to achieve the same heating or cooling rate β in the sample and reference furnaces. During a measurement this additional heat flow rate $\phi(T)$ is typically recorded as a function of sample temperature.

If the reference and sample furnace were absolutely symmetrical, the difference in heat flow rate could be ascribed solely to the sample. However, in any real DSC there will always be certain instrument specific asymmetries between sample and reference furnace. The influence of these asymmetries of the instrument can be compensated by measuring and subtracting a baseline $\phi_0(T)$ from the actual sample measurement. The baseline is measured using the same temperature program as the actual measurement but with both sample and reference furnace containing only an empty aluminum pan. By normalizing the resulting measurement curve, after subtraction of the baseline, by sample mass m and heating rate β one obtains the apparent specific heat capacity c_p of the sample:

$$c_p(T) = \frac{\phi(T) - \phi_0(T)}{m \cdot \beta} \tag{3.1}$$

Note, that the apparent specific heat capacity of the sample is only equivalent to the specific heat capacity of the sample in temperature regions where no thermal events occur in the sample.

As illustrated in figure 3.1b), phase transitions like melting and crystallization will result in a peak in the c_p curve. The crystallization or melting enthalpy is equivalent to the area between the peak and the c_p interpolated curve. Within this thesis the melting temperatures T_m of the investigated polymers where determined from the maximum position of the melting peaks.

DSC measurements were performed with the *PerkinElmer DSC7* and with the *PerkinElmer DSC 8000*, both of which are power compensation DSCs.

3.2. Polarized Optical Microscopy

Polarized optical microscopy (POM) is a variation of optical microscopy that uses linearly polarized light to illuminate a sample of interest. POM allows to visually observe optical anisotropic structures like liquid crystalline and crystalline phases (e.g.

spherulites) within a sample. A general introduction to POM can be found in the book by Robinson and Bradbury [105] and a more specific introduction to the application of POM to polymer samples can be found in the book by Sawyer, Grubb and Meyers [106].

In principal the polarized light optical microscope is built identical to a regular light microscopy except for the addition of two linear polarization filters. The first polarization filter which is located directly after the light source is called the polarizer, while the second polarization filter, located between the sample and the eyepiece or camera, is called the analyzer. Typically, one of the two polarization filters is rotatable. If the polarizer and analyzer are "crossed", i.e. their planes of polarization are rotated relative to one another by 90°, and there is no optical anisotropic sample present, no light from the light source will be able to pass through both polarizer and analyzer resulting in a field of view that is completely dark. However, if a sample with optically anistotropic regions is present that rotate the plane of polarization of the incident light, these regions will be visible in the image.

The POM images presented throughout this thesis were obtained using a *Olympus BX51* microscope equipped with an *Olympus XC30* digital camera. As the samples investigated in this thesis were thin films of polymers on opaque substrates, all POM images in this thesis were recorded in reflection geometry.

3.3. Atomic Force Microscopy

Atomic force microscopy (AFM) is a measurement technique that scans the surface of a sample using a sharp sampling tip supported at the end of a cantilever. There is a large variety of different AFM measurement modes available allowing to measure a variety of different properties and samples. A general introduction to AFM and an overview over some of the different measurement modes and their applications can be found in the book by Reifenberger [107] and in the book by Eaton and West [108, 107].

Figure 3.2a) schematically shows the major components of an AFM. A laser is reflected off the backside of the cantilever onto a four quadrant photodetector. This results in an optical lever that allows to accurately track the motion of the tip of the cantilever based on the position of the laser detector. The motion of the cantilever relative to the sample surface is realized using piezoelectric elements. In some measurement modes(e.g. tapping mode, peak-force tapping mode) the cantilever is forced to oscillate through an additional excitation piezoelectric element at the base of the cantilever.

The AFM images shown within this thesis were obtained using the peak-force tapping mode. In the peak-force tapping mode the maximum force (peak force) applied to the oscillating cantilever tip by the sample surface is kept constant through a feedback loop by regulating the distance between cantilever and sample surface [109]. This is in contrast to the regular tapping mode where the amplitude of the oscillating cantilever is kept constant instead. A further difference to the regular tapping mode is that in peak force tapping mode the excitation frequency of the cantilever is far below its resonance

a)

Four Quadrant
Photodetector

Laser

Excitation Piezo

Cantilever

z

x y

Piezoelectric xyz-Scanner

b)

Force F

repulsive

attractive

Peak Force

Approach

Withdraw

Adhesion

Deformation

Tip-Sample-Distance d
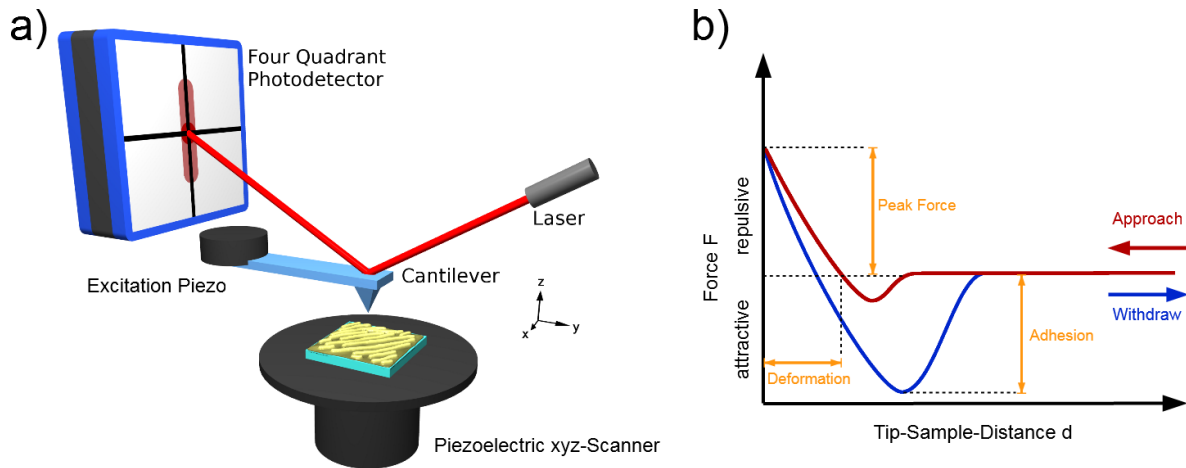
Figure 3.2.: a) Schematic diagram of the basic components of an AFM. b) Sketch of a typical force-distance curve observed in peak force tapping mode. Some of the obtainable measurement parameters are indicated. The maximum force (peak force) the cantilever tip experiences is kept constant in this measurement mode. The adhesion of the sample is given by the minium force the cantilever tip experienced. The deformtion is given by the extent the cantilever tip indented the sample surface before the peak force was reached. Figure b) based on [109] and [110]

frequency and is typically in the range of $1\,\mathrm{kHz}$ to $10\,\mathrm{kHz}$ [111]. The peak force tapping mode is well suited for measurements of soft samples as the direct control over the maximum normal force between cantilever and sample allow to minimize the damage to both the sample surface and the cantilever. Additionally, in measurements using the peak force tapping mode the force-time and force-distance curves are obtained for each oscillation period of the cantilever from which a variety of different mechanical properties of the sample surface can be extracted. This allows to map various properties of the sample surface with the same lateral resolution as the height maps. Figure 3.2b) shows a typical force-distance curve upon approach and retraction of the cantilever from a sample surface. When the cantilever tip comes close to the sample surface it will start experiencing attractive forces (e.g. van der Waals, electrostatic). Upon further approach, when the attractive forces overcome the stiffness of the cantilever, the tip will jump to contact with the surface. Upon further moving the base of the bent cantilever towards the surface the force experienced by the tip will start increasing until it is repulsive. When the specified maximum force is reached (peak force) the cantilever is retracted again. Upon retraction the tip of the cantilever will stay in contact with the substrate until the restoring forces in the cantilever (due to cantilever deflection) overcome the adhesive force. Within this thesis AFM height and adhesion images are shown. The contrast in the adhesion images is determined by the magnitude of the adhesion force observed at each point of the sample, while the contrast in the height images is determined by the height offset of the cantilever required to keep the peak

force constant.

The AFM images shown in this thesis were obtained using a *Bruker MultiMode 8 AFM* with a *Nanoscope V* controller. *ScanAsystFluid+* cantilevers (f_0 = 150 kHz, k = 0.7Nm^{-1}) from *Bruker* were used. The obtained measurement data was further processed using the open-source software Gyddion [112].

3.4. Wide Angle X-ray Scattering

3.4.1. Basics of X-ray Scattering

This section is intended to give only short summary of the basics of x-ray scattering. A more thorough and detailed introduction including the derivations of the formulas presented here can be found in various textbooks. Good examples are the textbooks by Roe [113], Birkholz [114] and Als-Nielsen [115] this section is based on.
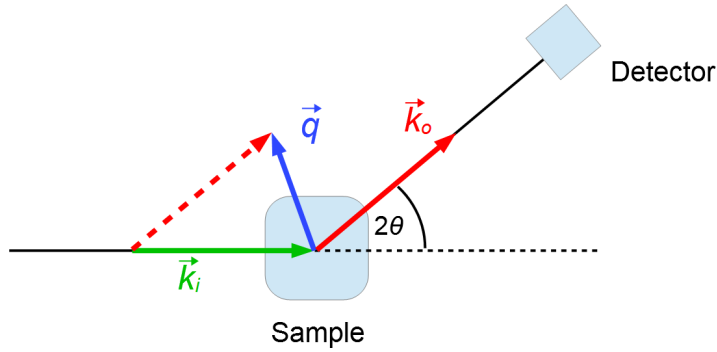
Figure 3.3.: Sketch of the general geometry of x-ray scattering experiments. The scattering can be characterized either by the scattering angle 2θ between the wave vectors of the incident wave $\vec{k_i}$ and the scattered wave $\vec{k_o}$ or by the scattering vector $\vec{q} = \vec{k_o} - \vec{k_i}$. The red dashed arrow is $\vec{k_o}$ shifted by $-\vec{k_i}$ and illustrates the geometrical construction of $\vec{q}$.

A sketch of the general geometry of x-ray scattering experiments is shown in figure 3.3. The incident wave and the scattered wave are characterized by their wave vectors $\vec{k_i}$ and $\vec{k_o}$ respectively. As only elastic scattering is considered here, $\vec{k_i}$ and $\vec{k_o}$ have the same length:

$$|\vec{k_i}| = |\vec{k_o}| = \frac{2\pi}{\lambda} \tag{3.2}$$

where λ is the wavelength of the x-rays. The angle between $\vec{k_i}$ and $\vec{k_o}$ is the so called scattering angle 2Θ. The scattering vector $\vec{q}$ is defined by:

$$\vec{q} = \vec{k_o} - \vec{k_i} \tag{3.3}$$

As $\vec{q}$ has the dimension of m, the three dimensional space $\vec{q}$ is defined in is often referred to as reciprocal space. The scattering angle 2Θ and the absolute of the scattering vector $\vec{q}$ are related by:

$$|\vec{q}| = q = \frac{4\pi}{\lambda} \sin\left(\frac{2\Theta}{2}\right) \tag{3.4}$$

In general, the incident x-ray beam is scattered due to the interactions with the electrons in the sample. Accordingly, the scattered intensity that reaches the detector at different scattering angles depends on the electron density distribution within the sample. As shown for example in the book by Roe [113], the amplitude A of the scattered intensity reaching the detector as a function of $\vec{q}$ is given by the Fourier transform of the electron density distribution $\sigma_e(\vec{r})$ of the illuminated sample volume V:

$$A(\vec{q}) = A_0 b_e \int_V \sigma_e(\vec{r}) e^{-i\vec{q}\cdot\vec{r}} d\vec{r} \tag{3.5}$$

where A_0 is the amplitude of the incident x-ray beam and b_e is the scattering length of an electron. The intensity that is measured with a detector is then proportional to the squared absolute of the amplitude: $I(\vec{q}) \propto |A(\vec{q})|^2$.

3.4.2. Scattering from Single crystals

Equation 3.5 is a general description of x-ray scattering. Further insights can be gained when considering more specific electron density distributions $\sigma_e(\vec{r})$ like the perfectly 3D-periodic electron density distributions found in ideal crystals. The periodic $\sigma_e(\vec{r})$ of an ideal crystal is fully defined by the shape and contents of its unit cell. The shape of the unit cell is typically given either by three unit cell vectors, $\vec{a}$, $\vec{b}$ and $\vec{c}$, or by the unit cell parameters a, b, c, α, β and γ, where a, b, c are the lengths of the unit cell vectors, α is the angle between $\vec{b}$ and $\vec{c}$, β is the angle between $\vec{a}$ and $\vec{c}$, and γ is the angle between $\vec{a}$ and $\vec{b}$.

Mathematically, the periodic electron density distribution can be described as a convolution of a mathematical lattice $z(\vec{r})$ and the electron density distribution of a single unit cell $\sigma_u(\vec{r})$:

$$\sigma(\vec{r}) = \sigma_u(\vec{r}) * z(\vec{r}) \tag{3.6}$$

The mathematical lattice $z(\vec{r})$ of a crystal can be expressed by a triple sum over a series of three dimensional δ-distributions:

$$z(\vec{r}) = \sum_{u=-\infty}^{\infty} \sum_{v=-\infty}^{\infty} \sum_{w=-\infty}^{\infty} \delta\left(\vec{r} - \left(u\vec{a} + v\vec{b} + w\vec{c}\right)\right) \tag{3.7}$$

By inserting equation 3.6 into equation 3.5 and using the convolution theorem one obtains:

$$A(\vec{q}) = F(\vec{q})Z(\vec{q}) \tag{3.8}$$

where the so-called structure factor $F(\vec{q})$ is the Fourier transform of $\sigma_u(\vec{r})$ and $Z(\vec{q})$ is the Fourier transform of $z(\vec{r})$. It can be shown, that the Fourier transform of a mathematical lattice is again a mathematical lattice. The lattice described by $Z(\vec{q})$ is referred to as the reciprocal lattice.
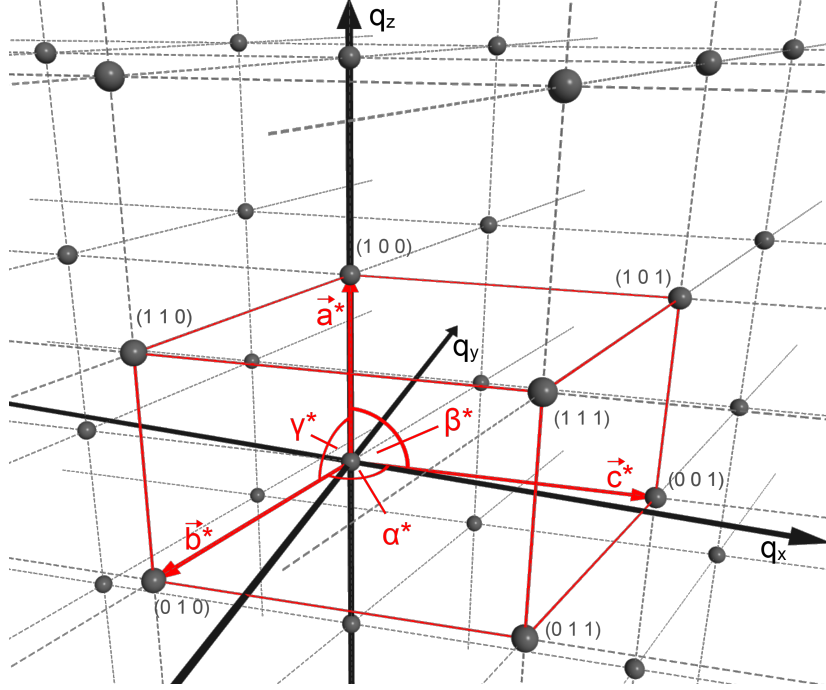
Figure 3.4.: Sketch of a reciprocal lattice and its reciprocal unit cell.

Similar to the real lattice, the reciprocal lattice can be described by three reciprocal unit cell vectors $\vec{a}^*$, $\vec{b}^*$ and $\vec{c}^*$ or by a set of six reciprocal unit cell parameters (a^*, b^*, c^*, $alpha^*$, $beta^*$, $gamma^*$). A sketch of a reciprocal lattice and its reciprocal unit cell is shown in figure 3.4. The relationship between the reciprocal unit cell vectors and the unit cell vectors of the crystal lattice are given by:

$$\vec{a}^* = \frac{2\pi\vec{b} \cdot \vec{c}}{\vec{a} \cdot (\vec{b} \times \vec{c})} \tag{3.9}$$

$$\vec{b}^* = \frac{2\pi\vec{c} \cdot \vec{a}}{\vec{a} \cdot (\vec{b} \times \vec{c})} \tag{3.10}$$

$$\vec{c}^* = \frac{2\pi\vec{a} \cdot \vec{b}}{\vec{a} \cdot (\vec{b} \times \vec{c})} \tag{3.11}$$

$$\tag{3.12}$$

The position of the reciprocal lattice points in reciprocal space ($\vec{q}$-space) is given by the reciprocal lattice vector $\vec{G}_{hkl}$:

$$\vec{G}_{hkl} = h\vec{a}^* + k\vec{b}^* + l\vec{c}^* \tag{3.13}$$

where the so-called Miller indices h,k, and l are integer numbers.

As seen from equation 3.8, $A(\vec{q}) \neq 0$ only when $F(\vec{q}) \neq 0$ and $Z(\vec{q}) \neq 0$. Consequently, since $Z(\vec{q})$ is only unequal to zero at the positions described by $\vec{G}$, scattered intensity can only be observed at scattering angles for which the scattering vector $\vec{q}$ is equal to a reciprocal lattice vector $\vec{G}_{hkl}$:

$$\vec{q} = \vec{G}_{hkl} \tag{3.14}$$

The absolute of the scattered intensity at positions where this condition is fulfilled, then depends on the structure factor $F(\vec{q})$ and thus the contents of the unit cell of the crystal. The intensity peak observed when the scattering vector $\vec{q}$ is equal to a specific $\vec{G}_{hkl}$ is often also referred to as (hkl)-reflection.
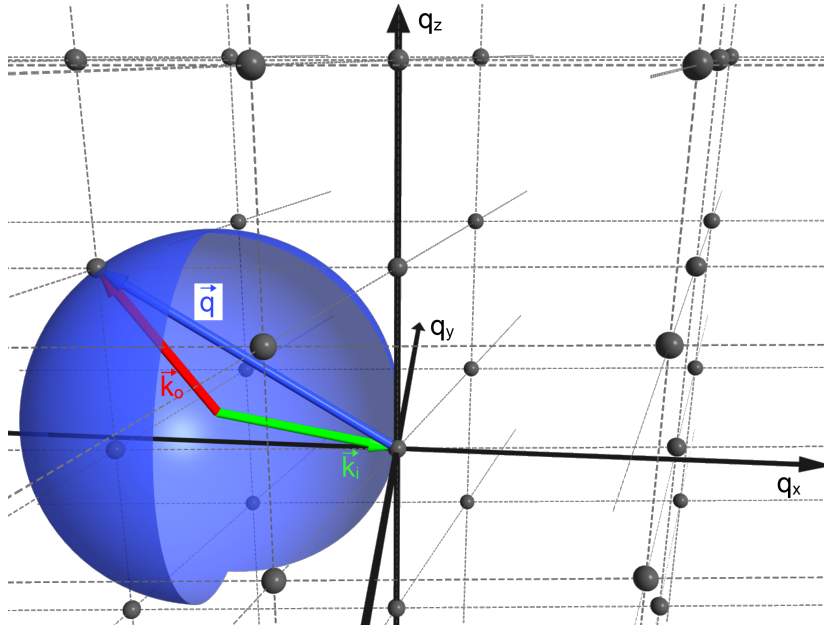
Figure 3.5.: Sketch of the Ewald sphere in reciprocal space. A section of the Ewald sphere is omitted in the sketch for better visibility.

In a typical x-ray scattering experiment one measures the scattered intensity at various different scattering angle 2Θ and thus probes the reciprocal space at various $\vec{q}$-positions. An illustrative approach to visualize which (hkl)-reflections are visible with a specific scattering geometry is the Ewald sphere construction shown in figure 3.5. When the wave vector $\vec{k}_i$ of the incident x-ray beam is positioned such that its tip points at the origin of the reciprocal space, the definition of the scattering vector $(\vec{q} = \vec{k}_o - \vec{k}_i)$ implies, that all measurable scattering vectors $\vec{q}$ lie on the surface of a sphere with radius $2\pi/\lambda$ around the base of $\vec{k}_i$. Wherever a point of the reciprocal lattice lies on the surface of this so-called Ewald sphere the corresponding (hkl)-reflection can be observed. Note, that the surface of the Ewald sphere always intersects the origin of the reciprocal space. When the sample is rotated or equivalently, when the direction from which the x-ray beam illuminates the sample is rotated, the position of the Ewald

sphere is rotated around the origin of the reciprocal space. Consequently, every reciprocal lattice point within a distance of $2|\vec{k}_i| = 4\pi/\lambda$ from the origin of the reciprocal space can be measured by correct choice of sample rotation and detector position.

3.4.3. Scattering from Polycrystalline Samples

Up to now, only scattering from single crystals was considered. For the discussion of scattering from polycrystalline samples it is helpful to define three different reference frames [114]. So far, scattering was discussed in a reference frame defined relative to a single crystal. When dealing with multiple crystals in the same sample it is useful to additionally define a reference frame relative to the investigated macroscopic sample. The third reference frame is the laboratory reference frame which is defined relative to the measuring instrument and will differ from the sample reference frame if the sample is rotated. In the reference frame of the crystal a specific reciprocal lattice vector can also be expressed by its vector components q_x, q_y and q_z:

$$\vec{G}_{hkl} = \begin{pmatrix} q_x \\ q_y \\ q_z \end{pmatrix} \tag{3.15}$$

This can be helpful when trying to determine $\vec{G}_{hkl}$ from the scattering patterns of polycrystalline samples.
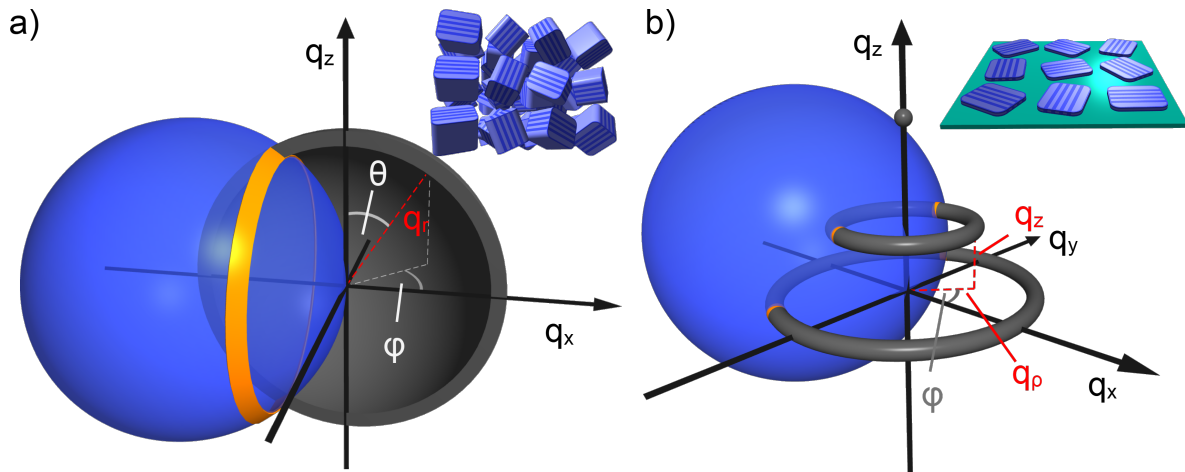
Figure 3.6.: Sketch of the distribution exemplary reflections in the reciprocal space of polycrystalline samples in the sample reference frame. a) Sample with an isotropic distribution of crystal orientations. For clarity the distribution of only one G_{hkl} is shown (grey sphere). b) Sample with an uniaxially oriented distribution of crystal orientations often found in thin films or drawn fibers. The distribution of three different G_{hkl} are shown (grey rings). The intersects of the distributions with the Ewald sphere (blue) are highlighted in orange.

If the investigated sample is not a single crystal but instead contains many different crystals their individual reciprocal lattices are superimposed in the sample reference frame. As illustrated in figure 3.6, in case of a polycrystalline sample with an isotropic distribution of crystal orientations this results in a spherical distribution of the reflections in reciprocal space of the sample. Consequently, from an observed (hkl)-reflection only the absolute of the corresponding reciprocal lattice vector can be determined while the information of the individual components of the reciprocal lattice vector:

$$|\vec{G}_{hkl}| = q_{r,hkl} = \sqrt{q_x^2 + q_y^2 + q_z^2} \tag{3.16}$$

Nonetheless, if a large number of reflections is observable, in many cases the unit cell of the investigated sample can still be determined with the help of various algorithms [116, 117].

If the distribution of crystal orientations in the sample is uniaxially oriented, as is often the case in thin films or drawn fiber samples, the superimposed reciprocal lattice points are distributed on rings around the alignment axis. A sketch of the reciprocal space of a sample where the crystals are uniaxially aligned with respect to the q_z-axis is shown in figure 3.6. As seen from the sketch, the resulting distribution of the reflections in the reciprocal space of the sample has a cylindrical symmetry. Therefore, scattering data from uniaxially aligned samples is often presented in 2D plots of intensity as a function of q_z and $q_p = \sqrt{q_x^2 + q_y^2}$. While for each reflection observed in an uniaxially aligned sample the q_z and q_p values of the corresponding reciprocal lattice vectors can be obtained, the angle ϕ cannot be determined directly from the measurements.

3.4.4. Grazing Incidence Wide Angle X-ray Scattering from Thin Films

Grazing incidence wide angle x-ray scattering (GIWAXS) is a form of WAXS used to investigate thin film samples. As the scattering intensity is directly proportional to the scattering volume, i.e. the sample volume irradiated by the x-ray beam, measuring thin films in transmission or with large angles of incidence usually results in very low scattering intensity. In GIWAXS measurements the scattering volume is increased significantly by adjusting the measurement geometry such that the x-ray beam irradiates the thin film sample under a very shallow angle of incidence α_i.

In most experiments the refraction of x-rays can be neglected as the real part of the complex refractive index n for most materials is only slightly smaller than 1 for x-rays. However for GIWAXS measurements refraction effects have to be considered due to the very shallow angles of incidence. In general, the complex refractive index is can be denoted as:

$$n = 1 - \delta + i\beta \tag{3.17}$$

where δ is the dispersion term and β is the absorption term. When considering a homogeneous medium and x-ray energies far away from absorption edges of the medium,

δ and β can be approximated as [118]:

$$\delta = \frac{\lambda^2}{2\pi} r_e \sigma_e \qquad \beta = \frac{\lambda}{4\pi} \mu \qquad (3.18)$$

where $r_e \approx 2.814 \times 10^{-5}$ Å is the classical electron radius, σ_e is the electron density and μ is the linear absorption coefficient. For most materials δ is on the order of 10^{-6}. As the resulting real part of the refractive index is smaller than 1, total external reflection can occur at the interface between vacuum and a medium if angles of incidence α_i is smaller than the critical angle α_c of the medium. The critical can be approximated by:

$$\alpha_c \approx \sqrt{2\delta(\lambda)} = \lambda \sqrt{\frac{r_e \sigma_e}{\pi}} \qquad (3.19)$$

Since α_c is proportional to $\sqrt{\sigma_e}$, the critical angle is typically larger the denser the material is. Consequently, in the case of thin polymer films supported on denser substrates like silicon, the critical angle of the substrate $\alpha_{c,Sub}$ is larger than the critical angle of the polymer $\alpha_{c,Pol}$. In GIWAXS measurements the angle of incidence is usually chosen to be in between the critical angle of the substrate $\alpha_{c,Sub} \approx 0.22$ degree and the critical angle of the polymer $\alpha_{c,Pol} \approx 0.17$ degree. This allows to maximize the scattering form the sample, while simultaneously minimizing the scattering of the underlying substrate.

Conversion of the Detector Image
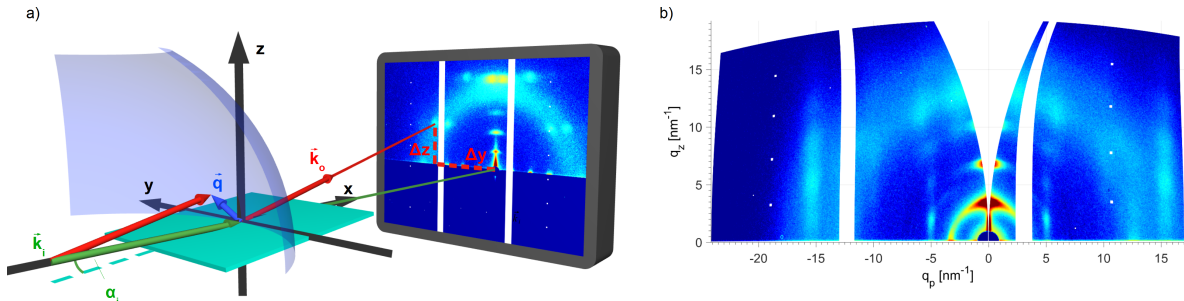
Figure 3.7.: a) Sketch of GIWAXS measurement in reflection geometry. The instrument coordinate system is indicated by the x-, y- and z-axis. b) Final reciprocal space map of the sample obtained by converting the detector image to reciprocal space taking refraction effects into account.

Figure 3.7a) illustrates the measurement geometry used for GIWAXS measurements of thin film samples. In the reference frame of the instrument the incident x-ray beam, also referred to as the primary beam, coincides with the x-axis and is perpendicular to the 2D detector. Accordingly, in this reference frame, the sample is rotated around the y-axis by the angle of incidence α_i. The 2D detector allows to simultaneously measure the intensity scattered in a certain range of scattering angles. As indicated by the blue sphere section in figure 3.7a), this corresponds to probing the reciprocal space along a

certain section of the Ewald sphere. Since the Ewald sphere curves away from the q_z-axis in reciprocal space, it is clear that the scattering pattern recorded by the detector is a distorted image of the reciprocal space. Therefore, the detector image has to be converted before further analysis. Usually the image is converted into the reciprocal space of the sample where the q_z-axis is perpendicular to sample surface and the q_x- and q_y-axis are parallel to the sample surface. The scattering observed on the 2D detector can be converted into the reciprocal space of the sample using the following formula, which also takes into account refraction effects of both incident and scattered x-rays [31]:

$$\begin{pmatrix} q_x \\ q_y \\ q_z \end{pmatrix} = \frac{2\pi}{\lambda} \begin{pmatrix} \cos\delta\cos(\gamma-\alpha_i) - \cos\alpha_i \\ \sin\delta\cos(\gamma-\alpha_i) \\ (\sin^2\alpha_i - \sin^2\alpha_c)^{1/2} + (\sin^2(\gamma-\alpha_i) - \sin^2\alpha_c)^{1/2} \end{pmatrix} \quad (3.20)$$

Here α_i is the angle of incidence, α_c is the critical angle of the sample, δ is the in-plane scattering angle and γ is the out-of-plane scattering angle. While equation 3.20 allows to describe the conversion in a relative compact form, the actual algorithm the employed analysis software uses to convert the detector image is somewhat different and will be described in the following. In general the software does all required calculations for the conversion using the wave vectors instead of scattering angles. As the difference between refraction indices of the sample and vacuum are marginally small, the length of the wave vector can be considered to be the same in both media. The software performs all required calculation using unit vectors defined by the directions of the wave vectors of the incident wave and scattered wave and only applies a factor of $2\pi/\lambda$ when the final scattering vector in the coordinate system of the sample is calculated.

As seen from the sketch in 3.7a), the unit vector $\vec{K}_i$ in the direction of the incident wave vector $\vec{k}_i$ is parallel to the x-axis in the reference frame of the instrument. The direction of the wave vector $\vec{k}_o$ of the intensity scattered into a specific pixel on the detector is defined by the position of the pixel $\vec{r}_{pix}$ in the instrument coordinate system. Since the origin of the instrument coordinate system is in the center of the sample and the primary beam is parallel to the x-axis, $\vec{r}_{pix}$ is given by:

$$\vec{r}_{pix} = (d_{sd}, \Delta y, \Delta z) \quad (3.21)$$

where d_{sd} is the sample to detector distance, and Δy and Δz are offsets of the pixel in x and y direction relative to the position of the primary beam on the detector. The unit vector $\vec{K}_o$ in the direction of $\vec{k}_o$ is then given by:

$$\vec{K}_o = \frac{\vec{r}_{pix}}{|\vec{r}_{pix}|} \quad (3.22)$$

The unit vectors $\vec{K}_i$ and $\vec{K}_o$ can then be converted into the coordinate system of the sample by rotating them both by α_i around the y-axis:

$$\vec{K}_i' = R_y \cdot \vec{K}_i \quad (3.23)$$

$$\vec{K}_o' = R_y \cdot \vec{K}_o \quad (3.24)$$

where R_y is a rotation matrix. The next step is to calculate the direction of the refracted wave vectors in the sample. This can be done using the vectorial form of Snell's law [119]:

$$\vec{K}_i'' = m\vec{K}_i' - \vec{n} \cdot \left(m\left(\vec{n} \cdot \vec{K}_i'\right) - \sqrt{1 - m^2\left(1 - \left(\vec{n} \cdot \vec{K}_i'\right)^2\right)} \right) \qquad (3.25)$$

where $\vec{K}_i''$ is the unit vector in direction of refracted incident beam in sample coordinate system, $\vec{n}$ is the unit normal vector of the sample surface pointing into the sample and m is the ratio of refractive indices. The unit vector $\vec{K}_o''$ in direction of the scattered intensity in the sample before it is refracted at the interface to vacuum can be calculated analogously. The ratio of refractive indices m can be expressed in terms of the critical angle α_c of the sample:

$$m = \frac{n_v}{n_s} = \left(\frac{1}{cos(\alpha_c)} \right) \qquad (3.26)$$

where $n_v = 1$ is refractive index of vacuum and n_s is refractive index of the sample. In the case of elastic scattering, the scattering vector $\vec{q}$ is then given by:

$$\vec{q} = \vec{k}_o'' - \vec{k}_i'' = \frac{2\pi}{\lambda}\left(\vec{K}_o'' - \vec{K}_i''\right) \qquad (3.27)$$

where $\vec{k}_i''$ and $\vec{k}_o''$ are the wave vectors of the incident and scattered wave in the sample and given in the coordinate system of the sample. An example of a detector image converted into the reciprocal space of the sample is shown in figure 3.7b).

Surface-Sensitive GIWAXS Measurements

As illustrated in figure 3.8a), whenan x-ray beam impinges on a sample at an angle of incidence α_i that is smaller than the critical angle α_c of the sample, only an evanescent wave penetrates the surface. The intensity of this wave decreases exponentially with the penetration depth. The penetration depth Λ at which the intensity of the wave drops to e^{-1} of its original intensity can be calculated with the following formula [118]:

$$\Lambda = \frac{\lambda}{\sqrt{2}\pi}\left(\sqrt{\left(\alpha_i^2 - \alpha_c^2\right)^2 + 4\beta^2} - \left(\alpha_i^2 - \alpha_c^2\right) \right)^{-\frac{1}{2}} \qquad (3.28)$$

where β absorption term of the complex refractive index. A plot of Λ as a function of the angle of incidence, calculated for $\lambda = 1.54\,\text{Å}^{-1}$, $\alpha_c = 0.165°$ and $\beta = 1 \cdot 10^{-7}$, is shown in 3.8b). As seen in the plot, the penetration depth quickly decreases to only a approximately $10\,\text{nm}$ within a few hundredths of a degree below the critical angle. Precise control of the angle of incidence therefore allows to vary the penetration depth of the primary beam into the sample. This allows to selectively measure scattering patterns of only the upper few nanometers of the sample.

a)

b)
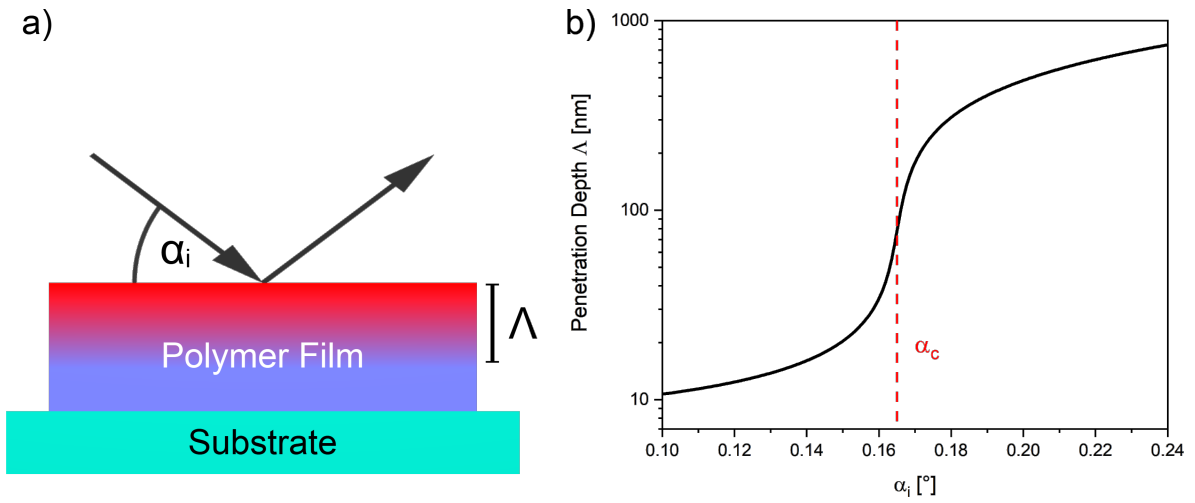
Figure 3.8.: a) For incident angles α_i smaller than the critical angle α_c of the polymer, only an evanescent wave traveling parallel to the interface penetrates the film surface. The intensity of the evanescent wave decays exponentially and is reduced by a factor of e^{-1} at the depth Λ. b) Penetration depth Λ as a function of the angle of incidence α_i.

Peak Smearing Effects

In general the peaks observed in GIWAXS scattering patterns are typically significantly broader than peaks observed in transmission WAXS measurements of the same sample. The main reason for this is the elongation of the sample in beam direction. As seen
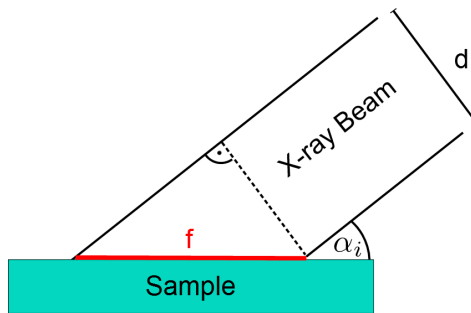
Figure 3.9.: Sketch of the dependence of the footprint f of the x-ray beam on the angle of incidence α_i and the beam width d;

from the sketch in figure 3.9, the foot print f of the beam on the sample at a certain angle of incidence α_i is given by:

$$f = \frac{d}{\sin(\alpha_i)} \tag{3.29}$$

where d is the beam width. For typical values of $d = 0.9\,\text{mm}$ and $\alpha_i = 0.18°$, the footprint is $> 28\,\text{cm}$ which is significantly larger than the length of typical samples
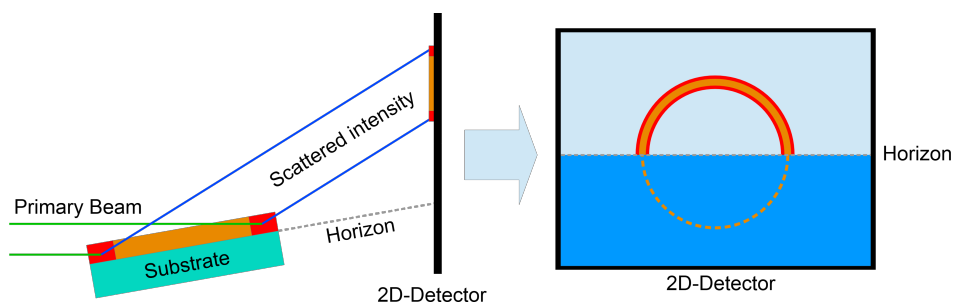
Figure 3.10.: Sketch illustrating the effect of the sample elongation in primary beam direction on the measured intensity distribution.

($\approx 10\,\text{mm}$). Therefore the whole sample is illuminated by the primary beam. As illustrated in figure 3.10 the sample to detector distance varies along the length of the sample which results in a radial broadening of observed scattering peaks. Additionally, as the foot print of the beam is larger than the sample the position of the scattering peaks is sensitive to errors in the positioning of the sample in beam direction. The GIWAXS samples are positioned manually and an error in positioning in the primary beam direction of $\approx \pm 0.5\,\text{mm}$ can be expected. This leads to a general offset of peaks in the radial direction, the extent of which increases with the scattering angle 2Θ. However, this effect is rather small compared to the broadening due to the elongation of the samples and the true position of the reflection will always lie within the broadened peak.
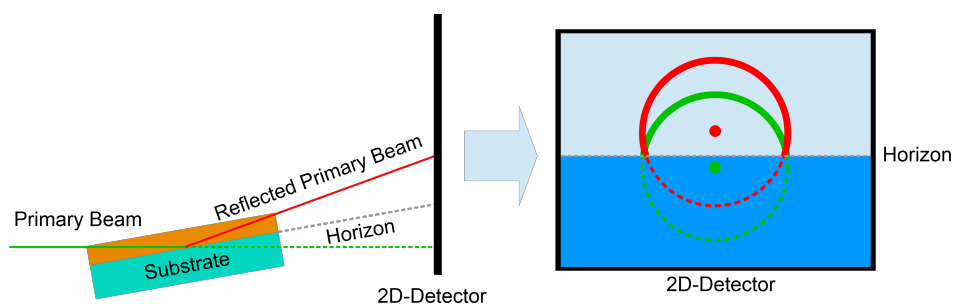
Figure 3.11.: Sketch illustrating the effect of scattering from the primary beam and scattering from the reflected primary beam on the measured intensity.

Another effect that leads to peak broadening is shown in figure 3.11. As the GIWAXS patterns are typically measured at an angle of incidence α_i that is smaller than the critical angle of the substrate, a large fraction of the intensity of the primary beam will be reflected by the substrate. Since scattering will occur both from the primary beam and the reflected primary beam two scattering patterns are superimposed on the detector. The offset of both scattering patterns in the out of plane scattering angle is equal to $2\alpha_i$. The extent of the shift is exaggerated in figure 3.11. For typical angles of incidence only a broadening of peaks in q_z-direction can be observed instead of a splitting of peaks. However, the broadening will result in a noticeable difference between

the q-position of identical reflections located on the horizon and on the q_z-axis(e.g. in the case of isotropic scattering).

3.4.5. X-Ray Scattering Instrument
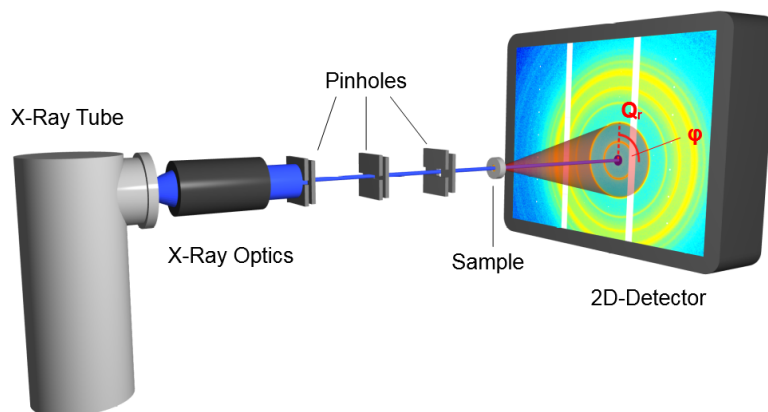
Figure 3.12.: Schematic view of the main components of the microfocus X-ray setup. Here, a WAXS measurement on a powder sample performed in transmission geometry is illustrated.

A schematic view of the main components of the microfocus X-ray setup used to obtain the WAXS and GIWAXS patterns shown throughout this thesis is given in figure 3.12. The instrument used was a *Retro-F* setup from *SAXSLAB* (Copenhagen, Denmark) equipped with a microfocus X-ray source from *AXO* (Dresden, Germany). An *AXO* multilayer x-ray optics (*ASTIX*) was used as a monochromator for Cu Kα radiation ($\lambda = 0.154\,18\,\mathrm{nm}$).

The width of the cross section and the divergence of the primary beam are defined through a series of three pinholes. Each pin hole consists of a vertical and a horizontal slit. The function of the pinhole closest to the sample is to minimize the background radiation due to scattering from the first two pinholes [113].

The two dimensional scattering patterns were recorded using a *PILATUS R 300 K* detector from *DECTRIS* (Daettwil, Switzerland). A *Linkam* hot stage was used to perform temperature dependent measurements. All WAXS and GIWAXS measurements were performed under vacuum.

3.5. Preparation of Thin Film Samples

The thin films of semiconducting polymers on silicon and graphene substrates investigated within the context of this thesis were spin-coated from solution.

The silicon substrates of approximately $10 \times 10\,\mathrm{mm}^2$ were cut from larger silicon wafers with a naturally oxidized oxide layer of $2\,\mathrm{nm}$ to $3\,\mathrm{nm}$. The silicon substrates were cleaned in sulfuric acid for 30 min and rinsed with distilled water afterwards. The substrates were then dried in a vacuum oven at $160\,^\circ\mathrm{C}$ for $1\,\mathrm{h}$. Directly before thin films

were spin-coated onto the silicon substrates the substrates were cleaned again with a CO_2-snowjet.

The graphene substrates used were single-layer graphene on ultraflat SiO_2/Si with a size of $10 \times 10\,mm^2$. These substrates were purchased from *Graphenea* (San Sebastian, Spain). The graphene substrates were stored in a vacuum oven prior to use and used as purchased without any additional cleaning procedure.

The thin films of the investigated polymers were spin-coated onto the substrates from chloroform solution using a spinning speed of 2000 rounds per minute and a spinning duration of 60 s. The film thickness was controlled by varying the concentration of the chloroform solutions. The film thicknesses of the resulting films were measured using x-ray reflectometry (XRR). For films that were to thick to be measured with XRR, the thickness was determined by scratching the films with a surgical knife and measuring the depth of the resulting scratch with AFM instead.

All films presented in this thesis were crystallized by cooling from the melt if not stated otherwise. The thin film samples presented in chapters 4 and 6 were crystallized directly in the microfocus x-ray setup under vacuum using a *Linkam* hot stage. As the special sample holder required to use the *Linkam* hot stage for thin film samples in the microfocus setup only became available during the course of this thesis, the films of polythiophenes with ethylene glycol side chains presented in chapter 5 were thermally treated in a vacuum oven instead. The vacuum oven has the disadvantage that the temperature sensor is of the oven is rather far away from the samples. Consequently, a significant temperature dependent temperature offset between the temperature of the sample and the temperature indicated by the oven was observed (based on incomplete melting). While this offset can somewhat be compensated by simply increasing the set point temperature of the oven, the overall reliability and reproducibility is not optimal. Furthermore, the used vacuum oven also neither offered the option of controlled heating or cooling rates, nor did it allow for active cooling. The cooling rate after turning off the oven is estimated to be approximately 1 K/min

4. Controlling Crystal Orientation via Chemical Modification of the Side Chains

The significant anisotropy of the charge transport properties of semiconducting polymers result in a strong dependence of the efficiency of the final electronic devices on the crystal orientations in the polymer film [120, 58, 121, 27]. Applications which require horizontal charge transport benefit from a dominant edge-on orientation. In contrast, in applications which require vertical charge transport like OPV devices, the face-on orientation is more favorable [122, 123]. In thin films of P3HT and many other semiconducting polymers with alkyl side chains, crystallized from the melt on substrates that do not induce a specific orientation on their own, the edge-on orientation is dominant [31]. Therefore, finding a method to reliably induce face-on orientation in thin films of semiconducting polymers is crucial for efficient OPV devices. In recent years many different approaches to induce face-on orientation in P3HT films have been investigated. Some of these approaches are mechanical stretching and rubbing [124, 120, 125, 126], drop or spin-coating from low-boiling-point solvents [127] and the use of specific substrates [128, 129, 32, 130, 57, 131]. Despite many attempts, so far none of these approaches have been successful in producing P3HT films of thickness relevant for organic electronic devices ($d \geq 100\,\text{nm}$) with a complete face-on orientation. Furthermore, mechanical stretching and rubbing, as well as drop or spin-coating from low-boiling-point solvents result in nonequilibrium crystal structures. As these crystals are usually thermally less stable they are likely to reorganize upon thermal treatment and the crystal orientation will be altered irreversibly.

As has been shown for P3HT both by simulations and by experiments, the prefference for edge-on orientation is induced by the upper interface of the film, i.e. the interface to air or vacuum apparently induces the formation of edge-on oriented crystals [132, 31]. This is quite similar to the phenomenon of surface freezing where the interface in vacuum also induces oriented crystallization [68]. Thus it can be hypothesized, that the edge-on crystals in thin films of P3HT are induced by the interface to vacuum through a similar mechanism. As discussed in section 2.2, the appearance of surface freezing depends on the involved interfacial energies. Consequently, it should be possible to suppress the crystallization induced by the vacuum interface by increasing the surface energy of the solid-vapor interface. For semiconducting polymers it was demonstrated that the surface energies can be tuned through chemical modifications of the side chains [133, 134, 135]. However, the different crystal orientations differ in the relative fraction

Figure 4.1.: Chemical structures of the investigated side chain modified Polythiophenes with differently polar end groups of the side chains. The differences in the chemical structure of P3BrHt, P3CF$_3$HT and PrCNHT with regard to P3HT are highlighted in color.

of side chains and in what segments of the side chains are exposed to the interface to vacuum. Therefore, the crystal orientation induced at the interface to vacuum has to be considered to identify where along the side chain the introduced chemical modifications are expected to be most effective in suppressing the formation of these crystals.

For edge-on oriented P3HT crystals the side chains are oriented normal to the substrate and therefore, the interface to vacuum is comprised of hexyl side chains and will likely have a high density of methyl end groups. Consequently, the surface free energy of the interface between vacuum and the edge-on oriented crystal can likely be increased most effectively by increasing the polarity of the end groups of the side chains. If the increase in surface free energy is sufficiently large this should result in the complete suppression of the induction of edge-on oriented crystals at the interface to vacuum.

Here a series of four polythiophens with increasingly more polar end groups of the alkyl side chains is investigated to determine how the polarity of the end groups influences the distribution of crystal orientations in thin films. The four investigated polythiophenes are (cf. fig. 4.1): P3HT, P3BrHT, P3CF$_3$HT and P3CNHT. [1] An

---

[1]P3HT was purchased from BASF SE and purified by a Soxhlet extraction using methanol, hexane, and chloroform. The chloroform fraction was concentrated and precipitated in methanol to obtain the polymer powder used in the presented experiments. PDPP[T]$_2$-T was purchased from Ossila, Sheffield, England. The remaining polymers were synthesized by the group of professor Mukundan Thelakkat from the university of Bayreuth (Philip Schmode: P3BrHT; Florian Meichsner: P3CF$_3$HT, P3CNHT; Andreas Erhardt: PDPP[T]$_2${2-HD}$_2$-T{CNH}). DSC, WAXS, GIWAXS and AFM measurements on thin films of P3HT and P3BrHT were performed by Oleksandr Dolynchuk from the group of professor Thurn-Albrecht from the Martin Luther University Halle-Wittenberg. DSC, GIWAXS, AFM and POM measurements of P3CF$_3$HT were performed by Alexander Much in the context of a master thesis supervised by Robert Kahl and Oleksandr Dolynchuk [136]. Initial investigations of P3CNHT films on silicon substrates (not included here)

overview of the molecular weight, the dispersity Đ and the dipole moment of the end group of the side chains μ_{E-SC} of the four investigated polythiophenes is given in table 4.1 together with a summary of selected thermal and structural parameters discussed in the following sections.

The results presented here reveal a decreasing tendency to form edge-on oriented crystals at the interface to vacuum with increasing dipole moment of the end group of the side chains μ_{E-SC}, culminating in the complete suppression of edge-on oriented crystals in P3CNHT. The detailed investigation of the crystal structures of the different polythiophenes reveals, that the ordering in the crystalline phase is mostly unaffected by the introduced chemical modifications, except for the P3CNHT sample in which a certain increase of the unit cell in the backbone direction is observed. Additionally, the effect of the competing crystallization of edge-on and face-on oriented crystals in P3CF$_3$HT is investigated, revealing a strong dependency of the final distribution of crystal orientations and morphology in thin films on the crystallization conditions. The results presented in this section have partially been published in references [34] and [138].

Table 4.1.: Sample Properties of Investigated Polythiophenes with Polar End Groups of the Side Chains

Polymer	$M_n{}^a$ [kDa]	Đ^a	$T_m{}^b$ [°C]	$\Delta H_m{}^b$ [J g^{-1}]	$\chi_c{}^c$ [%]	$d_{100}{}^d$ [Å]	$d_{020}{}^d$ [Å]	μ_{E-SC} [D]
P3HT	15.6	1.6	231	24.6	81	16.8	3.8	≈0
P3BrHT	10.8	1.1	136	7.1	43	17.6	3.89	1.81
P3CF$_3$HT	22	1.26	212	18	67	17.3	3.89	2.32
P3CNHT	10.3	1.56	190	10.2	52	18.2	3.75	3.92

^{a} Determined by GPC. ^{b}Determined by DSC. ^{c}Determined from WAXS measurements as described by Balko et al. [139] ^{d}Determined from WAXS measurements. ^{e}Dipole moments of small molecules equivalent to the end groups of P3AT side chains taken from NIST database [140].

---

were performed by Anna Averkova in the context of a bachelor thesis supervised by Robert Kahl and Oleksandr Dolynchuk [137]. DSC, WAXS, GIWAXS, AFM and POM measurements of P3CNHT, as well as WAXS measurements of P3CF$_3$HT were performed by the author of this thesis.

4.1. Effect on Phase Transitions and Crystal Lattice

Modifying the chemical structure of a polymer can severely influence the ordering of the polymer. For example it can result in a modified crystal structure, an in- or decrease in crystallinity, melting and crystallization temperatures or even in a complete suppression of the crystallization resulting in an amorphous material. Especially the molecular packing within the crystalline phase is known to influence the charge carrier mobility and other properties of semiconducting polymers [24, 25, 26]. Therefore, the influence of the differently polar end groups of the side chains on the crystallization behavior of polythiophenes and the crystal unit cell was investigated with DSC, WAXS and GIWAXS measurements.
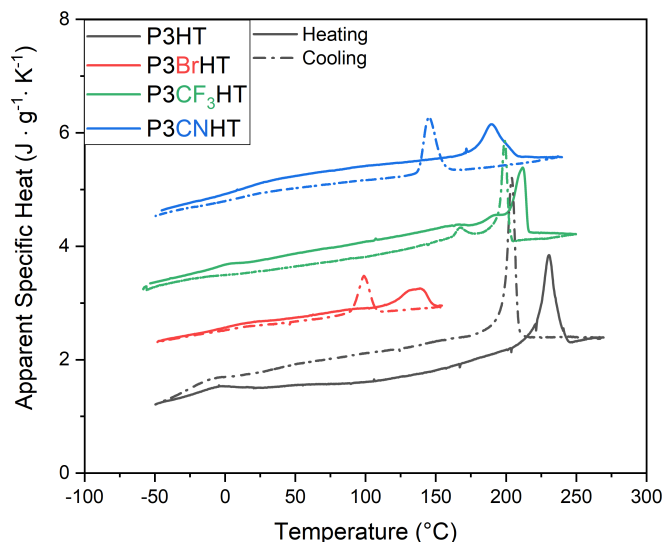

Figure 4.2.: DSC measurement of the investigated polythiophenes with different polar end groups of the side chains. Measurements were performed with a cooling/heating rate of $10\,\mathrm{K/min}$. The first cooling (dashed) and the second heating run (solid) are shown. Measurements of different polymers are shifted vertically for better visibility.

Figure 4.2 shows the first cooling and the second heating run of the DSC measurements of the different polythiophenes. The cooling/heating rate in all measurements was $10\,\mathrm{K/min}$. For all the investigated polythiophenes clear crystallization and melting peaks are visible indicating that the introduced chemical modifications do not prevent these polymers from crystallizing. Nonetheless, all modified polythiophenes show a reduction in both melting temperature T_m and melting enthalpy ΔH_m compared to P3HT($T_m = 231\,^{\circ}\mathrm{C}$, $\Delta H_m = 24.6\,\mathrm{J\,g^{-1}}$). However, these changes are not correlated with the dipole moment of the end groups of the side chains. While melting temperatures in P3CF$_3$HT and P3CNHT drop by $\approx 20\,\mathrm{K}$ and $\approx 40\,\mathrm{K}$ respectively, the

melting temperature of P3BrHT is almost $100\,\text{K}$ lower than that of P3HT. The melting enthalpies follow the same trend where P3BrHT ($\Delta H_m = 7.1\,\text{J}\,\text{g}^{-1}$) shows the smallest melting enthalpy followed by P3CNHT ($\Delta H_m = 10.2\,\text{J}\,\text{g}^{-1}$) and then P3CF$_3$HT ($\Delta H_m = 15.3\,\text{J}\,\text{g}^{-1}$). Since the observed reductions in melting temperature and enthalpy are clearly not correlated with the polarity of the end group of the side chains, the polarity in itself is likely not the primary reason for the reductions. As the chemical structures of the different investigated polythiophenes differ only slightly, the observed reductions in melting enthalpies compared to P3HT is likely an indication of reduced crystallinity. The melting temperatures and melting enthalpies of the four polythiophenes are summarized in table 4.1.
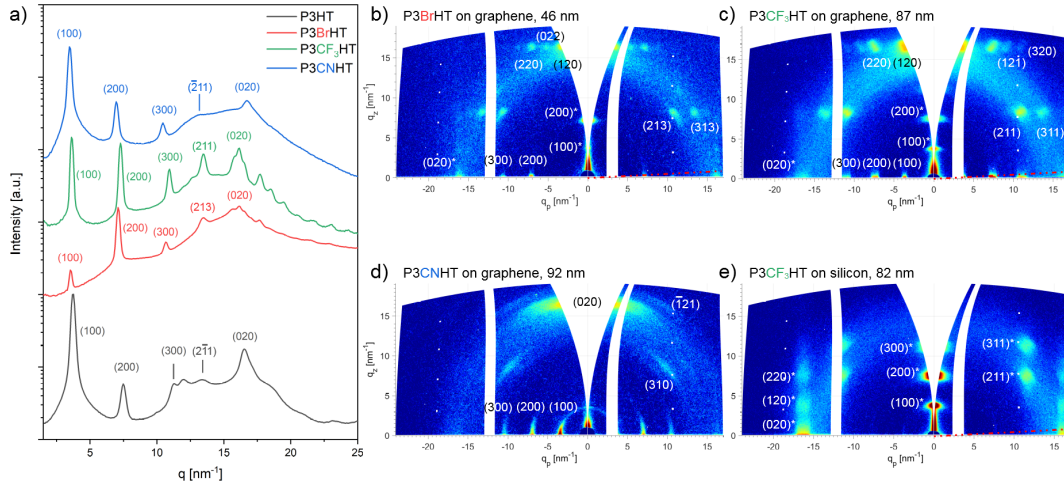

Figure 4.3.: a)WAXS patterns of powder samples and b-e) GIWAXS patterns of thin films of the investigated polythiophenes with differently polar end groups of the side chains. WAXS and GIWAXS patterns were measured after crystallizing the samples from the melt. Curves of different polymers in a) are shifted vertically for better visibility. P3BrHT sample is measured at an angle of incidence $\alpha_i = 0.20°$. All other samples are measured at $\alpha_i = 0.18°$. Reflections originating from edge-on oriented crystals are indicated with * in b-e). The red dashed lines in b), c) and e) illustrate an angle of 87° to the q_z axis.

The results of the powder WAXS measurements are shown in figure 4.3a). Despite apparent differences between the different scattering patterns, the curves share a number of common features: a series of regularly spaced (h00) reflections, an (020) reflection and additionally some peaks with mixed indices. Note that in P3BrHT the (200) reflection is the most intense of the (h00) reflections which is in contrast to the other investigated polythiophenes where the (100) reflection has the highest intensity. As discussed by Schmode et al. [141] this is likely caused by an increased electron density in the middle of two neighboring backbones in the side chain direction due to the accumulation of Bromine end groups which have a higher electron density than the other end groups. The crystallinity values χ_c of the different polythiophenes were estimated from the powder WAXS patterns by comparing the scattering intensities in between the (100) and (200) peaks (attributed to the amorphous fraction of the samples) in the

semicrystalline and in the fully amorphous (i.e. melt) state as described by Balko et al. [139] The resulting crystallinity values decrease going from P3HT ($\chi_c = 81\%$) to P3CF$_3$HT ($\chi_c = 67\%$), to P3CNHT ($\chi_c = 52\%$), to P3BrHT ($\chi_c = 43\%$). Thus, the determined crystallinity values follow the same trend as both the melting temperatures and enthalpies as measured by DSC.

The comparison of the positions of the (h00) and (020) peaks in the different WAXS curves further shows, that while the interlayer spacing in side chain direction differs significantly between the different polythiophenes, the π-π-stacking distance differs only slightly. The d_{100} and d_{020} values, as well as the crystallinity values of the different samples are summarized in table 4.1.

A more thorough analysis of the influence of the different side chains on the crystal structure requires the determination of the crystal unit cell for each of the four polymers.

For P3HT a number of different unit cells have been proposed in literature. While initial publications proposed an orthorhombic unit cell [142, 143], later publications proposed different monoclinic unit cells instead [144, 145]. Joshi and coworkers proposed different monoclinic unit cells with an angle $\beta \neq 90°$ [145, 146, 147], whereas Brinkmann and coworkers have proposed a series of monoclinic unit cells with an angle $\gamma \neq 90°$ ranging from $\gamma = 85°$ to $\gamma = 86.5°$ [144, 148, 149]. Several publications have reported good agreement of their measurements of P3HT with unit cells similar to those proposed by Brinkmann and coworkers where the angle γ deviates only slightly from 90° [42, 150, 31]. Similarly, Schmode et al. [141], who investigated the same P3HT sample as used in this thesis, found that the WAXS pattern of this P3HT sample can be well explained with a monoclinic unit cell with $\gamma = 92.7°$.

In the following the crystal structures of P3BrHT, P3CF$_3$HT and P3CNHT will be derived based on similarities in their scattering patterns. While Schmode et al. already proposed a triclinic unit cell for P3BrHT [141], the scattering data of P3BrHT are reevaluated here in the hope of benefiting from the direct comparison to similar polythiophenes and thus being able to find a unit cell with higher symmetry.

As the determination of the unit cell depends on the indexing of observed scattering peaks and the indexing of peaks in WAXS measurements can be quite difficult and ambiguous, the peaks were indexed based on the GIWAXS images shown in figure 4.3b-e) instead. Note, that in the GIWAXS patterns of P3BrHT, P3CF$_3$HT and P3CNHT on graphene shown in figure 4.3 b-d) a dominant face-on orientation is observed. In contrast, the GIWAXS pattern of the P3CF$_3$HT film on silicon shown in figure 4.3 e) shows a strong edge-on orientation. Additional measurements at an angle of incidence of $\alpha_i = 10°$ and an enlarged powder WAXS pattern of P3CNHT are given in appendix A. All peak positions extracted from WAXS and GIWAXS mesurements of P3BrHT, P3CF$_3$HT and P3CNHT are tabulated in appendix D together with the expected peak positions calculated from the unit cells proposed and discussed in the following.

As P3CF$_3$HT shows quite a few intense reflections and scattering patterns of both face-on and edge-on oriented crystals are available, the unit cell of P3CF$_3$HT is the

simplest to analyze. As seen in the two GIWAXS measurements of P3CF$_3$HT, the (h00) reflections of the face-on crystals as well as the (020) reflection of the edge-on crystals seem to be located directly on the q_p-axis. For a monoclinic unit cell with $\gamma \approx 93°$ (or $\gamma \approx 87°$) the angle γ^* between the (100) and the (020) reflection observed in GIWAXS measurements should be $\approx 87°$ (or $\approx 93°$) both for face-on and edge-on oriented crystals. Accordingly, the face-on (h00) and the edge-on (020) reflections should both be located at an angle of $\approx 87°$ to the q_z-axis. As illustrated by the red dashed lines in figure 4.3 c,e) the face-on (300) and the edge-on (020) reflections are clearly closer to the q_p-axis than expected for such a unit cell. Therefore, within the precision of the GIWAXS measurements γ^* can be assumed to be $\approx 90°$. In combination with the observation that all observed reflections are found on layer lines parallel to the q_p-axis for both face-on and edge-on oriented samples it can be concluded that the remaining angles of the reciprocal unit cell α^* and β^* are also $\approx 90°$. The reciprocal unit cell parameters a^* and b^* can be directly determined form the q-position of the (h00) and (020) reflections in the powder WAXS measurements. Due to the orthorhombic unit cell, c^* can then be determined from the q-position of the (211) reflection:

$$c^* = \sqrt{q_{211}^2 - (2a^*)^2 - b^{*2}} \tag{4.1}$$

The resulting orthorhombic unit cell of P3CF$_3$HT ($a = 17.26$ Å, $b = 7.79$ Å, $c = 7.89$ Å, $\alpha = \beta = \gamma = 90°$) results in a good agreement between expected and observed positions of reflections.
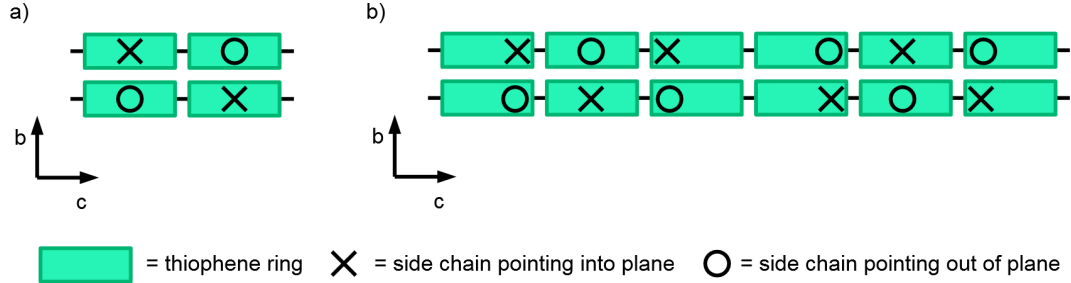

Figure 4.4.: a) Sketch of the unit cell of P3HT as seen from the side chain direction illustrating the arrangement of thiophene rings and side chains. b) Sketch of the proposed unit cell of P3BrHT as seen from the side chain direction illustrating a possible arrangement of thiophene rings and side chains that could explain the observed tripling of the unit cell in c-direction.

Under the assumption that the unit cell of P3BrHT is orthorhombic as well, the unit cell parameters of P3BrHT can be determined analogously as in the case of P3CF$_3$HT. The resulting unit cell gives accurate predictions for the positions of all reflections except for the peak labeled (022) in figure 4.3b) for which none of the calculated possible reflections are reasonably close in position. Schmode et al. faced the same problem for the same reflection (labeled peak 9 in their publication) for the first unit cell they proposed (labeled as scenario 1 in their publication) [141]. They were able to resolve this issue by increasing the size of the unit cell in c-direction by a factor of roughly 1.5.

Based on the overall similarity of their proposed unit cell to that of P3HT this would correspond to including three thiophene rings in the unit cell in *c*-direction instead of two. While this does allow to index all observed peaks, it seems unlikely for two reasons: On one hand, the reason for the unit cell of P3HT containing two thiophene rings in the *c*-direction instead of one is that the side chains of neighboring thiophene rings alternate in pointing to the one or the other side of the *b-c*-plane (cf. fig. 4.4a)). Therefore it is hard to imagine an arrangement with a period of three thiophene rings. On the other hand, the peaks labeled (213) and (313) in the GIWAXS image of P3BrHT and the peaks labeled (211) and (311) in the GIWAXS image of P3CF$_3$HT seem to be of similar nature and thus likely have the same origin and should be indexed in an equivalent way (cf. fig. 4.3b,c)). Increasing the *c*-parameter of the unit cell by a factor of 1.5 would make this impossible as the equivalent indexing would then be $(21\frac{3}{2})$ which of course is not a valid triple of Miller indices. Consequently, an increase of the *c*-parameter by a factor of 3 is proposed instead, as the resulting orthorhombic unit cell ($a = 17.65\,\text{Å}$, $b = 7.78\,\text{Å}$, $c = 23.36\,\text{Å}$, $\alpha = \beta = \gamma = 90°$) solves both of the aforementioned problems while also allowing to index all observed reflections and giving good agreement between the calculated and the observed positions of reflections. Although the exact arrangement of monomers in the unit cell is unclear, one possible arrangement of side chains that could explain the tripling of the unit cell size in *c*-direction is sketched in figure 4.4b). The replacement of a hydrogen atom of the methyl end group with a larger bromine atom in P3BrHT likely leads to an increased volume requirement per side chain. This could possibly lead to an arrangement of side chains where side chains of two next neighboring thiophene rings partially occupy the vacancy in between them resulting from the side chain of the neighboring thiophene ring pointing to the other side of the backbone (*b-c*-plane).

In comparison to P3BrHT and P3CF$_3$HT, P3CNHT shows fewer and less intense reflections with mixed indices. In the WAXS measurement these reflections are barely visible making an accurate determination of the peak positions difficult. Accordingly, only the parameters a^* and b^* were determined from the WAXS measurement. The parameter c^* was determined based on the positions of one of the indexed peaks the GIWAXS pattern. In a first attempt, the peak labeled (310) in figure 4.3d) was indexed as $(\bar{2}11)$ in analogy to the other polythiophenes instead. However, the resulting orthorhombic unit cell ($a = 18.16\,\text{Å}$, $b = 7.51\,\text{Å}$, $c = 8.60\,\text{Å}$, $\alpha = \beta = \gamma = 90°$) did not allow to index the peak labeled $(\bar{1}21)$ in figure 4.3 (cf. table D.4 in appendix D). Introducing an angle $\gamma^* \neq 90°$ allows to index peak this peak as (221), while also resulting in a slightly better agreement between observed and predicted peak positions. However, the resulting unit cell ($a = 18.2\,\text{Å}$, $b = 7.53\,\text{Å}$, $c = 9.34\,\text{Å}$, $\alpha = \beta = 90°$, $\gamma = 86°$) gives an unreasonably large *c* parameter. Consequently, the attempt to index the peak labeled (310) in figure 4.3d) analogously to the other polythiophenes was dropped and the peak was indexed as (310) instead. According to the law of cosine, the angle γ^*

Table 4.2.: Unit Cell Parameters of the Investigated Polythiophenes

Reciprocal Unit Cell						
	$a^*[\text{Å}^{-1}]$	$b^*[\text{Å}^{-1}]$	$c^*[\text{Å}^{-1}]$	$\alpha^*[°]$	$\beta^*[°]$	$\gamma^*[°]$
P3HT[a]	0.375	0.831	0.797	90	90	87.3
P3BrHT	0.356	0.808	0.269	90	90	90
P3CF$_3$HT	0.364	0.807	0.796	90	90	90
P3CNHT	0.346	0.837	0.774	90	90	92.1
Real Unit Cell						
	$a[\text{Å}]$	$b[\text{Å}]$	$c[\text{Å}]$	$\alpha[°]$	$\beta[°]$	$\gamma[°]$
P3HT[a]	16.77	7.57	7.88	90	90	92.7
P3BrHT	17.65	7.78	23.36	90	90	90
P3CF$_3$HT	17.26	7.79	7.89	90	90	90
P3CNHT	18.17	7.51	8.12	90	90	87.9

[a] Unit cell of P3HT as determined in [141].

can than be determined from the position q_{310} of the (310)-reflection:

$$\cos\gamma^* = \frac{q_{310}^2 - 9a^{*2} - b^{*2}}{6a^*b^*} \tag{4.2}$$

Indexing the last remaining visible peak in the scattering pattern shown in figure 4.3d) as ($\bar{1}21$) reflection allows to determine the length of $c*$. Under the assumption of $\alpha^* = \beta^* = 90°$ the parameter c^* is given by:

$$c^* = \sqrt{q_{\bar{1}21}^2 - q_{\bar{1}20}^2} \tag{4.3}$$

where $q_{\bar{1}21}$ and $q_{\bar{1}20}$ are the positions of the ($\bar{1}21$)- and ($\bar{1}20$)-reflection respectively. While the ($\bar{1}20$)-reflection in not visible in the scattering pattern, its hypothetical position can be calculated based on the already determined reciprocal unit cell parameters:

$$q_{\bar{1}20} = \sqrt{a^{*2} + 4 * b^{*2} - 4a^*b^*} \tag{4.4}$$

The resulting unit cell of P3CNHT ($a = 18.17\,\text{Å}$, $b = 7.51\,\text{Å}$, $c = 8.11\,\text{Å}$, $\alpha = \beta = 90°$, $\gamma = 87.9°$) shows a reasonably good agreement between calculated and observed positions of reflections.

The proposed unit cells for P3BrHT, P3CF$_3$HT and P3CNHT are summarized in table 4.2 together with the unit cell of P3HT proposed by Schmode et al. who investigated the same P3HT sample as used in this thesis [141]. Overall, all unit cells of the investigated polythiophenes are either orthorhombic or monoclinic with an angle γ that only slightly varies from 90°. The comparison of the unit cell dimensions reveals, that the different unit cells differ in their a-spacing as expected due to the different

lengths of the side chains. In contrast, the *b*-spacings of the different unit cells are quite comparable. The largest differences between the different unit cells is observed in the *c*-spacing of P3BrHT. However, as discussed above, the larger *c*-parameter of P3BrHT is likely a result of a different packing of the side chains resulting in having to extend the unit cell to include six thiophene rings in the *c*-direction instead of two, while the actual spacing of thiophene rings along the backbone is comparable to P3HT and P3CF$_3$HT ($\frac{1}{3}c_{P3BrHT} = 7.79$ Å).

Overall, all investigated polythiophenes have rather similar unit cells indicating that the modifications of the end groups of the side chains do not significantly affect the molecular packing of the polymers in the crystalline phase.

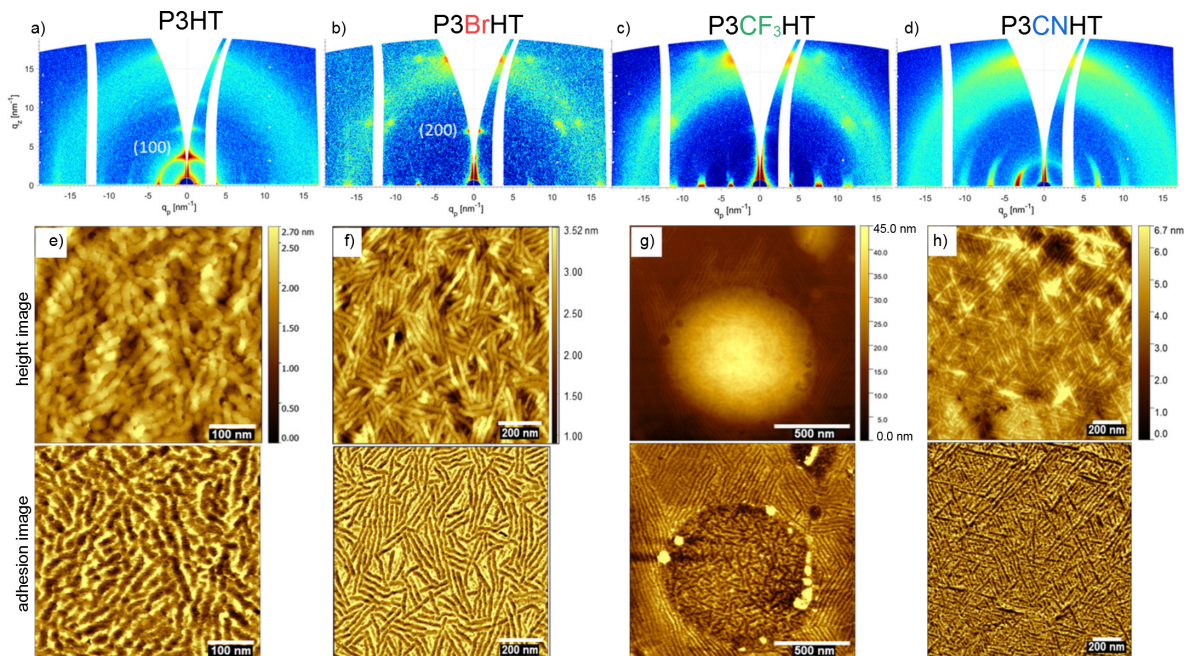## 4.2. Crystal Orientation and Morphology in Thin Films

Figure 4.5.: Crystal orientation and surface morphology in thin P3AT films on graphene substrates. GIWAXS patterns of a) a 55 nm thick P3HT film, b) a 46 nm thick P3BrHT film, c) a 46 nm thick P3CF$_3$HT film and d) a 193 nm thick P3CNHT film. Measured at angles of incidence $\alpha_i = 0.18°$(a,c,d) and $\alpha_i = 0.2°$(b) chosen to be above the critical angles of the samples (0.174° for P3BrHT, 0.163° to 0.165° for the other P3ATs). AFM height (upper row) and adhesion (lower row) images of e) a 46 nm thick P3HT film, f) a 35 nm thick P3BrHT film, g) a 25 nm thick P3CF$_3$HT film and h) a 21 nm thick P3CNHT film. The imaged area varied in the range of $0.5 \times 0.5\,\mu m^2$ and $1.5 \times 1.5\,\mu m^2$. Adapted with permission from [138]. Copyright 2024 American Chemical Society.

To determine the influence of the polarity of the end group on the crystal orientation in thin films of P3ATs on graphene substrates a series of films with different thick-

nesses were investigated for each of the P3ATs with modified side chains. Figure 4.5 a-d) shows representative GIWAXS patterns for the different samples and P3HT for comparison. The GIWAXS patterns shown for P3HT, P3BrHT and P3CF$_3$HT were obtained from films with thicknesses in the range of 45 nm to 60 nm. The shown GIWAXS pattern of P3CNHT was obtained from a film of about 200 nm. All films were crystallized by cooling from the melt. Comparing the intensity of the (h00) reflections on the meridian in the different samples, it is clear that the amount of edge-on crystals decreases monotonously with increasing polarity of the end group of the side chains. The P3HT thin film shows a mixed edge-on and face-on orientation with intense (h00) reflections on the meridian. This mixed orientation is consistent with reports from literature where P3HT shows mixed edge-on and face-on orientation even in films of only 10 nm thickness. [32, 130]. In contrast, thin P3BrHT films on graphene of up to 26 nm thickness crystallized from the melt show complete face-on orientation as previously reported by Dolynchuk et al. [34]. In films thicker than 26 nm additional edge-on oriented crystals appear (cf. fig. 4.5 b) resulting in a mixed crystal orientation similar to that found in P3HT films. Based on these observations it is evident that in P3BrHT films the formation of edge-on crystals is somewhat hindered compared to the case of P3HT films but not completely suppressed.

The GIWAXS measurement of the P3CF$_3$HT film (cf. fig. 4.5 c) shows intense (h00) reflections on the horizon and barely visible (h00) reflections on the meridian indicating that almost all crystals in the film are face-on oriented. Demonstrating that while the formation of edge-on oriented crystals seems to be even more strongly hindered in thin films of P3CF$_3$HT than in thin films of P3BrHT, it is still not completely suppressed. The P3CF$_3$HT films on graphene exhibit a dewetting behavior resulting in droplets of various heights. Therefore, it was not possible to determine whether a similar critical film thickness as in P3BrHT exists below which the P3CF$_3$HT films are completely face-on oriented.

Figure 4.5 d) shows the GIWAXS pattern of a 200 nm thick P3CNHT film on graphene. While a certain circular intensity distribution originating from randomly oriented crystals can be observed, no explicit (h00) reflections on the meridian are visible. Note, that the edges of this sample were removed with a scalpel prior to the GIWAXS measurement since the edges were significantly thicker than 200 nm as a result of the spin-coating process used to deposit the films on the substrate (see Appendix B for more details). Overall, the GIWAXS pattern in figure 4.5d) unambiguously proves that complete suppression of the formation of edge-on crystals in P3ATs films of upto 200 nm can be achieved through chemical modifications of the end groups of the side chains. Furthermore, the clear correlation between the decreasing intensity of (h00) peaks from edge-on crystals with increasing polarity of the end group of the side chain is in line with the hypothesis that edge-on oriented crystallization at the interface to vacuum can be suppressed by increasing the dipole moment of the endgroup of the side chains in P3ATs. In combination with a substrate inducing face-on orientation, such as graphene, this allows to obtain uniform face-on crystal orientation in films with thicknesses relevant for applications.

The surface morphology of the different P3AT films crystallized on graphene were investigated through AFM measurements of which representative images are shown in figure 4.5 e-h). All four investigated P3ATs clearly exhibit elongated lamellar crystals. The lamellae visible in the P3HT and P3BrHT films on graphene show no clear preference for specific in-plane orienteations (cf. fig. 4.5 e-f). In contrast, the lameallae visible at the upper interface in thin P3CNHT films on graphene of less than 30 nm thickness (cf. fig. 4.5 h) show a clear threefold symmetry matching the threefold symmetry of the underlying graphene substrate. This proves, that P3CNHT crystallizes epitaxially on graphene and therefore, that the face-on orientation is indeed induced by the graphene substrate. Note, that the clear threefold symmetry of the lamellae seems to get lost during the further vertical growth of the lamellae and is not observable in thicker films of P3CNHT.

Figure 4.5 g) shows the surface morphology of a P3CF$_3$HT film on graphene after crystallization from the melt. While directly after spin-coating and prior to the crystallization from the melt the film was smooth and had a thickness of 25 nm, during the crystallization from the melt the film formed droplets of different heights. The clearly visible droplet illustrates the dewetting behavior observed in all investigated P3CF$_3$HT films on graphene after crystallization from the melt. The average droplet height for this sample was determined to be about 85 nm. Interestingly, as visible in the AFM image, the droplets are surrounded by epitaxially crystallized lamellae similar to those observed in the P3CNHT film. This observation strongly suggests that molten P3CF$_3$HT dewetted from a thin layer of its own epitaxially aligned crystals, a phenomenon also observed in other polymers [151, 66, 152] and termed autophobic dewetting [153]. In contrast to the lamellae in the continuous film surrounding the droplet, the lamellae on top of the droplet are shorter and randomly oriented. This morphology is quite similar to the morphologies found in the edge-on oriented upper layers of the P3HT and P3BrHT films. Thus, the lamellae on top of the P3CF$_3$HT droplets are likely the origin of the scattering signal of edge-on oriented crystals observed in the GIWAXS measurement.

As the influence of the interface to vacuum on the crystal orientation is largely suppressed in the thin films of P3CF$_3$HT and P3CNHT, the crystal orientation in these films is almost completely determined by the epitaxial crystal growth at the interface to graphene and thus by the interactions with the substrate. To determine whether the formation of edge-on oriented crystals is still significantly suppressed on substrates that do not induce epitaxial crystallization, a series of thin films on silicon substrates were investigated. These investigations were limited to the P3CF$_3$HT and P3CNHT polymers as the CF$_3$- and the CN-group evidently had the largest effect on the crystal orientation in thin films on graphene. The used silicon substrates feature a thin (≈ 2 nm to 3 nm) amorphous layer of naturally oxidized silicon oxide eliminating the possibility for epitaxial growth. Additionally, similar silicon substrates were previously shown to have no effect on the crystal orientation in thin films of P3HT [31].

Figure 4.6 a-c) shows representative GIWAXS patterns for thin films of P3HT, P3CF$_3$HT and P3CNHT on silicon substrates crystallized from the melt. The thicknesses of the corresponding thin films are in the range of 80 nm to 120 nm. The GIWAXS pattern
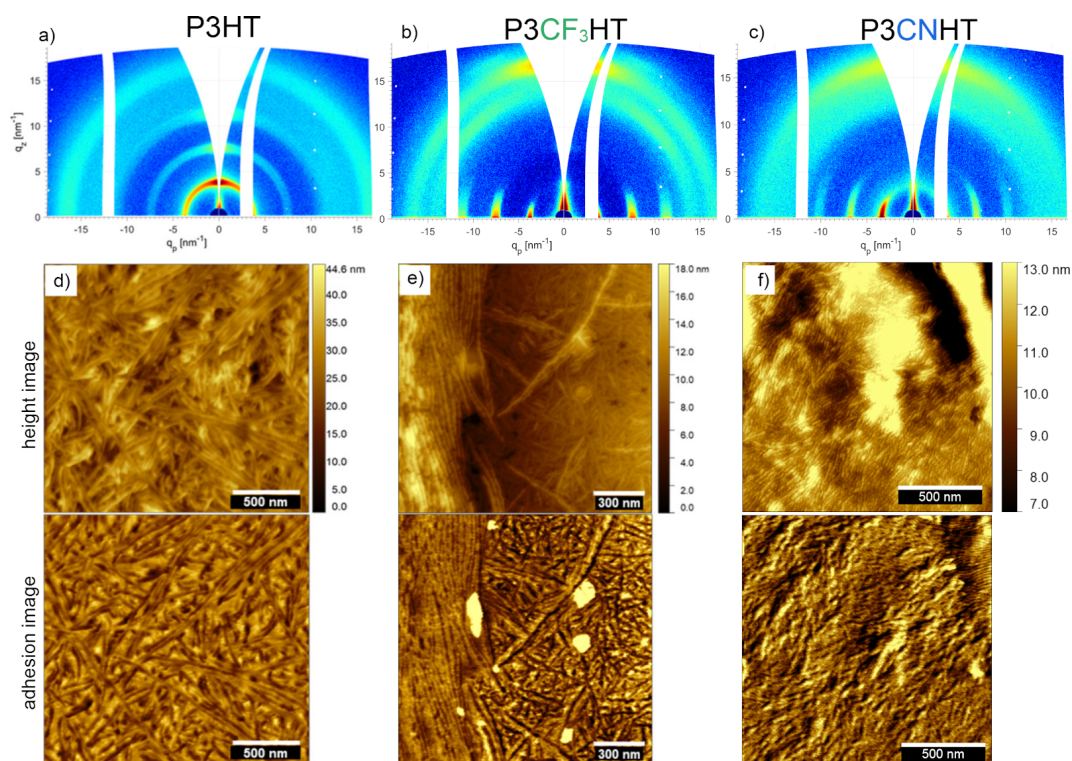
Figure 4.6.: Crystal orientation and surface morphology in thin P3AT films on silicon substrates. GIWAXS patterns measured at an angle of incidence $\alpha_i = 0.18°$ of a) a 120 nm thick P3HT film, b) a 85 nm thick P3CF$_3$HT film and c) a 81 nm thick P3CNHT film. AFM height (upper row) and adhesion (lower row) images of the corresponding films of d) P3HT, e) P3CF$_3$HT and f) P3CNHT. The imaged area in all AFM images was $1.5 \times 1.5\,\mu m^2$. Adapted with permission from [138]. Copyright 2024 American Chemical Society.

of the P3HT film shows a circular distribution of (h00) reflections with significantly higher intensity on the meridian indicating a dominant edge-on orientation with an additional amount of unoriented crystals.

The P3CNHT film on silicon shows very intense (h00) reflections on the horizon and an additional but weaker circular intensity distribution of the (100) reflection indicating a strong preference for face-on orientation and a small amount of randomly oriented crystals (cf. fig. 4.6 c). The absence of any strong (h00) reflections on the meridian indicates a complete suppression of the formation of explicitly edge-on oriented crystals. The thin film of P3CF$_3$HT also shows a very dominant face-on orientation. Unlike P3CNHT however, it shows no signs of unoriented crystals and instead shows weak (h00) reflections on the meridian evidencing the presence of edge-on oriented crystals (cf. fig. 4.6 b). Therefore, while the formation of edge-on crystals in P3CF$_3$HT has clearly been hindered significantly compared to P3HT, it has not been fully suppressed in. Also note, that the distributions of crystal orientations in thin films of P3CF$_3$HT and P3CNHT on silicon substrates are remarkably similar to the distributions of crys-

tal orientations observed in their thin films on graphene despite the lack of epitaxy on silicon substrates.

The AFM images shown in figure 4.6 d-f reveal the surface morphology of the three P3AT films on silicon substrates. The P3HT films on silicon exhibit randomly oriented elongated lamellae which is qualitatively similar to the morphology found in the P3HT films on graphene. In contrast, and unlike their counterparts on the graphene substrates, the films of P3CF$_3$HT and P3CNHT on silicon substrates show no sign of epitaxial crystal growth. The lack of epitaxial crystal growth demonstrates that despite the similar distributions of crystal orientations in the P3CF$_3$HT and P3CNHT films on the silicon and graphene substrates, the underlying crystallization mechanisms are clearly different. As epitaxy is commonly observed in prefreezing of polymers, the observed epitaxy in thin films of P3CNHT and P3CF$_3$HT on graphene may indicate that the face-on crystals on graphene are possibly induced by prefreezing [66].
As seen in figure 4.6 f), the P3CNHT film shows a spruce-like lamellar morphology which is typical for spherulitic growth. Since spherulites form through nucleation and growth and the crystals in the observed sphreulitic structures are clearly oriented, they are likely induced by heterogeneous nucleation at the interface to the silicon substrate. The P3CF$_3$HT films on silicon show a behavior similar to dewetting upon crystallization from the melt, although a certain amount of material remains in the seemingly dewetted areas (cf. right side of fig. 4.6 e). The surface morphology observed in different P3CF$_3$HT films on silicon will be discussed in more detail as it strongly depends on film thickness and the applied thermal treatment.

4.3. Influence of Competing Crystallization Mechanisms

The formation of edge-on and face-on oriented crystals is unavoidably accompanied by different crystal lattice planes being in contact with the substrate and/or the interface to vacuum. In the case of edge-on crystals the contact plane to the substrate and/or the interface to vacuum is the (100) plane while in the case of face-on crystals it is the (020) plane. As the (100) and (020) planes differ in their chemical composition and therefore likely also in their surface energies, both, the crystal growth kinetics and the onset of crystallization upon cooling from the melt likely differ between edge-on and face-on crystals. This implies, that in thin films where a competition between the formation and growth of edge-on and face-on oriented crystals exists, the dominating crystal orientation can strongly depend on the choice of crystallization conditions.

The results presented in section 4.2 show that in P3CF$_3$HT a certain competition between the formation of edge-on and face-on crystals is present while in P3CNHT the formation of explicitly edge-on oriented crystals has seemingly been suppressed completely. To elucidate the effect of the competing crystallization processes on the crystal orientation and surface morphology in thin films of P3CF$_3$HT and to verify that the suppression of explicitly edge-on oriented crystals in P3CNHT is not just the result

of coincidentally favorably chosen crystallization conditions, a series of thin films of P3CF$_3$HT and P3CNHT subjected to varying crystallization conditions is investigated.

As the observed strong dewetting of P3CF$_3$HT films on graphene made the controlled preparation of comparable thin film samples unfeasible, the investigations of P3CF$_3$HT are limited to P3CF$_3$HT films on silicon substrates.

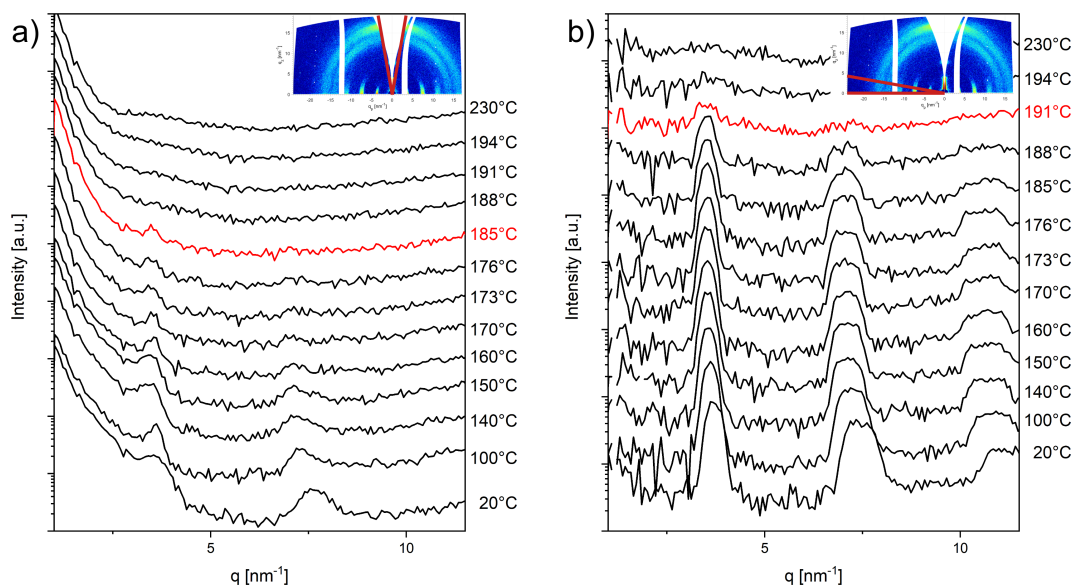### 4.3.1. Crystal Orientation and Morphology of Thin Films of P3CF$_3$HT

Figure 4.7.: Line profiles along a) the meridian and b) the horizon extracted from GIWAXS patterns of a 105 nm thick P3CF$_3$HT film on silicon, measured at different temperatures during cooling from the melt. The angular integration ranges used to extract the line profiles in the different directions are indicated by the red cones in the inset GIWAXS patterns in the upper right corners of the two graphs. The line profiles in which the (100) reflection is first visible are highlighted in red.

To verify that the formation of edge-on and face-on oriented crystals in thin films of P3CF$_3$HT differ in their onsets of crystallization temperature dependent GIWAXS measurements were conducted. For these measurements a 105 nm thick film was cooled from the melt via multiple isothermal steps during which GIWAXS patterns were recorded. For each step the sample was kept at a constant temperature for 1 h(= 30 min equilibration/annealing+30 min measurement). Measurement steps were performed every 3 K (200 °C - 170 °C) or 10 K (170 °C - 100 °C) with a cooling rate of 1 K/min between steps. A graph of the exact temperature program is shown in figure 4.9i) (Program P4). Figure 4.7 shows the line profiles along the meridian and the horizon extracted from these GIWAXS patterns. The line profiles along the meridian and along the horizon show the (h00) reflections of the edge-on and face-on crystals respectively.

Notably, the (100) reflection of face-on oriented crystals is first visible in the measurement at 191 °C while the (100) reflection of the edge-on oriented crystals becomes visible only upon reaching 185 °C. Comparing the intensities of the face-on (h00) reflections at different temperatures a continuous increase of intensity is evident at least upto the measurement at 176 °C. As the intensity is proportional to the number of scatterers it can be concluded that the sample had not yet fully crystallized at 185 °C enabling the formation of edge-on oriented crystals in the remaining melt. Similarly, the intensity of the edge-on (h00) reflections increases at least upto the measurement at 150 °C which is more than 30 K below the temperature at which the edge-on (100) reflection first appeared.

The observed differences in the onsets of the formation of edge-on and face-on oriented crystals and the sufficiently slow crystallization rate at elevated temperatures open up two possible approaches to influencing the distribution of crystal orientations in thin films of P3CF$_3$HT.

The first option is to vary the thickness of the films while keeping the cooling procedure used to crystallize the films from the melt constant. As the competing crystal orientations are induced at the upper and lower interface of the film, it can be expected that changing the distance between the interfaces will affect the resulting distribution of crystal orientations. Similar observations were made by Dolynchuk et al. for thin P3BrHT films on graphene substrates. They reported that films of upto 26 nm thickness exclusively contained face-on oriented crystals while in thicker films the fraction of edge-on crystals increased with film thickness [34].

The second option is to crystallize films of comparable thicknesses using different cooling procedures. Since the formation of edge-on and face-on crystals are induced by different crystallization phenomena the involved kinetics in both likely differ too. Thus, changing the temperature program by which the samples are crystallized should result in a change in the distribution of crystal orientations as well. In the following the effects of both approaches on the distribution of crystal orientations and the surface morphology of thin films of P3CF$_3$HT on silicon substrates are investigated.

Figure 4.8 shows the results of GIWAXS, POM and AFM measurements on films of different thicknesses crystallized from the melt following the same cooling program. As seen in the GIWAXS images shown in figure 4.8 a-d) the distribution of crystal orientations changes gradually with increasing film thickness from an almost complete edge-on orientation to a mixed edge-on and face-on orientation to an almost complete face-on orientation. Therefore, as expected, the dominant crystal orientation in thin films of P3CF$_3$HT can be modified by varying the film thickness.

The morphologies of the films as observed with optical microscopy (cf. figure 4.8 e-h) and AFM (cf. figure 4.8 i-l) reveal that the crystallization of P3CF$_3$HT in thin films is rather complex and likely multiple competing processes are involved.

In the two thinner films multiple birefringent crystalline stems separated by non-birefringent areas are visible. Note that the larger dark spots in the 29 nm film were already visible in the films prior to crystallization from the melt and are likely thickness inhomogenities resulting from the spin coating process. As seen from the AFM images (cf. 4.8 i), the non-birefringent areas show a nanofibrillar or whisker morphology of
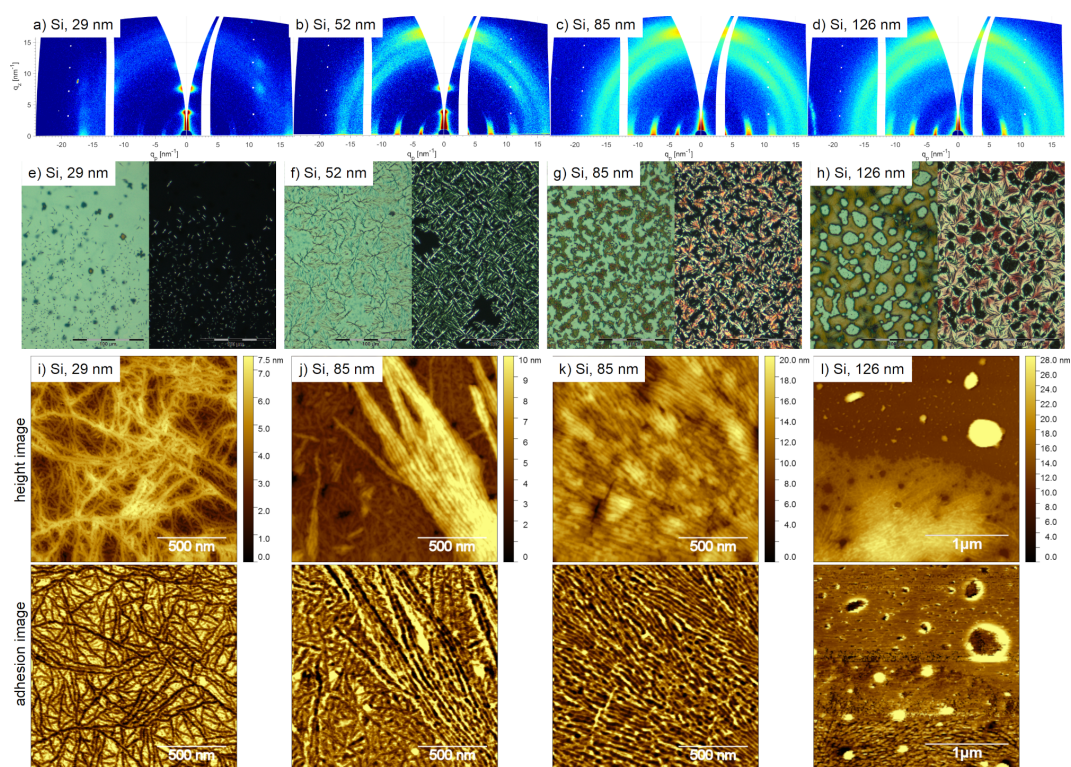
Figure 4.8.: a-d) GIWAXS patterns of P3CF$_3$HT films of different thicknesses on silicon substrates crystallized from the melt using the same cooling program (230 °C to 120 °C with 1 K/min, 120 °C to 20 °C with 10 K/min). e-h) Corresponding optical microscopy images of the same films. Left and right halves of the microscopy images depict the same regions recorded with open (left) and crossed polarizers (right). i-l) AFM height (upper row) and adhesion (lower row) images of the same films. Note, that j) was recorded in one of the non-birefringent areas and k) was recorded in one of the birefringent areas of the film shown in g). Measured film thicknesses are indicated in the upper left of the measurements.

elongated, mostly individual crystalline lamellae with no clear orientational correlation between different lamellae. Similar nanofibrillar morphologies have been reported in P3HT films crystallized from solution [154, 155]. Evidently, the lack of birefringence in these areas is not caused by the absence of crystalline material, but by the isotropic orientation of the crystalline lamellae on the micrometer scale.

The large crystalline stems visible in the POM images of the two thinner films are comprised of multiple elongated lamellae running in parallel. Based on the very dominant edge-on orientation of the 29 nm film (cf. fig. 4.8 a) it is evident that the nanofibrillar morphology is comprised of edge-on oriented crystals. In contrast, the birefringent crystalline stems are comprised of face-on oriented crystals as can be concluded from the measurements on the 52 nm film where the increased number and size of birefringent crystalline stems (cf. fig. 4.8 f) results in an increased ratio of face-on oriented crystals

as observed in the GIWAXS measurement (cf. fig. 4.8b).

The two thicker films show a drastically different morphology than the two thinner films. The optical microscopy images (cf. fig. 4.8 g,h) show that instead of individually discernible birefringent crystalline stems whole areas have become birefringent. On the nanometer scale the birefringent areas show a morphology of parallel crystalline lamellae that slightly splay outwards as is typical for spherulitic growth (cf. fig. 4.8k). The observation of spherulitic structures is an indication, that the face-on oriented crystals in P3CF$_3$HT on silicon substrates are induced through heterogeneous nucleation at the interface to the substrate.

Additionally, the films appear to have partially dewetted. Interestingly though, the majority of the areas that appear dewetted in the optical microscopy images are still covered by a thin film of crystallized polymer, as seen in AFM images (cf. fig. 4.8j) and thus the majority of the areas are actually only pseudo-dewetted [156, 157, 158]. This thin remaining film has a morphology quite similar to that of the 29 nm film as smaller crystalline stems comprised of multiple parallel lamellae surrounded by nanofibrillar structures can be observed. A complete dewetting as indicated by smooth and featureless areas in the AFM images (representing the surface of the underlying silicon substrate) could only be observed at a few positions of these films (cf. fig. 4.8l).

Figure 4.9 shows the results of GIWAXS, POM and AFM measurements on P3CF$_3$HT fims on silicon of similar thickness crystallized from the melt using different cooling programs. The cooling programs used are labeled P1-P4 and are plotted in figure 4.9 i). Note that the film crystallized using cooling program P2 is the same sample also shown previously in the series of films investigating the influence of different film thicknesses.

Interestingly, the sample that was cooled quickly using program P1 (210 °C to 20 °C with 10 K/min) and the sample cooled a bit slower using program P2 (230 °C to 120 °C with 1 K/min, 120 °C to 20 °C with 10 K/min), as well as the sample cooled very slowly via multiple isothermal steps (P4), all show a dominant face-on orientation (cf. fig. 4.9 a,b,d). At a first glance, this seems to suggest that the crystal orientation in P3CF$_3$HT films on silicon is mostly independent of the cooling program. As this is contradictory to the expectations based on the different onsets of formation of edge-on and face-on crystals, a sample was crystallized with cooling program P3 which was specifically designed to increase the amount of edge-on oriented crystals. P3 was derived from P2 by inserting a series of isothermal steps in a temperature range (175 °C - 160 °C) where the formation and growth of edge-on oriented crystals was observed (cf. fig. 4.7) followed by rapid cooling (10 K/min) of the sample to 20 °C.

As seen from the GWIAXS measurement (cf. fig. 4.9 c) the cooling program P3 did indeed significantly increase the amount of edge-on oriented crystals resulting in a mixed distribution of edge-on and face-on crystals. This indicates once again, that the distribution of crystal orientations in P3CF$_3$HT depends on a complex interplay of multiple processes.

This interpretation is further supported by the drastically different morphologies of the films as observed in POM and AFM images. The POM images of the films cooled
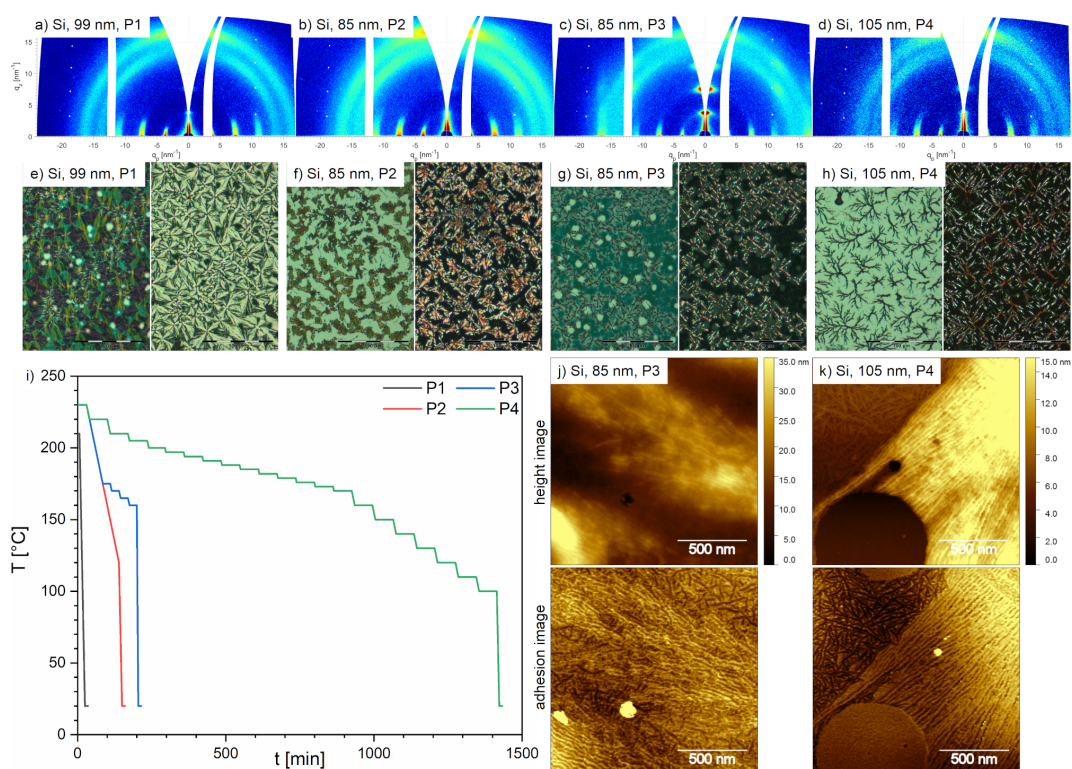
Figure 4.9.: a-d) GIWAXS patterns of P3CF$_3$HT films of similar thicknesses on silicon substrates crystallized from the melt using different cooling programs. e-h) Corresponding optical microscopy images of the same films. Left and right halves of the microscopy images depict the same regions recorded with open (left) and crossed polarizers (right). i) Plot of the different cooling programs (P1-P4) used to crystallize the samples. j-k) AFM height (upper row) and adhesion (lower row) images of the same films. Measured film thicknesses and employed cooling programs are indicated in the upper left of the measurements.

with P1 and P2 (cf. fig. 4.9 e,f) show large birefringent areas filled with spherulites (cf. fig. 4.8 k) for AFM images of film cooled with P2). But while the sample cooled with P1 shows only a few small holes where the film has dewetted, the dewetting (or pseudo-dewetting) in the film cooled a bit slower with program P2 is more pronounced. In contrast, the film cooled via multiple isothermal steps using program P4 shows a completely different morphology (cf. fig. 4.9 e,f) consisting of large crystal stems with several branches and apparently dewetted areas in between. As seen from AFM images (cf. fig. 4.9 k) most areas that appear dewetted in POM images are actually just pseudo-dewetted as they are still covered by a crystalline polymer film with a nanofibrillar morphology. True dewetting resulting in featureless holes in the film as seen in the lower left corner of figure 4.9 k) is only observed in a few positions.

The large crystalline structures, which in their shape resemble tree canopies, look somewhat similar to dendritic crystals that have been observed in thin films of other polymers such as PCL and PEO [159, 160, 161]. But, these kind of dendritic crystals

are single flat-on oriented lamellae (i.e. chain-on oriented crystals) [162] that grow into these irregular shapes as a consequence of diffusion limited aggregation [163, 164, 165, 166]. In contrast, the structures observed in the P3CF$_3$HT films clearly consist of multiple parallel edge-on oriented lamellae (in this case face-on oriented crystals). Therefore, these structures are more of an incomplete spherulite formed due to a very low branching density and a very limited degree of splaying of lamellae. Thus, the face-on crystals in P3CF$_3$HT films on silicon substrates vary between two different growth forms depending on crystallization temperature. When crystallized closer to the melting point the crystals grow with little branching and splaying resulting in large crystal stems with few large branches consisting of multiple parallel lamealle. Upon further undercooling and an increasing frequency of lamellar branching [167, 168] the crystals transition to a common spherulitc growth form.

The film crystallized by cooling with P3 has a quite remarkable morphology (cf. fig. 4.9 g). In large parts the sample is still covered by a non-birefringent film with only a few visible holes. While the holes are a bit larger, the number of holes is approximately comparable to the number of holes found in the film cooled with P1 indicating that the dewetting has not significantly progressed compared to the film cooled with P1 despite the inserted isothermal steps at elevated temperatures. The extent of dewetting in this sample was most likely not significantly hindered by the crystallization of the film as the temperature dependent GIWAXS measurements suggest that edge-on crystallization proceeds slowly in the temperature range of the inserted isothermal steps and therefore the film was likely still partially molten during the isothermal steps.

Additionally, the film features large crystal stems which are quite similar to, but less developed than the crystal structures found in the film cooled with P4. Interestingly, in the POM image the film in the immediate surrounding of these large crystal stems is somewhat brighter than the remaining film indicating a reduced film thickness. This can be interpreted as a depletion zone caused by material incorporation into the denser and likely higher crystal stems. Similar depletion zones around growing polymer crystals have been reported for other polymers such as PEO and iPS [169, 161, 170]. Nonetheless, as seen in the upper right corner of the AFM adhesion image in figure 4.9 j) and similar to previous observations the large crystal stems are still surrounded by a thinner film with a nanofibrillar morphology.

Recently, Majumder et al. reported on the vertical growth of poly(nonadecane methylphosphonate) crystals in thin films where the height of the crystals surpassed the initial thickness of the film by 100 times [171]. This lead to a widespread depletion of molten polymer in between the crystals in the sample and thus a reduction of the film thickness. Therefore, it seems plausible that depletion is also responsible for the large extent of pseudo-dewetting observed in the P3CF$_3$HT films cooled with P2 and P4. Although, as seen in the film cooled with P3, the depletion is likely not the only reason for the formation of the observed holes as not all holes are in immediate proximity to a large crystal stem.

Based on the results presented here it is not quite clear why the depletion leaves a thin layer of material behind. One possible explanation might be a lower chain mobility (i.e. an increased glass transition T_g) in very thin films due to adhesive forces between

the polymer chains and the silicon substrate as similar effects have been observed in other polymers [172]. Although this raises the question as to how this immobilized layer is then still able to form edge-on oriented crystals. Another possible explanation is, that the further progression of the depletion is limited by the formation and growth of edge-on oriented crystals upon reaching lower temperatures.

Overall, the apparent dewetting in thin films of P3CF$_3$HT is likely a result of both actual dewetting as well as material diffusion to the growing face-on crystals resulting in the formation and growth of depletion zones. The holes in the film where the bare silicon substrate is visible are likely a result of actual dewetting, while the pseudo-dewetted areas are likely mainly caused by depletion.

In summary, the following model for the development of crystal orientation and morphology in thin films of P3CF$_3$HT on silicon substrates upon cooling from the melt is proposed: At temperatures above the melting point dewetting of the molten film leads to the formation of holes. Upon Cooling the film to 191 °C heterogeneous nucleation of face-on oriented crystals at the interface to the silicon substrate occurs. In this temperature range the face-on crystals grow with little branching and splaying of lamellae. If given enough time this leads to the formation of large crystal stems consisting of multiple lamellae and the depletion of the surrounding melt. If instead cooled down further until the temperature of the film drops to 185 °C, edge-on crystals start forming and growing at the interface to vacuum. If kept in this temperature range, the formation of edge-on crystals in the depletion zones around the large face-on crystal stems prevents further diffusion of material to the face-on crystals and their growth is halted. When instead further cooling the sample before the edge-on crystals can grow further, the lamellae of the face-on oriented crystals start branching and splaying more and more resulting in the formation of spherulites.

4.3.2. Crystal Orientation and Morphology of Thin Films of P3CNHT

As seen from the measurements of P3CF$_3$HT films discussed above, if there is a competition between the formation of crystals of two different crystal orientations, the final distribution of crystal orientations can sensitively depend on the crystallization conditions such as the film thickness and the cooling program used to crystallize the samples from the melt. To verify that the formation of explicitly edge-on oriented crystals is truly suppressed in P3CNHT and thus there is no competition between the formation of edge-on and face-on oriented crystals, a series of P3CNHT films of different thicknesses and crystallized from the melt using different cooling programs on both graphene and silicon substrates were investigated.

Figure 4.10 summarizes the results of the measurements on thin P3CNHT films on graphene substrates. The different temperature programs used to crystallize the films from the melt are labeled as P1 to P3 and are plotted in figure 4.10 k). In cooling program P1 the samples were cooled from 210 °C to 20 °C with 10 K/min. In program P2 the samples were cooled down to 120 °C with 1 K/min and then to
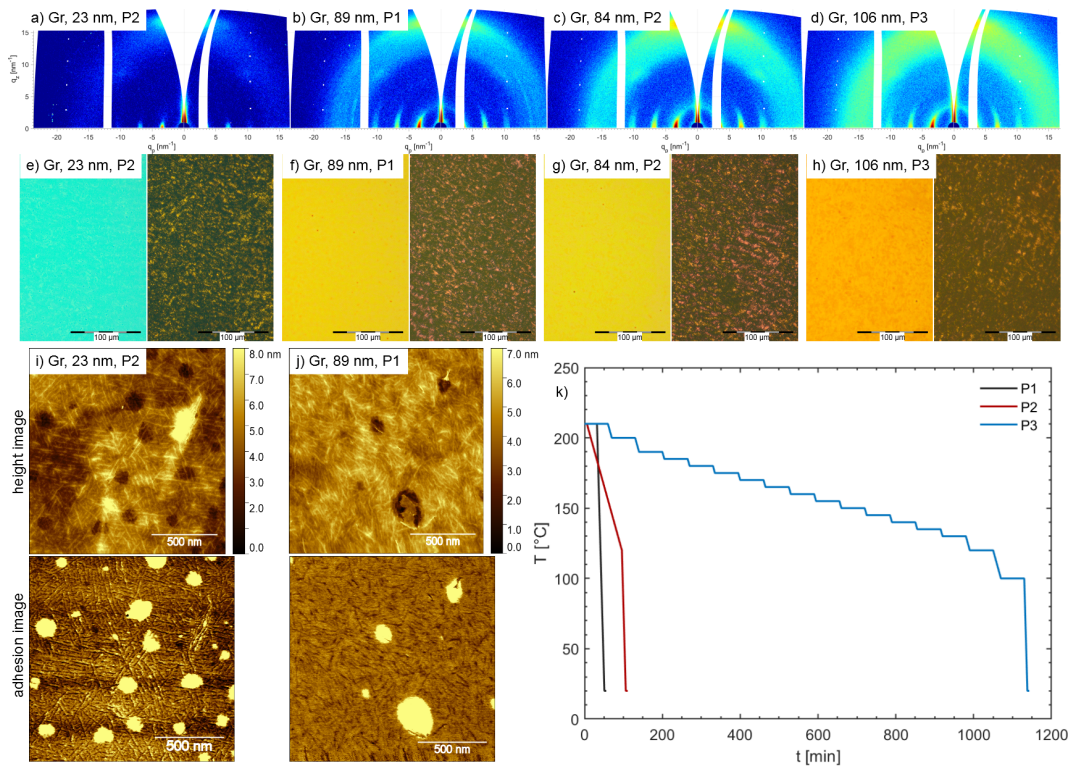
Figure 4.10.: a-d) GIWAXS patterns of P3CFNHT films on graphene substrates crystallized from the melt. Films measured in a) and c) had different thicknesses but were crystallized using the same cooling program. Films measured in b-d) had similar thicknesses but were crystallized using different cooling programs. e-h) Corresponding optical microscopy images of the same films. Left and right halves of the microscopy images depict the same regions recorded with open (left) and crossed polarizers (right). i-j) AFM height (upper row) and adhesion (lower row) images of the same films. k) Plot of the different cooling programs (P1-P3) used to crystallize the samples. Measured film thicknesses and employed cooling programs are indicated in the upper left of the measurements.

20 °C with 10 K/min. In program P3 the samples were cooled via multiple isothermal steps of 60 min each. As seen from the GIWAXS patterns (cf. fig. 4.10 a-d) all films show an almost complete face-on orientation and neither the film thickness nor the employed cooling program had any significant effect on the distribution of crystal orientations. While especially in the thicker films there is a small fraction of randomly oriented crystals as seen from the weak circular intensity distribution component of the (100) reflection, no sign of explicitly edge-on oriented crystals is observed. The optical microscopy images (cf. fig. 4.10 e-h) of all films show rather smooth films with an irregular birefringence pattern and no sign of dewetting. The AFM images of thin films (<30 nm) show that the lamellae are arranged in a clear threefold symmetry (cf. fig. 4.10 i) indicating that the face-on crystals have grown epitaxially on graphene.

While the crystals in the thicker films are still strongly face-on oriented the in-plane orientation of the growing lamellae is apparently lost at a certain distance from the graphene substrate as the clear threefold symmetry of the lamellae is not visible at the surface of thicker films (cf. fig. 4.10 j).
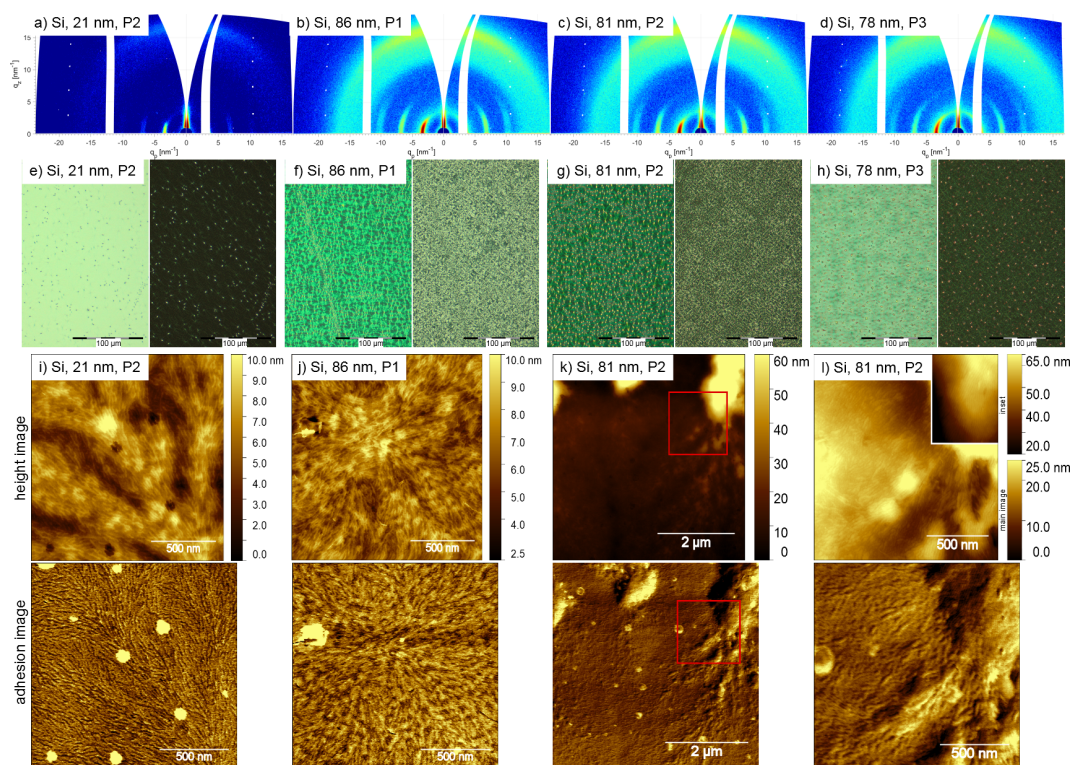

Figure 4.11.: a-d) GIWAXS patterns of P3CFNHT films on silicon substrates crystallized from the melt. Films measured in a) and c) had different thicknesses but were crystallized using the same cooling program. Films measured in b-d) had similar thicknesses but were crystallized using different cooling programs. e-h) Corresponding optical microscopy images of the same films. Left and right halves of the microscopy images depict the same regions recorded with open (left) and crossed polarizers (right). i-l) AFM height (upper row) and adhesion (lower row) images of the same films. AFM image in l) shows an enlarged view of the area in the red square in k). The inset in l) shows the underlying area in a different height/color scale. Measured film thicknesses and employed cooling programs are indicated in the upper left of the measurements.

Figure 4.11 summarizes the results of the measurements on thin P3CNHT films on silicon substrates. The same cooling programs (P1-P3) used to crystallize the P3CNHT films on graphene were also used to crystallize the P3CNHT films on silicon substrates. Similar to the films on graphene, all films on silicon show an almost complete face-on orientation with only a small additional fraction of randomly oriented crystals (cf. fig. 4.11 a-d). Again, neither the film thickness nor the employed cooling programs had any significant effect on the distribution of crystal orientations. In contrast, the morphologies of the films do show certain difference as observed by POM and AFM.

In the thinnest film small birefringent crystal stems are visible that look quite similar to the crystal stems observed in the thinnest P3CF$_3$HT film on silicon substrates (cf. fig. 4.11e and 4.8e). The film in between these small crystal stems is only weakly birefringent. However, as seen from the AFM image shown in figure 4.11i) the film in between the small crystal stems is also covered by crystalline lamellae. In the three thicker films a multitude of overlapping maltese cross patterns can be seen in the microscopy images with crossed polarizers (cf. fig. 4.11f-h), indicating that the crystalline lamellae in these films are organized in spherulites. The AFM images of these films show branching and outward splaying lamellae confirming the spherulitic growth of the crystalline lamellae (cf. fig. 4.11j). The observation of spherulitic structures again indicates that the face-on crystals in P3CNHT on silicon substrates are induced through heterogeneous nucleation at the interface to the substrate. Interestingly, the two more slowly cooled films (P2,P3) feature a series of small inhomogeneities as seen by the yellowish and reddish spots found in the centers of many of the spherulites in the POM images (cf. fig. 4.11g,h). The AFM measurements reveal that these inhomogeneities are comprised of multiple parallel lamellae that have grown to be significantly higher than the surrounding film (cf. fig. 4.11k,l). The morphology of elongated parallel lamellae with little branching and splaying is similar to the morphology found in the large crystal stems of slowly cooled P3CF$_3$HT films. Based on this, face-on oriented crystals of P3CNHT on silicon substrates also seem to grow with only little branching at higher temperatures forming larger crystal stems that can grow vertically to significantly exceed the original film thickness. Upon further cooling, the branching and splaying of lamellae increases and together with an increased lateral growth speed this results in the complete crystallization of the remaining film in the form of spherulites.

Overall, while their are certain similarities between the films of P3CF$_3$HT and P3CNHT crystallized from the melt on silicon substrates, the latter shows no signs of dewetting or pseudo-dewetting. Additionally, no influence of the film thickness or the cooling program on the distribution of crystal orientations in thin films of P3CNHT on both graphene and silicon substrates could be observed. Thus, it seems like the formation of edge-on crystals at the interface to vacuum has indeed been completely suppressed in P3CNHT.

4.4. Crystallization Mechanisms in Thin Films of P3CF$_3$HT and P3CNHT

The formation of oriented crystals in thin films of semicrystalline polymers supported on substrates is a result of interface-induced crystallization. Known mechanisms through which the interfaces can induce oriented crystallization are heterogeneous nucleation [173], prefreezing at the interface to the substrate [151, 66, 152, 174, 64] and surface freezing at the interface to vacuum [67, 68, 70, 71, 72, 73]. Additionally, a recently published simulation study by Qiu et al. suggests that heterogeneous nucleation at the interface to vacuum is also possible [175]. However, heterogeneous nucleation at

the interface has never been observed experimentally. Based on the results presented in section 4.3, it is possible to draw several conclusions regarding which crystal orientation is induced by which interface. The lamellae of face-on oriented crystals found in both the P3CF$_3$HT and P3CNHT films on graphene substrates are clearly grown epitaxially. Therefore, based on the observed lamellar morphology, it can be concluded that graphene induces face-on oriented crystallization in both polymers. Furthermore, as the nanofibrillar morphology found in thin films of P3CF$_3$HT is clearly comprised of edge-on oriented crystals and the same nanofibrillar morphology is found on top of the pseudo-dewetted droplets on graphene substrates, the edge-on oriented crystals in P3CF$_3$HT films are clearly induced by the interface to vacuum.

As speculated based on the observed spherulites in thin films of P3CF$_3$HT and P3CNHT on silicon substrates the face-on crystals in these films are likely formed through heterogeneous nucleation at the interface to the substrate. Additionally, it seems unlikely that for P3CF$_3$HT films on silicon the interface to vacuum would induce both edge-on and face-on oriented crystals making heterogeneous nucleation at the interface to the silicon substrate even more probably. Regrettably, a more reliable determination of the origin of face-on oriented crystals in P3CF$_3$HT films on silicon was not possible as surface sensitive GIWAXS measurements could not be performed due to the significant roughness of the films caused by the observed dewetting and pseudo-dewetting. It is however possible to determine which interface induces the face-on crystals in P3CNHT films on silicon substrates by performing surface sensitive GIWAXS measurements on the compared to P3CF$_3$HT much smoother films.
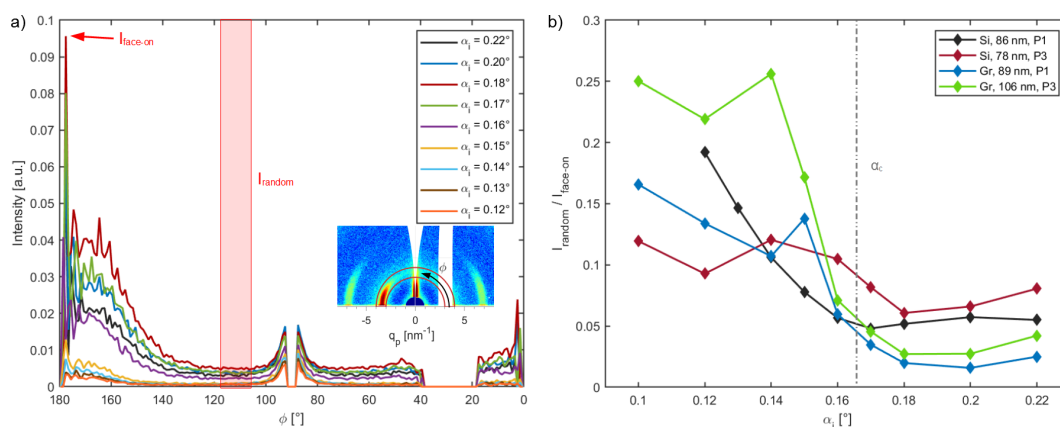
Figure 4.12.: a) Azimuthal intensity distribution of the (100) reflection extracted from GIWAXS measurements of a 86 nm thick P3CNHT film on a silicon substrate measured at different angles of incidence α_i. b) Ratio of intensities $I_{random}/I_{face-on}$ of the (100) reflection scattered from random and face-on oriented crystals as a function of α_i for different P3CNHT films. The red semi-circle in the inset GIWAXS image in a) shows the integration range used to extract the azimuthal intensity profiles. The dashed line in b) indicates the critical angle of P3CNHT ($\alpha_c \approx 0.165°$).

The surface sensitive GIWAXS measurements of the P3CNHT film were performed analogously to the measurements reported by Dolynchuk et al. on thin films of P3BrHT [34]. Figure 4.12a) shows exemplary azimuthal intensity distributions of the (100) reflection extracted from GIWAXS measurements at varying angles of incidence α_i from a 86 nm thick film on a silicon substrate. As Dolynchuk et al. evaluated the ratio of scattering intensities of edge-on and face-on oriented crystals and there are no explicitly edge-on oriented crystals in the P3CNHT films the ratio between the scattering intensity of random oriented crystals and face-on oriented crystals was evaluated instead. As illustrated in figure 4.12a) the maximum intensity in the angular range of 170° to 180° was taken as a measure for the scattering intensity of face-on oriented crystal $I_{face-on}$. The scattering intensity of the randomly oriented crystals I_{random} was determined by averaging the intensity in the angular range of 104.5° to 115.5°. The resulting ratio $I_{random}/I_{face-on}$ for two P3CNHT films on silicon as a function of the angle of incidence are plotted in figure 4.12b). For comparison, the plot also contains similar measurements on two P3CNHT films on graphene substrates.

With decreasing angle of incidence and thus with decreasing penetration depth of the primary beam the $I_{random}/I_{face-on}$-ratio of all four P3CNHT films increases on average. While this trend is least pronounced in the 78 nm thick film on silicon it is still evident that the average $I_{random}/I_{face-on}$-ratio increases when angle of incidence α_i drops below the critical angle α_c of the polymer. Overall, these measurements give a clear indication, that the fraction of random oriented crystals increases with increasing distance to the substrate. Therefore, it can be concluded that the formation of face-on oriented crystals in thin films of P3CNHT on silicon is induced by the interface to the silicon substrate.

Regarding the crystallization mechanism at the different interfaces, the spherulites observed both in P3CF$_3$HT and P3CNHT films on silicon are a clear indication that the face-on crystals in both polymers on silicon are formed through heterogeneous nucleation and growth. The random oriented crystals found in thin films of P3CNHT on both graphene and silicon substrates are most likely a result of both a loss of orientation upon further growth of the face-on oriented crystals, as well as homogeneous nucleation in the remaining melt upon reaching lower temperatures during the continuous cooling. In the temperature dependent GIWAXS measurements of the P3CF$_3$HT film on silicon the first indication of edge-on oriented crystals is visible at 185 °C (cf. fig. 4.7) which is below the bulk melting temperature of P3CF$_3$HT ($T_m = 212$ °C). Therefore, the edge-on crystals in thin films of P3CF$_3$HT are not formed by surface freezing, which happens above the bulk melting point, but instead most likely through heterogeneous nucleation at the interface to vacuum. Note however, that a potential layer of nematic liquid crystalline order in P3CF$_3$HT films induced by the vacuum interface above the bulk melting point cannot be excluded as this would not be visible in GIWAXS measurements.

To elucidate whether the face-on crystals in thin films of P3CNHT on graphene substrates are formed via heterogeneous nucleation or through prefreezing, temperature dependent GIWAXS measurements were performed in thin films on graphene and on silicon for comparison. The results of these measurements are shown in figure 4.13.
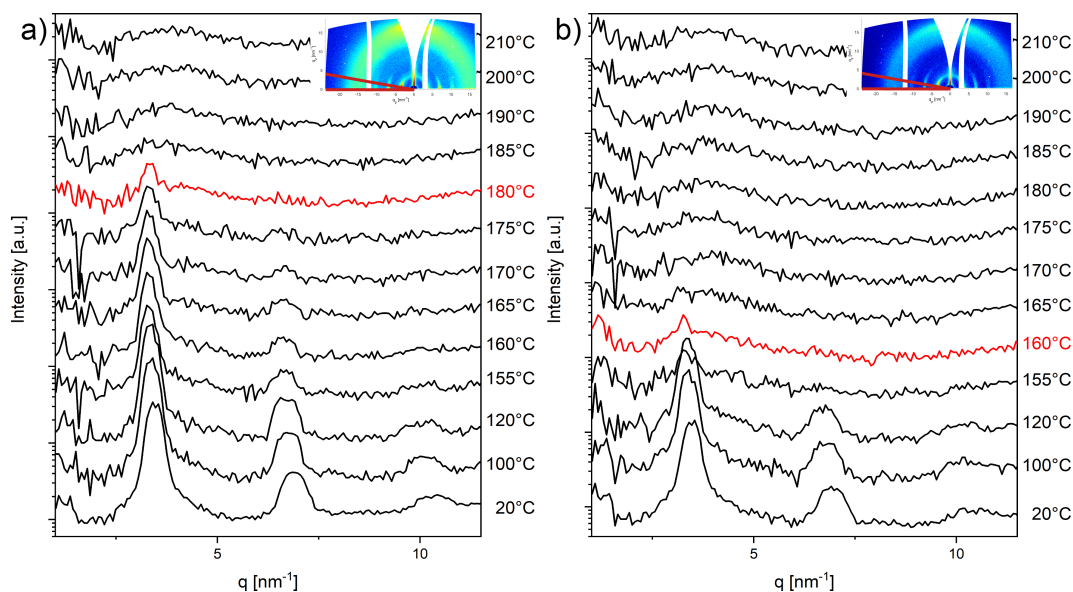
Figure 4.13.: Line profiles extracted from temperature dependent GIWAXS measurements of P3CNHT films on a) graphene and b) silicon substrates during cooling from the melt. The red cones in the insets illustrate the integration range used to extract the shown line profiles from the 2-dimensional GIWAXS patterns. The line profiles in which the (100) reflection is first visible are highlighted in red.

The (100) reflection of face-on oriented crystals on graphene is first visible in the measurement at $180\,^\circ$C while the (100) reflection of the face-on oriented crystals on silicon is only visible upon reaching $160\,^\circ$C. While the graphene substrate does induce crystallization at higher temperatures than the silicon substrate the onset of the formation of face-on oriented crystals is still below the bulk melting temperature of P3CNHT (T_m = $190\,^\circ$C) on both substrates. Thus, although the existence of a layer of nematic order above the bulk melting temperature cannot be excluded, based on the experimental results the face-on crystals in thin films of P3CNHT on graphene are most likely formed through heterogeneous nucleation and not through prefreezing.

Overall, these results are in line with the observations reported in literature for thin films of P3HT and P3BrHT, for which the vacuum interface induces face-on oriented crystals, while graphene substrates induce face-on oriented crystals [129, 32, 33, 31, 34].

4.5. Transferring Approach to Other Semiconducting Polymers

Within the previous sections it was demonstrated that the preferred crystal orientation of polythiophenes in thin films can indeed be controlled by increasing the polarity of the endgroup of the side chain. As there are many other semiconducting polymers
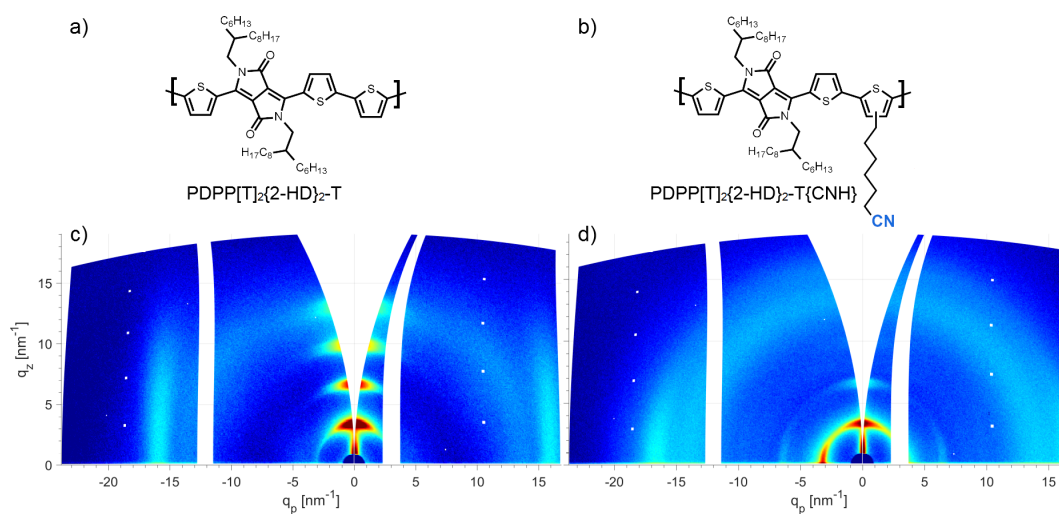
Figure 4.14.: Chemical structure of a) PDPP[T]$_2${2-HD}$_2$-T and b) PDPP[T]$_2${2-HD}$_2$-T{CNH}. GIWAXS patterns of ≈ 100 nm thick films of c) PDPP[T]$_2${2-HD}$_2$-T and d) PDPP[T]$_2${2-HD}$_2$-T{CNH} on silicon substrates after crystallization from the melt.

with better performance than polythiophenes it is of significant interest to determine, whether the approach of controlling the crystal orientation is unique to polythiophenes or if it is transferable to other semiconducting polymers.

As a first attempt to verify whether the crystal orientation in other semiconducting polymers can also be controlled through chemical modifications of the side chains, two diketopyrrolopyrrole-based copolymers were investigated. The chemical structure of the two PDPPs is shown in figure 4.14a,b). The first, PDPP[T]$_2${2-HD}$_2$-T or PDPP[T]$_2$-T, is a PDPP with exclusively alkyl side chains. As discussed in chapter 6 in more detail PDPP[T]$_2$-T, in contrast to P3HT, only has liquid crystalline order at room temperature. The second, PDPP[T]$_2${2-HD}$_2$-T{CNH}, is derived from PDPP[T]$_2$-T by adding a cyanohexyl side chain, equivalent to that in P3CNHT, to the thiophene comonomer. Films of both PDPPs were spin-coated onto silicon substrates and crystallized from the melt. The GIWAXS patterns of the PDPP[T]$_2$-T film shows a very dominant edge-on orientation with no explicitly face-on oriented crystals. In contrast, the PDPP[T]$_2${2-HD}$_2$-T{CNH} film shows a binary distribution of edge-on and face-on oriented crystals. This demonstrates, that while only one out of five end groups of the side chains in PDPP[T]$_2${2-HD}$_2$-T{CNH} carries a cyano group it was sufficient to alter the distribution crystal orientations significantly. Additionally, the general appearance of face-on oriented crystals in the PDPP[T]$_2${2-HD}$_2$-T{CNH} film on silicon is an indication that the cyano end group might generally enable face-on oriented crytallization at the interface to silicon substrates.

Further research is still needed to fully confirm the validity of the approach of increasing the polarity of the end groups of side chains to control the preferred crystal orientation in thin films of conjugated polymers other than polythiophenes. Nonetheless, these initial results obtained for PDPPs are quite promising.

4.6. Conclusion

In this chapter the influence of the polarity of the end groups of the side chains in polythiophenes on the the crystal orientation in thin films was investigated. It was demonstrated, that the formation of edge-on oriented crystals at the interface to vacuum is fully suppressed if the end groups of the side chains have a sufficiently large dipole moment. The suppression of the edge-on oriented crystals by more polar end-groups is attributed to an increase in the interfacial energy of the crystal-vacuum-interface making the edge-on crystallization at the vacuum interface thermodynamically unfavorable. For P3CNHT, the polythiophene with the most polar end group of the side chain, a dominant face-on orientation without any sign of explicitly edge-on oriented crystals could be achieved in films on graphene of upto 200 nm thickness. Furthermore, it was shown that the introduced polar end groups enabled heterogeneous nucleation of face-on oriented crystals at the interface to silicon substrates in P3CF$_3$HT and P3CNHT. This is in contrast to P3HT, for which the amorphous SiO$_2$ interface of the silicon substrates has no pronounced influence on the crystallization. The complete suppression of edge-on oriented crystals in films of device-relevant thicknesses combined with the expansion of the available substrates that induce face-on oriented crystallization is a significant step towards more efficient and cheaper organic photovoltaic devices.

Additionally, the influence of the polar end groups of the side chains on the crystal structure was investigated. All of the investigated polymers have either an orthorhombic (P3BrHT, P3CF$_3$HT) or monoclinic unit cell with only a small deviation of γ from 90° (P3HT, P3CNHT). Generally, the polar end groups of the side chains did not significantly affect the intermolecular ordering of the investigated polythiophenes.

Despite the limited effect of the polar end groups on the crystal structure, a reduction in crystallinity compared to P3HT was observed for all of the investigated polythiophenes. However, the reduction in crystallinity does not correlate with the strength of the dipole moment of the end group. Therefore, a high end group polarity itself does not necessarily result in a significant reduction in crystallinity. Thus, there might be other polar end groups that have less effect on the crystallinity of polythiophenes and furthermore, the same end groups might have a completely different effect on the crystallinity in other polymers.

It was also demonstrated, that the simultaneous presence of the competing edge-on and face-on oriented crystallization processes in P3CF$_3$HT results in a strong dependence of the distribution of crystal orientations and the film morphology on the crystallization conditions. Consequently, the resulting distribution of crystal orientations upon cooling from the melt can be changed from a dominant face-on orientation to a dominant edge-on orientation by a suitable choice of film thickness and employed cooling program.

Finally, initial results of a polydiketopyrrolopyrrole with partially polar end groups of the side chains were presented, indicating that the chosen side chain engineering strategy to control the crystal orientation in thin films is transferable to other semiconducting polymers.

Overall, the presented results demonstrate that introducing polar end groups to the alkyl side chains of polythiophenes is a valid approach to control the crystal orientation in thin films. While these results are promising, further research of other polar end groups is still needed to establish a broader catalog of suitable polar end groups, allowing to simultaneously optimize the crystal orientation and other material properties such as the crystallinity. Furthermore, the transferability of the approach presented here to other semiconducting polymers has to be investigated in more detail. Additionally, a more profound understanding of the required strength of the dipole moment and the fraction of side chains that have to carry polar end groups in order to successfully suppress the edge-on crystallization would certainly be beneficial for further optimization of material properties.

5. Influence of Ethylene Glycol Side Chain Linkage on Molecular Ordering and OECT Performance
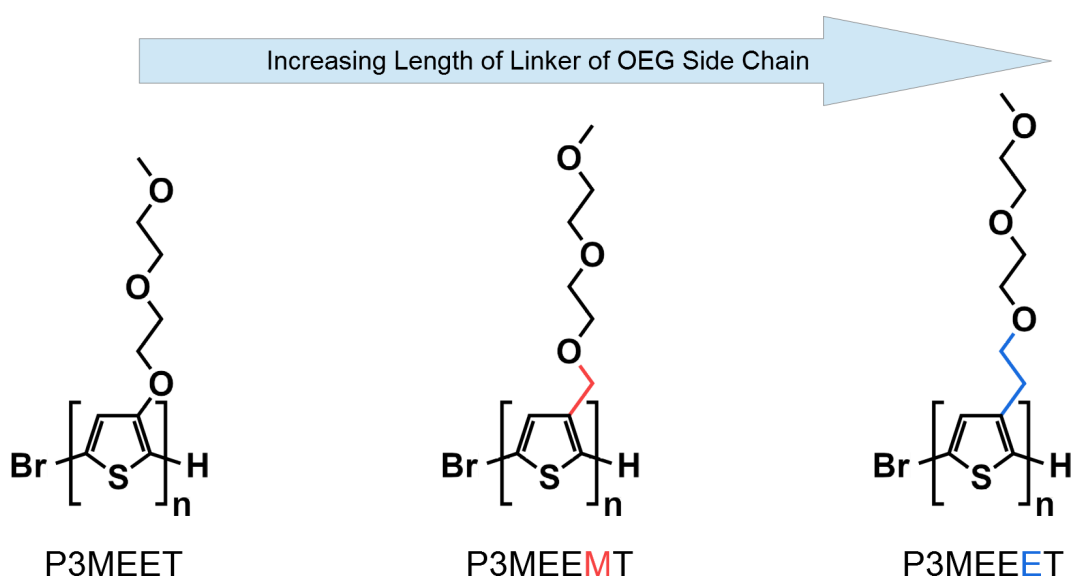

Figure 5.1.: Chemical structures of the investigated polythiophenes with differently linked ethylene glycol side chains. The methyl (red) and ethyl (blue) spacers are highlighted in color.

As described in section 2.3.3, OECTs operate in aqueous environment and have many different applications in bioelectronics related to detection and concentration measurement of ions and biomolecules. The active layer of OECT devices requires materials that enable both ionic and electronic transport (mixed conduction). Typical polymers used for the active layer of OECTs are semiconducting polymers like poly(3,4-ethylenedioxythiophene) doped with poly(styrene sulfonate)(PEDOT:PSS) or polyelectrolytes like poly(6-(thiophene-3-yl)hexane-1-sulfonate) tetrabutylammonium (PTHS). While conjugated polyelectrolytes are suitable candidates for mixed conduction, they suffer from the significant drawback of being water soluble. Therefore, polyelectrolytes require cross-linkers to be used in OECT devices [176, 177].

Another promising class of polymers for OECT devices are semiconducting polymers with hydrophilic ethylene glycol(EG) side chains. The introduction of EG side chains to conjugated polymers facilitates the penetration and the transport of aqueous ions into

the bulk film and therefore enables OECT operation [178, 179, 180]. Additionally, it has been shown that conjugated polymers with EG side chains exhibit high electrostability in aqueous environment [181] and do not require any cross-linkers for application in OECT devices [178]. The chemical structure of the conjugated backbones for polymers designed for bioelectronic applications is often based on polymers that have been known to perform well in other applications such as organic field effect transistors. Therefore, polythiophene derivatives are one of the most widely studied class of p-type seimconductors for bioelectronic applications. They benefit from a high crystallinity, good charge carrier mobility and a well established synthesis route (Kumada catalyst transfer polymerization) resulting in well defined polymers with narrow molecular weight distribution and high regioregularity [182, 183, 184]. One of the best performing polymers in this class is poly(2-(3,3'-bis(2-(2-(2-methoxyethoxy)ethoxy)ethoxy)-[2,2'-bithiophen]-5-yl)thieno[3,2-b]thiophene), p(g2T-TT) [178, 185, 186].

Dong et al. investigated two polythiophenes with EG side chains, one where the first oxygen of the EG side chain is directly attached to the thiophene backbone (P3MEET) and one where a methyl spacer was inserted between the oxygen and the backbone (P3MEEMT) [187]. As they investigated these polymers for potential use in battery applications, their main focus lay on the Li-ion conduction properties of these two polymers. Thus, they did not study mixed conduction properties or the performance of these polymers in OECTs or OFETs. Nonetheless, their study revealed significant differences in the ion conductivity of these two polymers, indicating that the linkage of the EG side chain to the thiophene backbone can have a strong influence on the properties of these polymers.

While it has been established, that functionalizing polythiophenes with EG side chains results in polymers well suited for application in OECT devices [188], the influence of the linkage of the EG side chain to the backbone has not yet been investigated in detail. Here, a series of three polythiophenes with differently linked EG side chains is investigated to elucidate the influence of the linkage of the EG side chain on the molecular ordering, mixed conduction properties and performance in OFET and OECT devices. The three investigated polymers are (cf. fig. 5.1): poly(3-[2-(2-methoxyethoxy)ethoxy]thiophene-2,5-diyl) (P3MEET) with no spacer between EG side chain and backbone, poly(3-[2-(2-methoxyethoxy)ethoxy]methyl-thiophene-2,5-diyl) (P3MEEMT) with a methyl spacer between EG sidechain and backbone and poly(3-[2-(2-methoxyethoxy)ethoxy]ethyl-thiophene-2,5-diyl) (P3MEEET) with an ethyl spacer between EG side chain and backbone. An overview of the molecular weight and the dispersity Đ of the three investigated polythiophenes with EG side chains is given in table 5.1 together with a summary of selected thermal and structural parameters discussed in the following sections. [1]

---

[1]The three polythiophenes with EG side chains were synthesized by Philip Schmode from the group of professor Mukundan Thelakkat from the University of Bayreuth as described in reference [189]. The size exclusion chromatography measurements, thermogravimetric analysis (TGA) measurements, spectroelectrochemistry (SEC) measurements, cyclic voltammetry (CV) measurements, swelling experiments, electrochemical impedance (EIS) measurements as well as OFET and OECT device preparation and characterization were also performed by Philip Schmode, partially in collabora-

Table 5.1.: Material Properties of the Investigated Polythiophenes with DEG Side Chains

Polymer	$M_n{}^a$ [kDa]	$Đ^a$	$T_{5\%}{}^b$ [°C]	$T_m{}^c$ [°C]	$\Delta H_m{}^c$ [J/g]	$\chi_c{}^d$ [%]	$d_{100}{}^e$ [Å]	$d_{020}{}^e$ [Å]
P3MEET	10	1.43	≈220	-	-	-	-	-
P3MEEMT	12	1.21	≈300	99	2.0	32	18.4	3.8
P3MEEET	13	1.08	≈370	122	8.6	58	20.7	3.7

[a] Determined by SEC with THF as eluent and against polystyrene standards. [b]Determined by TGA. [c]Determined by DSC. [d]Determined from WAXS measurements as described by Balko et al. [139] [e]Determined from WAXS measurements.

The results presented here reveal a strong dependence of the material properties on the linkage of the EG side chain, as most of the investigated properties show a monotonous dependence on the spacer length. Consequently, within the investigated series, P3MEEET with the ethyl spacer shows the highest crystallinity, the highest hole mobility in OFET devices and the highest transconductance and $\mu_{OECT}C^*$ product in OECT devices. The results presented in this section have partially been published in reference [189].

5.1. Thermal Stability and Phase Transitions

The effect of the different spacer length between the EG side chain and the thiophene backbone on the thermal stability and the phase behavior was studied using thermogravimetric anaylsis (TGA) and differential scanning calorimetry (DSC). The results of the TGA measurements are shown in figure 5.2a. The measurements clearly demonstrate that the thermal stability increases with increasing length of the alkyl spacer between the first oxygen of the EG side chain and the thiophene backbone. Within the investigated series P3MEET shows the lowest onset of degradation as a total mass loss of 5 wt% already occurs at approximately 220 °C. The low thermal stability of P3MEET can be attributed to the electron-withdrawing effect of the oxygen atom of the EG side chain being directly attached to the thiophene backbone. In contrast, P3MEEMT and P3MEEET, in which the first oxygen of the EG side chain is separated from the thiophene backbone by an alkyl spacer, show a higher thermal stability. Namely, a total mass loss of 5 wt% in P3MEEMT and P3MEEET occurs at temperatures of approximately 300 °C and 370 °C respectively.

Figure 5.2b shows the first cooling and second heating run of the three polythiophenes
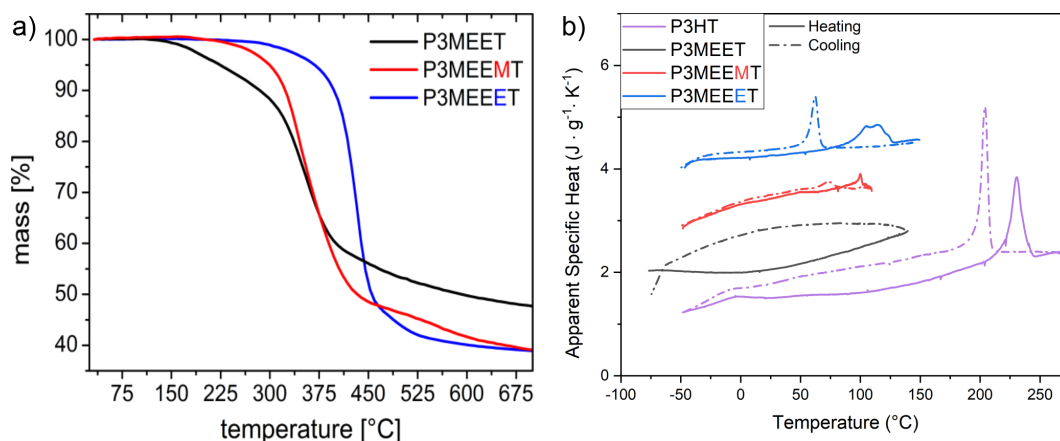
Figure 5.2.: a) TGA and b) DSC measurements of P3MEET (black), P3MEEMT (red) and P3MEEET (blue). Measurements were performed under nitrogen atmosphere with a cooling/heating rate of 10 K/min. The DSC curves show the first cooling (dashed) and the second heating run (solid) and are shifted vertically for better visibility. For comparison a DSC measurement of P3HT (purple) is also given. Panel a) reprinted with permission from [189]. Copyright 2020 American Chemical Society.

with EG side chains and P3HT for comparison. While for P3MEEET a clear melting peak can be observed at 122 °C and a weak melting peak can be observed for P3MEEMT at 99 °C, no clear sign of crystallization or melting could be observed for P3MEET indicating that it is amorphous. The observed melting enthalpies ΔH_m for P3MEEMT and P3MEEET are 2.0 J/g and 8.6 J/g respectively. Overall, melting point and melting enthalpy clearly increase with increasing spacer length.

In comparison to P3HT($T_m = 231$ °C, $\Delta H_m = 24.6$ J/g) the investigated polythiophenes with EG side chains all show significantly lower melting points and melting enthalpies, indicating that the replacement of the hexyl side chain with an EG side chain resulted in a reduced molecular order. The results of the TGA and DSC measurements are summarized in table 5.1.

5.2. Ordering and Thin Film Morphology

The ordering in bulk was investigated by a series of WAXS measurements recorded at different temperatures during a step-wise heating run. The scattering patterns obtained at various temperatures during a heating run (red curves), as well as before (black curve) and after (blue curve) the heating run are shown in figure 5.3a-c). For P3MEET and P3MEEMT the first heating run of the as prepared samples is shown as both did not crystallize upon cooling from the melt. For P3MEEET scattering patterns recorded in a second heating run after the sample had been crystallized by cooling from the melt are shown to emphasize its thermal stability.

The scattering patterns of P3MEET show no signs of increased order during or after
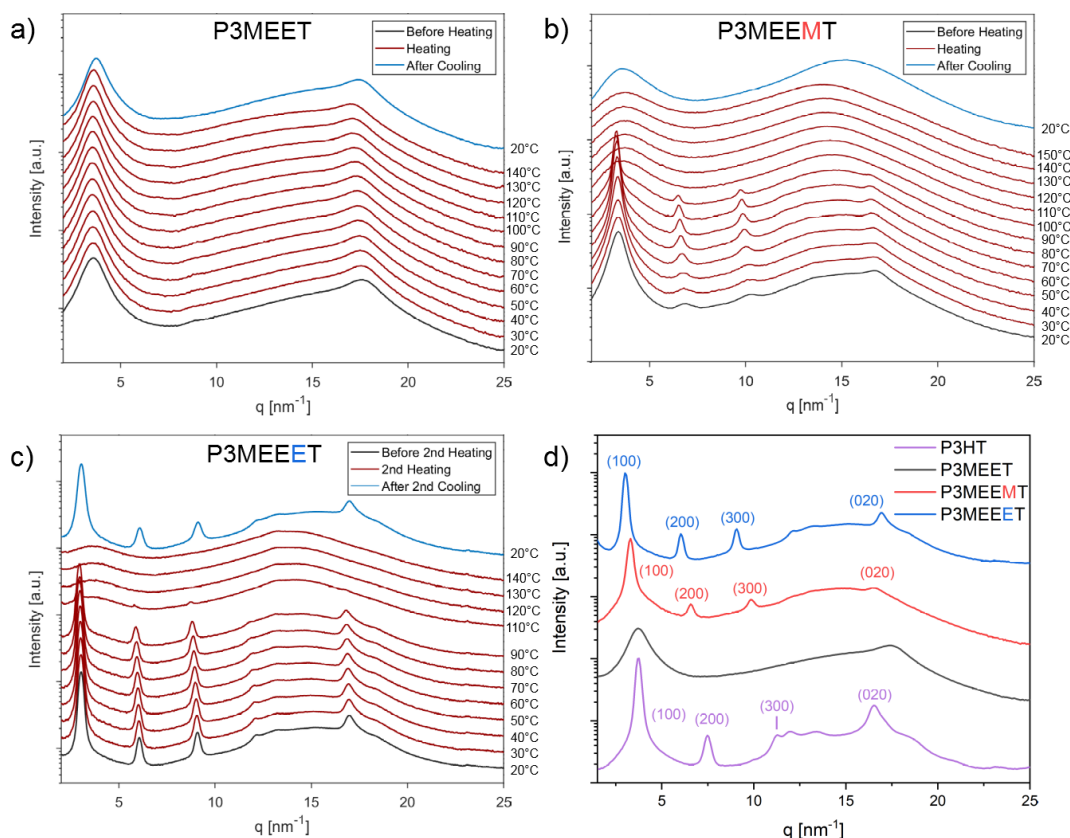
Figure 5.3.: a-c) Powder WAXS patterns measured during step-wise heating of a) P3MEET, b) P3MEEMT and P3MEEET. d) Powder WAXS patterns of P3MEET, P3MEEMT, P3MEEET and P3HT in most ordered state observed. Scattering patterns of P3MEEET and P3HT were measured at 20 °C after crystallization from the melt. P3MEET scattering pattern was measured at 20 °C after annealing at 140 °C. For P3MEEMT the scattering pattern measured at 70 °C, showing the most ordered state observed, is shown. Curves are shifted vertically for better visibility. All visible (h00) and (020) peaks are indexed.

the heating, which is in line with the lack of crystallization and melting peaks in the DSC measurements. In contrast, the temperature dependent WAXS measurements of P3MEEMT clearly show a continuous growing and narrowing of reflection peaks upon heating up to a temperature of around 70 °C, indicating that the sample undergoes cold crystallization resulting in increased ordering. At 100 °C all peaks in the scattering pattern of P3MEEMT have disappeared indicating that the sample has completely molten somewhere between 90 °C and 100 °C, which agrees well with the melting point of $T_m = 99$ °C determined from the DSC measurements. Interestingly, P3MEEMT does not recrystallize upon cooling after having been heated to 150 °C. Since the polymer clearly is able to crystallize as seen from the observed cold crystallization, the absence of

crystallization upon cooling from the melt is most likely a result of thermal degradation of the polymer.[2]

In contrast to P3MEEMT, P3MEEET crystallizes without any significant signs of thermal degradation after cooling from the melt as evidenced by the similar scattering patterns before and after the shown heating run (cf. fig. 5.3c). While the intensities of the scattering peaks of P3MEEET are already significantly reduced at $110\,°C$, they are still clearly visible. Thus, the measurement at $120\,°C$ is the first measurement where the sample is completely molten, which agrees reasonably well with the melting point determined from DSC measurements. Note, that as the sample had been crystallized through slow cooling from the melt prior to the shown heating run, no cold crystallization is observed.

Figure 5.3d) shows a comparison of the most ordered scattering patterns recorded of the polythiophenes with EG side chains and P3HT as reference. While for P3MEET, P3MEEET and P3HT scattering patterns measured at $20\,°C$ are shown, the shown scattering pattern of P3MEEMT was measured at $70\,°C$ representing the most ordered state of P3MEEMT observed. The crystallinity values χ_c of the polymers were estimated from the powder WAXS patterns by comparing the scattering intensities inbetween the (100) and (200) peaks (attributed to the amorphous fraction of the samples) in the semicrystalline and in the fully amorphous (i.e. melt) state as described by Balko et al. [139]. The crystalinity of the P3HT sample was determined to be $81\,\%$ which is similar to values obtained in previous studies [139].

The scattering patterns of both P3MEEMT and P3MEEET show a series of regularly spaced reflections below $10\,nm^{-1}$ and an additional single reflection between $15\,nm^{-1}$ and $18\,nm^{-1}$. By comparison with the scattering pattern of P3HT the equidistant peaks can easily be identified as a series of (h00) reflections, while the single peak can be identified as (020) reflection. In contrast, P3MEET only shows a significantly broader peak at a position where one would expect the (100) reflection likely corresponding to an amorphous structure. The spacings in the side chain direction d_{100} and the π-π-stacking distances d_{020} determined from the (h00) and (020) reflections are given in table 5.1. While d_{100} increase from P3MEEMT to P3MEEET, which is to be expected due to the overall longer side chain, the length of the alkyl spacer apparently does not significantly influence the π-π-stacking distance. For P3MEEMT and P3MEEET the overall number of visible reflections do not suffice to independently determine the unit cell of these polymers. Nonetheless, based on the additional (unindexed) reflections

---

[2]The apparent contradiction between the thermal stability observed during WAXS measurements and the thermal stability determined for P3MEEMT by TGA ($T_{5\%} \approx 300\,°C$) is likely a result of the extended amount of time the sample is kept at elevated temperatures during the WAXS measurements. The time per step of the step-wise heating and cooling program employed during the WAXS measurements is $\approx 22\,min$ ($2\,min$ equilibration time, $10\,min$ WAXS measurement, $10\,min$ SAXS measurement). Thus, the samples are kept at elevated temperatures for multiple hours during the WAXS measurements, which is significantly longer than modeled by the TGA measurements. Therefore, the degradation temperatures determined from TGA measurements recorded employing a continuous heating rate of $10\,K/min$ can result in a significant overestimation of the thermal stability for use-cases where the polymer is kept at elevated temperatures for longer times. A similar observation was also made for the PDPPs investigated in chapter 6.

visible in the scattering pattern of P3MEEET in the range of $10\,\mathrm{nm^{-1}}$ to $20\,\mathrm{nm^{-1}}$ that resemble the reflections found in P3HT in the same range, it can be speculated that the unit cell of P3MEEET is likely quiet similar to the unit cell of P3HT. As the intensity of these additional reflections is quite low in P3MEEET, the absence of similar reflections in P3MEEMT is likely a result of the significantly lower crystallinity and not necessarily an indication of a different or reduced ordering in P3MEEMT.
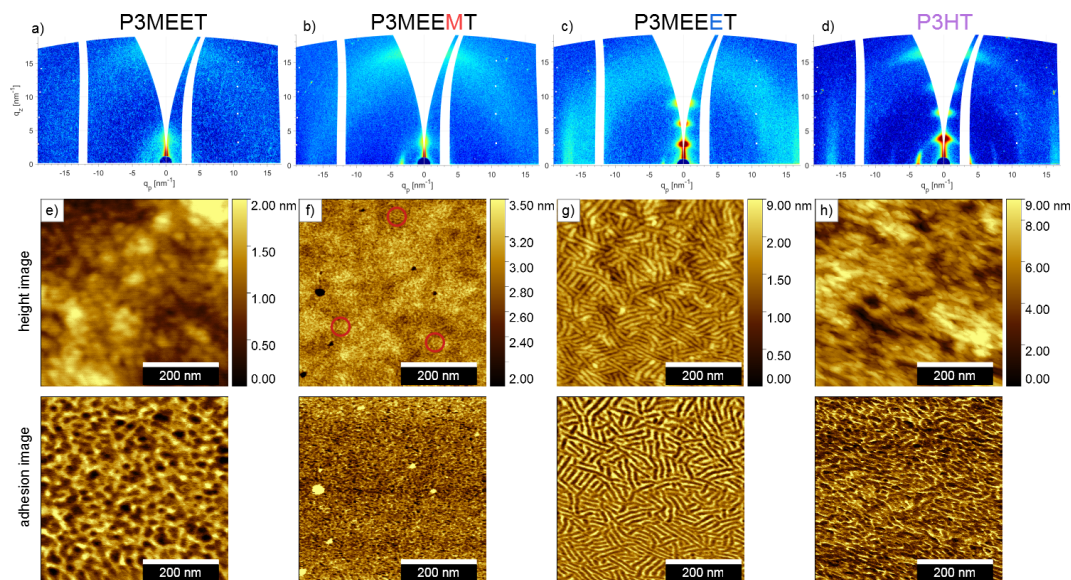

Figure 5.4.: Crystal orientation and surface morphology in thin films of polythiophenes with differently linked EG side chains and P3HT. a-d) GIWAXS patterns of a) P3MEET, b) P3MEEMT, c) P3MEEET and d) P3HT measured at an angle of incidence of 0.2°. e-h) AFM height(upper) and adhesion (lower) images of the same thin films. Red circles in f) highlight a few better visible lamellae. The P3MEET film was measured as cast while all other films were measured after annealing in a vacuum oven.

The performance of devices such as OFET are not only influenced by the crystal structure and the crystallinity of the active material but also by the orientation of these crystals within the active layer. To investigate the influence of the side chain linkage on the preferred crystal orientation in thin films, films of approximately $20\,\mathrm{nm}$ - $30\,\mathrm{nm}$ thickness were spin coated onto silicon substrates and investigated through GIWAXS and AFM measurements.[3] The P3MEEET and P3HT samples were slowly cooled after having been annealed for $5\,\mathrm{min}$ at $141\,°\mathrm{C}$ and $284\,°\mathrm{C}$ respectively (temperatures as indicated by oven), which for both polymers was nominally above the melting point

---

[3]As mentioned in section 3.5, the thin film samples presented in this section were thermally treated in a vacuum oven and not in the microfocus x-ray setup, since the sample stage used to heat thin film samples in the microfocus setup was not yet available. As pointed out in section 3.5 the thermal treatment of thin film samples in the vacuum oven suffers from a less controlled cooling rate which can roughly be estimated to be around $\approx 1\,\mathrm{K/min}$ and a significant temperature dependent offset of the actual sample temperature to the measured temperature.

(cf. table 5.1). The thin film of P3MEEMT was annealed at 85 °C (temperature as indicated by oven) for 5 min, which is nominally below its melting point to minimize thermal degradation. Since P3MEET was classified to be amorphous as discussed above, the P3MEET film was not thermally treated and measured as cast instead. The results of the GIWAXS measurements on these thin films are shown in figure 5.4 together with AFM images of the same films. Comparing the intensities of the (h00) reflections found on the meridian and the horizon of the GIWAXS measurements of both P3MEEMT and P3MEEET (cf. fig. 5.4b,c) reveals a strong preference for the edge-on crystal orientation for both polymers. Clearly, the different linkage of the EG side chains does not have a significant effect on the preferred crystal orientation in thin films of these polymers on silicon substrates. Judging by the amount and position of visible reflections, the GIWAXS pattern of P3MEEET looks rather similar to the scattering pattern of P3HT further attesting to the similarity of the crystal structure of these two polymers. In contrast in the P3MEEMT thin film only the (100) and the (020) reflections are visible. Overall, similar to what was observed in the powder WAXS measurements, a general trend of decreasing order with decreasing length of alkyl spacer is observed.

Another interesting observation can be made in the context of the results presented in section 4: despite having multiple alternating dipoles the EG side chains do not seem to have any significant effect on the preferred crystal orientation. This demonstrates, that it is not just the aspect of whether or not the side chain is polar or not that influences the preferred crystal orientation but indeed a certain dipole moment located at the end-group of the side chain seems to be required. Also note that, while the presence of face-on oriented crystals in a thin film of P3HT on a silicon substrate as evidenced by the (100) peaks located on the horizon (cf. fig. 5.4d) might seem contradicting to the results and arguments presented in chapter 4, the face-on crystals are easily explained as remnants of the spin coating process and are an indication that the P3HT film did not melt completely during the thermal treatment in the vacuum oven. Similar observations of face-on oriented crystals appearing in thin films of P3HT and other semiconducting polymers spin coated onto silicon substrates and annealed below the melting temperature have also been reported in literature [190, 191].

The surface morphologies of the same thin film samples as used for GIWAXS measurements were investigated using AFM operated in peak force tapping mode. The resulting height and adhesion images are shown in the upper and lower row of figures 5.4e-h) respectively. The P3MEEET film shows a clear lamellar morphology featuring numerous stacks of multiple elongated lamellae running in parallel, which is consistent with the strong edge-on orientation of the crystals observed in this film. The P3HT film also shows lamellar morphology albeit the lamellae are shorter and not as well defined as in P3MEEET, which is most likely due to the P3HT film being annealed instead of crystallized from the melt. In contrast, in the P3MEEMT film only a few significantly shorter and narrower lamellae are visible which can be attributed to the annealing and the lower degree of order observed for this polymer in WAXS and GI-WAXS measurements. In the P3MEET film no clear structures can be discerned as to be expected from an amorphous film. Summarizing the results obtained from the

structure investigation, replacing the alkyl side chain of P3HT with an EG side chain results in a general reduction of crystallinity despite seemingly having no significant effect on the unit cell. Furthermore, the crystallinity shows a strong dependence on the linkage of the EG side chain as it decreases significantly with decreasing length of the alkyl spacer culminating in an amorphous polymer when no spacer is present. In contrast, neither the EG side chain nor the linkage of said side chain seem to have a significant effect on the crystal orientation in thin films on silicon substrates.

5.3. Electrochemical Properties and Device Performance
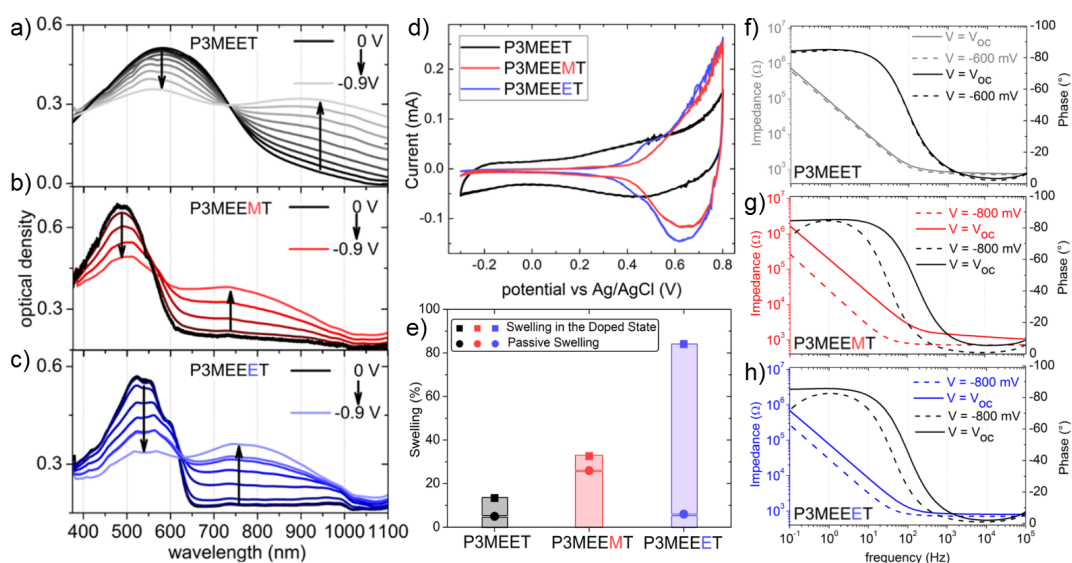
Figure 5.5.: Influence of linkage of DEG side chains on electrochemical and swelling properties of polythiophenes. a-c) Spectroelectrochemistry (SEC) measurements of a) P3MEET, b) P3MEEMT and c) P3MEEET films on ITO. d) Cyclic voltametry (CV) measurements of the polymer films. Both SEC and CV measurements were performed in 0.1 M aqueous NaCl solution using an Ag/AgCl reference and a Pt counter electrode. CV curves were measured at a scan rate of $50\,\mathrm{mV\,s^{-1}}$. e) Swelling of polymer films in 0.1 M aqueous NaCl solution with and without application of a doping potential measured using a electrochemical quartz crystal microbalance with dissipation monitoring. f-h) Electrochemical impedance spectra of f) P3MEET, g) P3MEEMT and h) P3MEEET measured using Au electrodes with a DC voltage of 0.6 V (P3MEET) or 0.8 V (P3MEEMT and P3MEEET) vs Ag/AgCl. Adapted with permission from [189]. Copyright 2020 American Chemical Society.

To allow better understanding of potentially observed differences in the performance of the polythiophenes with differently linked EG side chains in OFET and OECT devices a variety of different electronic properties and the swelling behavior of the

polymers were investigated. The oxidation at doping potential in aqueous medium was investigated through spectroelectrochemistry (SEC) and cyclic voltametry (CV) measurements using a 0.1 M NaCl aqueous electrolyte. The thin film samples for these measurements were prepared on ITO-coated glass substrates. The measurements were performed using a Pt mesh as counter electrode and an Ag/AgCl reference electrode. The UV-Vis absorption spectra of the films at different applied doping potentials (0 V to −0.9 V in −0.1 V steps) are plotted in figures 5.5a-c). Each doping potential was applied for 10 s before the absorption spectra was recorded. As seen from these measurements, the general trend upon application of increasing doping potentials is similar in all three polymers: Upon exceeding a polymer specific threshold potential, a continuous decrease of the π-π^* associated absorption peak is observed while at the same time a red-shifted polaron absorption peak appears and grows with further increasing doping potential. In P3MEEMT and P3MEEET the onset of oxidation occurs at similar doping potentials (≈ -0.6 V and ≈ -0.5 V respectively). In contrast, P3MEET exhibits a significantly lower onset of oxidation of only ≈ -0.2 V. Determining the onsets of oxidation from the CV measurements shown in figure 5.5d) gives comparable values to the results from the SEC measurements. While P3MEET shows the lowest onset of only 0.1 V, P3MEEMT and P3MEEET show higher onsets of oxidation of 0.5 V and 0.4 V respectively. The lower onset of oxidation in P3MEET compared to P3MEEMT and P3MEEET can be explained by a lower oxidation potential caused by the electron withdrawing effect of the oxygen atom of the EG side chain being directly attached to the conjugated backbone.

The swelling behavior of the polymers was investigated using an electrochemical quartz crystal microbalance with dissipation monitoring (EQCM-D). The mass of the polymer films in the dry state and when exposed to 0.1 M NaCl aqueous solution without an applied doping potential were determined from observed shifts of the 7th overtone of the resonance frequency δf of the QCM sensor using the Sauerbrey equation: $\Delta m = -C\Delta f/n$, where C is the mass sensitivity constant and n is the order of the used overtone. For the 5 MHz quartz crystal of the QCM sensor C is 17.7 ng cm^{-2} Hz^{-1} [192]. The swelling of the polymer films exposed to the NaCl solution upon application of a doping potential lead to large changes in dissipation and thus a Kelvin-Voigt model was used instead of the Sauerbrey equation to fit the energy dissipation and observed shifts in resonance frequencies of the 3rd, 5th and 7th overtones for these measurements [193, 194]. The doping potentials were applied to the films using a three-electrode setup with a Ag/AgCl reference electrode, a Pt counter electrode and the EQCM-D sensor acting as the working electrode. The results of the swelling experiments are summarized in figure 5.5e). The passive swelling of the films exposed to the NaCl solution resulted in a relative mass uptake of (5 ± 2) % for P3MEET, (26 ± 8) % for P3MEEMT and (6 ± 3) % for P3MEEET. Thus, while the passive swelling in P3MEET and P3MEEET are comparable, the passive swelling of P3MEEMT is significantly more pronounced. Interestingly, upon application of a doping potential this trend changes fundamentally as the P3MEET and P3MEEMT films both take up another approximately 1.0 µg cm^{-2} while the mass of the P3MEEET film increases by 12 µg cm^{-2}. Therefore, P3MEEET shows a 12 times higher mass uptake than the other two polymers. This high mass

uptake in P3MEEET is amongst the highest values reported for mixed conduction polymers and also higher than reported for the benchmark accumulation mode polymer p(g2T-TT) [185, 186]. Neither the differences in passive swelling nor the differences in swelling under applied doping potential correlate with spacer length, crystallinity or observed film morphology. Thus, while the investigated polymers differ significantly in their swelling behavior, the mechanisms responsible for these differences are unclear.

Another important material parameter for materials intended for use in OECT devices is the volumetric capacitance C^* as the transconductance g_m of an OECT device scales linearly with C^* (cf. eq. 2.12 in section 2.3.3). Therefore, the volumetric capacitance of the three polymers was determined using electrochemical impedance spectroscopy (EIS) measurements. The measurements were performed in an $0.1\,\mathrm{M}$ NaCl aqueous solution. During the measurements, in addition to the AC potential with an amplitude of $10\,\mathrm{mV}$, an additional polymer specific DC offset potential was applied in order to measure the polymers in a state of maximum achievable doping. Figure 5.5f-h) shows the result of the EIS measurements recorded at open-circuit potential before doping ($V = V_{OC}$) and with an applied doping potential ($V = 0.6\,\mathrm{V}$ for P3MEET and $V = 0.8\,\mathrm{V}$ for P3MEEMT and P3MEEET). To determine the capacitance of the polymers the impedance curves were fitted using a simplified Randles circuit ($R_{electrolyte}(R_{polymer}||C_{polymer})$) [195, 196]. The volumetric capacitance C^* was then determined by normalizing the capacitance of the polymer films by the volume of the dry films, as is a common approach [92, 197]. The determined volumetric capacitance shows a strong depends on the linkage of the EG side chain. While P3MEET without a spacer has a volumetric capacitance of $(80 \pm 9)\,\mathrm{F\,cm^{-3}}$, the volumetric capacitance doubles to $(160 \pm 12)\,\mathrm{F\,cm^{-3}}$ in P3MEEMT when a methyl spacer is introduced and increases even further to $(242 \pm 17)\,\mathrm{F\,cm^{-3}}$ in P3MEEET which has an ethyl spacer. The volumetric capacitance of P3MEEET is therefore amongst the highest reported values for p-type mixed conductor polymers [178, 92]. The differences in volumetric capacitance between the three polymers are likely related to the differences in order and crystallinity, as Sivaraman et al. observed a similar dependence of the capacitance of P3HT films on the crystallinity by studying P3HTs with varying regioregularities [198]. Furthermore, Proctor et al. proposed a simple phenomenological model that describes the volumetric capacitance in terms of anion/hole pairs that form along the backbone upon doping [199]. According to their model, the film contains a certain number of these sites (anion/hole pairs). Cations injected from the electrolyte diffuse towards these sites and replace holes which then can be extracted from the film through the metal contacts . Within this model, the observed increase of volumetric capacitance with increasing length of the alkyl spacer and increasing crystallinity could be explained by a better accessibility of theses specific cites to the injected anions, thus increasing the number of accessible cites that can form anion/hole pairs.

The polymers were tested as active layer in OFET and OECT devices. OFET devices in bottom gate/bottom contact geometry were prepared by spin coating the polymers from a chloroform solution onto special substrates as described in section 3.5. The measured output and transfer curves of P3MEEMT and P3MEEET based OFETs are shown in figure 5.6 a-d). For the P3MEET based OFETs no transistor behavior
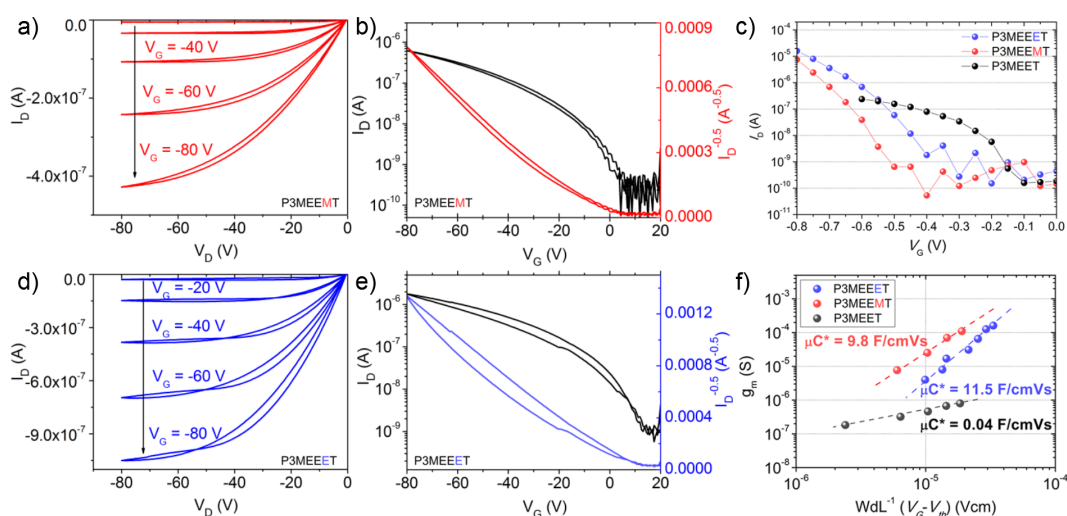
Figure 5.6.: Electronic properties of OFET and OECT devices based on polythiophenes with differently linked DEG side chains. a,d) Output and b,e) transfer curves of OFET devices based on a,b) P3MEEMT and d,e) P3MEEET. c) Transfer curves of OECT devices based on P3MEET, P3MEEMT and P3MEEET. d) Transconductance g_m of OECT devices plotted against channel geometry and operation parameters. Linear fits used to determine the μC^* product for each material are given as dashed lines. Adapted with permission from [189]. Copyright 2020 American Chemical Society.

was observed. The hole mobilities determined from the transfer curves of the OFET devices μ_{OFET} reveal a difference between P3MEEMT and P3MEEET of more than one order of magnitude ($0.0003\,\mathrm{cm^2\,V^{-1}\,s^{-1}}$ and $0.005\,\mathrm{cm^2\,V^{-1}\,s^{-1}}$ respectively). While the determined hole mobility of P3MEEET is an order of magnitude smaller than the hole mobility reported for P3HT based OFETs prepared under similar conditions (spin coated from chloroform) [200, 201, 202], it is still one of the highest mobilities in OFET devices reported for polythiophenes with polar side chains [203, 204]. The hole mobility in polymers can be influenced by many different factors. Some of the more important factors are the π-π stacking distance, the disribution of crystal orientataions and the crystallinity [19, 205, 206]. Although further factors cannot be excluded, the lack of significant differences between P3MEEMT and P3MEEET regarding the π-π stacking distance or the distribution of crystal orientations (cf. section 5.2) suggests, that the differences in hole mobilities can be attributed mainly to the observed differences in crystallinity.

The OECT devices were prepared by spin coating the polymers from chloroform solution onto the OECT substrates prepared as described in section 3.5 using photolithography and a parylene-C lift-off method. All resulting polymer films show comparable thicknesses in the range of $90\,\mathrm{nm}$ to $100\,\mathrm{nm}$. Figure 5.6c) shows the transfer curves of the OECTs based on P3MEET, P3MEEMT and P3MEEET measured in $0.1\,\mathrm{M}$ NaCl aqueous solution using a Ag/AgCl pellet as gate electrode.

Interestingly P3MEET, which did not show any transistor characteristics in OFET devices, clearly is a functional active material for OECT devices. In addition, the threshold voltage of P3MEET is significantly lower than for the other two polymers, which is well in line with the low onset of oxidation of P3MEET observed in SEC and CV measurements and again is likely caused by the electron withdrawing effect of the oxygen being directly connected to the conjugated backbone.

Figure 5.6f) shows the transconductance g_m of the different OECT devices as a function of channel geometry and operation parameters. As discussed in section 2.3.3, according to equation 2.12, the slope of this curve is defined by the $\mu_{OECT}C^*$ product. Thus, the $\mu_{OECT}C^*$ product for the different polymers were determined by fitting these curves linearly. The highest $\mu_{OECT}C^*$ product was observed in P3MEEET ($11.5\,\mathrm{F\,cm^{-1}\,V^{-1}\,s^{-1}}$) followed by a comparable but slightly lower value found in P3MEEMT ($9.8\,\mathrm{F\,cm^{-1}\,V^{-1}\,s^{-1}}$). In comparison, the $\mu_{OECT}C^*$ product in P3MEET($0.04\,\mathrm{F\,cm^{-1}\,V^{-1}\,s^{-1}}$) is more than two orders of magnitude lower than those of P3MEEMT and P3MEEET. Thus, P3MEEET with its ethyl spacer is the most promising of the three polymers for bioelectronic applications. As the OECT characteristics are known to depend on the chosen electrolyte [185], using an electolyte containing divalent anions or anions with different polarities might improve the performance of P3MEEET based OECT devices even further. Also note, that all three polymers could be tested in OECT devices without any additional cross-linker as the polymers only swell but do not dissolve in aqueous environment.

Based on the volumetric capacitances C^* of the polymers determined from the EIS measurements it is possible to estimate the hole mobilities μ_{OECT} of the different polymers from their $\mu_{OECT}C^*$ products. Here, μ_{OECT} describes the hole mobility in the swollen and oxidized state under OECT operation. While P3MEEMT and P3MEEET show similar hole mobilities in OECT devices of $60 \times 10^{-3}\,\mathrm{cm^2\,V^{-1}\,s^{-1}}$ and $50 \times 10^{-3}\,\mathrm{cm^2\,V^{-1}\,s^{-1}}$ respectively, P3MEET exhibits a significantly lower hole mobility of only $0.52 \times 10^{-3}\,\mathrm{cm^2\,V^{-1}\,s^{-1}}$. Interestingly, the hole mobility of P3MEEMT in the swollen state (μ_{OECT}) is slightly higher than that of P3MEEET despite the fact that P3MEEET exhibits a one order of magnitude higher hole mobility than P3MEEMT in the dry state (μ_{OFET}). Generally, high degrees of order and higher crystallinities are considered to be a requirement for high hole mobilities in polythhiophenes. Therefore, the smaller increase in hole mobility in P3MEEET compared to P3MEEMT is possibly a result of the excessive swelling observed in P3MEEET which likely disturbs the arrangement of the polymer chains and thus results in decreased order in the polymer film. Similar observations of reduced hole mobility with increased swelling have also been reported by Savva et al. for p(g2T-TT) [186]. In contrast, a smaller degree of swelling combined with doping via the uptake of ions clearly has a beneficial effect on the hole mobility as observed for P3MEET, which did not show any transistor behavior in the dry state but is a functional OECT material in the swollen state.

The results of the characterization of OFET and OECT devices based on the three polythiophenes with differently linked EG side chains are summarized in table 5.2.

Table 5.2.: Electronic Properties of OFET and OECT Devices Based on Polythiophenes with DEG Side Chains

Polymer	C^* [a] [F/cm^3]	μ_{OFET} [b] [cm^2/(V s)]	μ_{OECT} [c] [cm^2/(V s)]	g_m/d [d] [S/cm]	$\mu_{OECT} \cdot C^*$ [d] [F/(cm V s)]
P3MEET	80 ± 9	-	$0.52 \cdot 10^{-3}$	0.02	0.04 ± 0.01
P3MEEMT	160 ± 12	$0.3 \cdot 10^{-3}$	$60 \cdot 10^{-3}$	12.3	9.8 ± 1.1
P3MEEET	242 ± 17	$5 \cdot 10^{-3}$	$50 \cdot 10^{-3}$	20.4	11.5 ± 1.4

[a] Volumetric Capacitance determined by EIS on Au electrodes with a DC voltage vs Ag/AgCl. [b] Hole mobility as measured from OFET devices in bottom-gate and bottom-contact geometry. [c] Hole mobility as determined from $\mu_{OECT} \cdot C^*$ of OECT devices by dividing by C^*. [d] Transconductance determined from measurements on OECT devices in hydrated state using an Ag/AgCl pellet as the gate electrode and normalized by film thickness.

5.4. Conclusion

In this chapter a series of polythiophenes with ethylene glycol (EG) side chains was investigated to elucidate the effect of the linkage of EG side chain to the backbone on various material properties and on the performance in OFET and OECT devices. In the three investigated polythiohpenes the EG side chain was either directly attached to the backbone (P3MEET) or with a methyl or ethyl spacer in between the EG side chain and the backbone (P3MEEMT and P3MEEET respectively). It was demonstrated, that the thermal stability of the polymers decreases greatly with decreasing spacer length. Both the melting temperature and the crystallinity follow the same trend, culminating in the amorphous polymer P3MEET where the EG side chain is directly attached to the backbone. Based on a qualitative comparison of the WAXS patterns of P3MEEMT, P3MEEET and P3HT no significant influence of the spacer length on the crystal structure could be observed. Similarly to P3HT, the polythiophenes with EG side chains show a dominant edge-on crystal orientation in thin films on silicon with no discernible effect of the spacer length on the preferred crystal orientation.

The observed increase in crystalinity with increasing spacer length is also reflected in the OFET measurements in which the amorphous P3MEET shows no OFET behavior at all, while P3MEEET shows one of the highest hole mobilities reported for a polar polythiophene homopolymer.

Similarly, the volumetric capacitance $C*$, the swelling under doping potential as well as the performance in OECT devices expressed through the transconductance g_m and the $\mu_{OECT} \cdot C^*$ product also all increase with increasing spacer length. Interestingly, the hole mobility determined from OECT devices μ_{OECT} does not increase monotonously with increasing spacer length as P3MEEMT (methyl spacer) exhibits a slightly higher hole mobility than P3MEEET (ethyl spacer). The lower μ_{OECT} in P3MEEET is likely caused by a certain disturbance of the crystal structure as a result of excessive swelling,

as P3MEEET showed a 12 times higher water uptake under applied doping potential than P3MEET and P3MEEMT.

Overall, the seemingly trivial design aspect of the linkage of the EG side chain to the thiophene backbone clearly has a strong influence on many different material properties and is especially important for the interplay of swelling and charge transport in OECT devices.

6. Intermolecular Ordering in Polydiketopyrrolopyrroles

The modular chemical structure of polydiketopyrrolopyrroles (PDPPs) allows to easily introduce a large variety of chemical modifications. Through chemical modification of the backbone it is for example possible to control whether the resulting PDPPs are p-type, n-type, or ambipolar semiconductors [207, 208, 209, 210, 211]. By modifying the type or number of side chains the solubility and swelling behaviour in different solvents can be tuned. In this regard, attaching ethylene glycol (EG) side chains results in PDPPs that swell in aqueous media and are mixed ion-electron conductors, making these PDPPs suitable for applications in bioelectronic devices, such as organic electrochemical transistors (OECT) [212].

Despite the large number of different PDPPs that have been synthesized [37], the molecular ordering has only been investigated for a few PDPPs and especially the extent to which the molecular ordering can be influenced by different chemical modifications has not been investigated in detail.
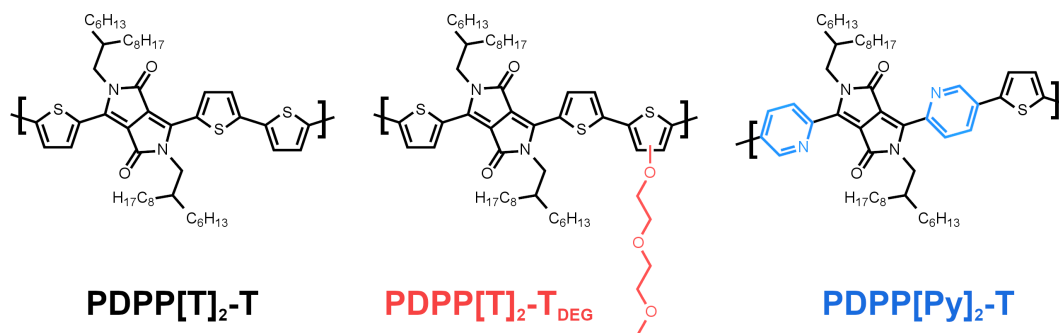
Figure 6.1.: Chemical structure of the three investigated PDPPs. The differences in the chemical structure of PDPP[T]$_2$-{DEG} and PDPP[Py]$_2$ with regard to PDPP[T]$_2$ are highlighted in color. Reprinted with permission from [213]. Copyright 2024 American Chemical Society.

Here, the influence of chemical modifications on the molecular ordering of PDPPs is investigated using a series of three representative PDPPs: PDPP[T]$_2$-T, PDPP[T]$_2$-T$_{DEG}$ and PDPP[Py]$_2$-T. The chemical structure of the three PDPPs is shown in figure 6.1. The choice of the introduced chemical modifications is aimed to represent typical or common modifications of PDPPs while also keeping the overall extent of modifications to a minimum, such that a certain correlation between the ordering behaviors of

the different PDPPs can still be expected. Within the investigated series of PDPPs the commercially available PDPP[T]$_2$-T serves as a reference sample. PDPP[T]$_2$-T has two thiophene flanking units and a thiophene comonomer. PDPP[T]$_2$-T$_{DEG}$ and PDPP[Py]$_2$-T are both derived from PDPP[T]$_2$-T by introducing one chemical modification each. In PDPP[T]$_2$-T$_{DEG}$ an additional polar diethyleneglycol (DEG) side chain was attached to the thiophene comonomer and therefore it serves as a representative for common side chain modifications. In contrast, PDPP[Py]$_2$-T serves as a representative of common backbone modifications and was derived from PDPP[T]$_2$-T by replacing the thiophene flanking units with pyridine flanking units. This modification of the backbone changes the polymer from an electron-rich (donor) to an electron deficient (acceptor) semiconductor [209]. [1] An overview of the determined molecular weight and the dispersity Đ of the three investigated PDPPs is given in table 6.1 together with a summary of selected parameters discussed in the following sections. The molecular ordering in the three investigated PDPPs is determined using WAXS and GIWAXS measurements, proving that the introduced chemical modifications indeed significantly impact the ordering in these materials. The ordering in both PDPP[T]$_2$-T and PDPP[T]$_2$-T$_{DEG}$ can be classified as sanidic liquid crystalline, with PDPP[T]$_2$-T$_{DEG}$ adopting a mesophase of higher order. PDPP[Py]$_2$-T shows the highest degree of order of the three and is crystalline with a triclinic unit cell.

The results presented in this section have partially been published in reference [213].

Table 6.1.: M_n and PDI of each sample measured by GPC. Decomposition temperature determined by stepwise isothermal TGA. Melting temperature measured by DSC. *Due to sample degradation issues, T_m and ΔH_m of PDPP[Py]$_2$ were determined from the first heating run.

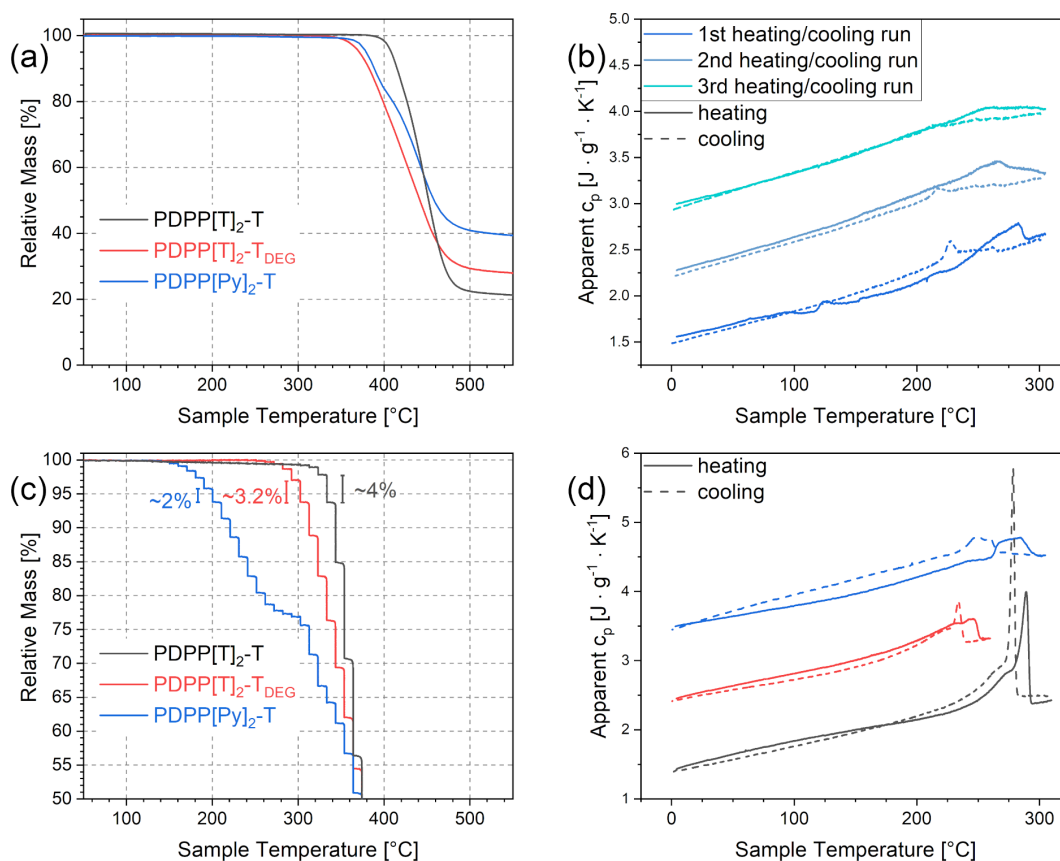| Polymer	M_n [a] [kDa]	Đ [a]	$T_{5\%}^{dynamic}$ [b] [°C]	$T_{5\%}^{isotherm}$ [c] [°C]	T_m [d] [°C]	ΔH_m [d] [J/g]	d_{100} [e] [Å]	d_{010} [e] [Å]
PDPP[T]$_2$-T	45.4	2.94	408.4	330	289.1	25.0	19.39	3.91
PDPP[T]$_2$-T$_{DEG}$	17.6	1.94	371.3	300	244.3	11.5	18.98	3.70
PDPP[Py]$_2$-T	43.5	1.8	379.1	200	284.7	6.9	18.81	3.88

Figure 6.2.: (a)Dynamic and (c) Isothermal TGA and (d) DSC measurements of the investigated PDPPs. PDPP[T]$_2$-T (black), PDPP[T]$_2$-T$_{DEG}$ (red) and PDPP[Py]$_2$-T (blue).(b) Consecutive DSC measurements of PDPP[Py]$_2$-T showing signs of degradation. The scalebars in (c) indicate the relative mass loss during the annealing step during which the relative sample mass fell below 95 wt%. Reprinted with permission from [213]. Copyright 2024 American Chemical Society.

6.1. Thermal Behavior and Optimal Thermal Treatment

6.1.1. Thermal Stability and Phase Transitions

The structure investigation using scattering techniques benefits from well ordered samples with high crystallinities. The ordering in polymer samples can be significantly improved by submitting the sample to a suitable thermal program used during sample preparation. To determine a suitable thermal program for the crystallization of the

---

[1]PDPP[T]$_2$-T was purchased from Ossila, Sheffield, England. Both PDPP[T]$_2$-T$_{DEG}$ and PDPP[Py]$_2$-T were synthesized by the group of professor Mukundan Thelakkat from the University of Bayreuth (Gerd Krauss: PDPP[T]$_2$-T$_{DEG}$; Ferdinand Seibold: PDPP[Py]$_2$-T) following a previously published synthesis [209, 212]. All thermogravimetric anylsis (TGA) and gel permeation chromatography (GPC) measurements presented here were also performed by the group of professor Thelakkat. All DSC and powder WAXS measurements, as well as all GIWAXS and AFM measurements of thin films were performed by the author of this thesis.

PDPP samples, their thermal stability and phase behavior were studied through TGA and DSC measurements. As shown in figure 6.2a all samples exhibit relatively high thermal stability in common dynamic TGA measurements, where the temperature at which a total mass loss of $5\,\mathrm{wt\%}$ is reached lies above $370\,^\circ\mathrm{C}$ for all samples. To verify the reproducibility of the DSC measurements, each sample was measured in three consecutive heating and cooling runs with a heating/cooling rate of $10\,\mathrm{K/min}$ and a short isothermal step of $1\,\mathrm{min}$ at the maximum temperature T_{max} (required by the instrument software). Despite the results of the dynamic TGA measurements suggesting high thermal stability for all samples, the PDPP[Py]$_2$-T sample showed signs of thermal degradation in these consecutive DSC measurements (cf. fig. 6.2b) although only being heated to T_{max}=305 $^\circ\mathrm{C}$. Comparing the three consecutive measurements, a systematic reduction in melting and crystallization enthalpies as well as in melting and crystallization temperatures is evident. Measurement of the sample mass before and after the DSC measurement further revealed a mass loss of $6.4\,\%$ indicating a significantly smaller thermal stability of PDPP[Py]$_2$-T than estimated based on the dynamic TGA measurements.

Thus, to further investigate the thermal stability of the samples additional isothermal TGA measurements following a stepwise heating program with steps of $10\,\mathrm{K}$ and an annealing time of $1\,\mathrm{h}$ at each step were performed. These stepwise isothermal measurements reflect the treatment conditions used during sample preparation for WAXS and GIWAXS measurements more accurately compared to dynamic TGA measurements, as the samples typically reside at elevated temperatures for longer times during sample preparation than modeled by a dynamic TGA measurement. However, because of the extended duration of the isothermal segments, the results shown in figure 6.2c should be understood as an upper limit for the actual material deterioration occurring during the experiments described below.

Overall, the decomposition temperatures $T_{5\%}^{isotherm}$ determined from the isothermal TGA measurements are all lower than the values determined from dynamic TGA. While PDPP[T]$_2$-T and PDPP[T]$_2$-T$_{DEG}$ still exhibit reasonable thermal stability and a total mass loss of $5\,\mathrm{wt\%}$ is only reached at $330\,^\circ\mathrm{C}$ and $300\,^\circ\mathrm{C}$ respectively, PDPP[Py]$_2$-T starts to degrade comparably early and already reaches a total mass loss of $5\,\mathrm{wt\%}$ at only $200\,^\circ\mathrm{C}$. The reason for the lower onset of mass loss of PDPP[Py]$_2$-T revealed only in isothermal TGA is not clear. The deterioration of a distinct structural site seems unlikely since PDPP[Py]$_2$-T shows no substantial mass loss before the degradation onset of the other investigated PDPP materials in dynamic TGA measurements.

To investigate the melting and crystallization behavior of the polymers DSC measurements with a heating/cooling rate of $10\,\mathrm{K/min}$ were performed. The resulting measurement curves are shown in figure 6.2d. For PDPP[T]$_2$-T and PDPP[T]$_2$-T$_{DEG}$ the first cooling and second heating run are shown. Since the second heating run of PDPP[Py]$_2$-T in consecutive DSC runs showed signs of degradation as discussed above (cf. fig. 6.2b), for PDPP[Py]$_2$-T the first cooling and first heating runs after a preceding annealing program are shown instead. The employed annealing program is the same as also used for the WAXS-measurements of PDPP[Py]$_2$-T and serves to crystallize the sample. The annealing program is shown in figure 6.4.

PDPP[T]$_2$-T and PDPP[Py]$_2$-T exhibit quite similar melting temperatures of 289.1 °C and 284.7 °C respectively. In contrast, the melting temperature of PDPP[T]$_2$-T$_{DEG}$ of 244.3 °C is significantly lower. As discussed in chapter 5, a similar reduction in melting temperature was also observed in the investigated polythiophenes upon replacing the hexyl side chains of P3HT with DEG side chains. Notably, the melting temperature of PDPP[Py]$_2$-T lies significantly above the onset of thermal degradation determined from the isothermal TGA measurements. The results of the DSC and TGA measurements are summarized in table 6.1.

6.1.2. Thermal Treatment Dependent Crystal Orientation in Thin Films

A well ordered sample is the prerequisite for scattering based structure determination. A common approach to prepare highly ordered polymer samples is to slowly cool them from the melt. For the PDPP[T]$_2$-T and PDPP[T]$_2$-T$_{DEG}$ this is a valid approach. However, as the onset of thermal degradation of PDPP[Py]$_2$-T lies significantly below its melting temperature crystallization from the melt is likely not feasible. This was confirmed by an initial series of temperature dependent WAXS measurements during which a PDPP[Py]$_2$-T powder sample was heated and cooled stepwise in 10 K steps and in which the PDPP[Py]$_2$-T sample did not recrystallize upon cooling from the melt. Accordingly, for the WAXS measurement used for structure determination the PDPP[Py]$_2$-T sample was ordered by annealing at 240 °C, 250 °C and 260 °C for 12 min each, reproducing the section of the initial series of temperature dependent WAXS measurements during which PDPP[Py]$_2$-T showed the most well pronounced scattering pattern.

When attempting to optimize the annealing program for thin film samples used for GIWAXS measurements, besides the degree of ordering and the thermal degradation, the degree of crystal orientation is an additional important parameter that has to be considered. The significant effect annealing can have on the crystal orientation has been observed for many different semiconducting polymers [214, 22, 211]. The observed changes upon annealing reach from a simple increase in degree of orientation to a complete change of the predominant orientation(e.g. change from strong face-on to strong edge-on orientation) [190, 215]. It is assumed that the predominant orientation observed in the as-cast samples is a result of the spin-coating process and does not represent a state in thermodynamic equilibrium but results from kinetic trapping of the chain molecules during the quick evaporation of the solvent. [191] The exact relationship between melting temperature and annealing temperature required to achieve a high degree of orientation is yet unclear. While for some polymers it is reported that a complete orientation is only achieved through crystallization during cooling from the melt [191], in other cases annealing the sample at temperatures below the melting temperature suffices [216].

To determine the minimal annealing temperature necessary to achieve the degree of crystal orientation in thin films of PDPP[Py]$_2$-T required for structure analysis, a se-
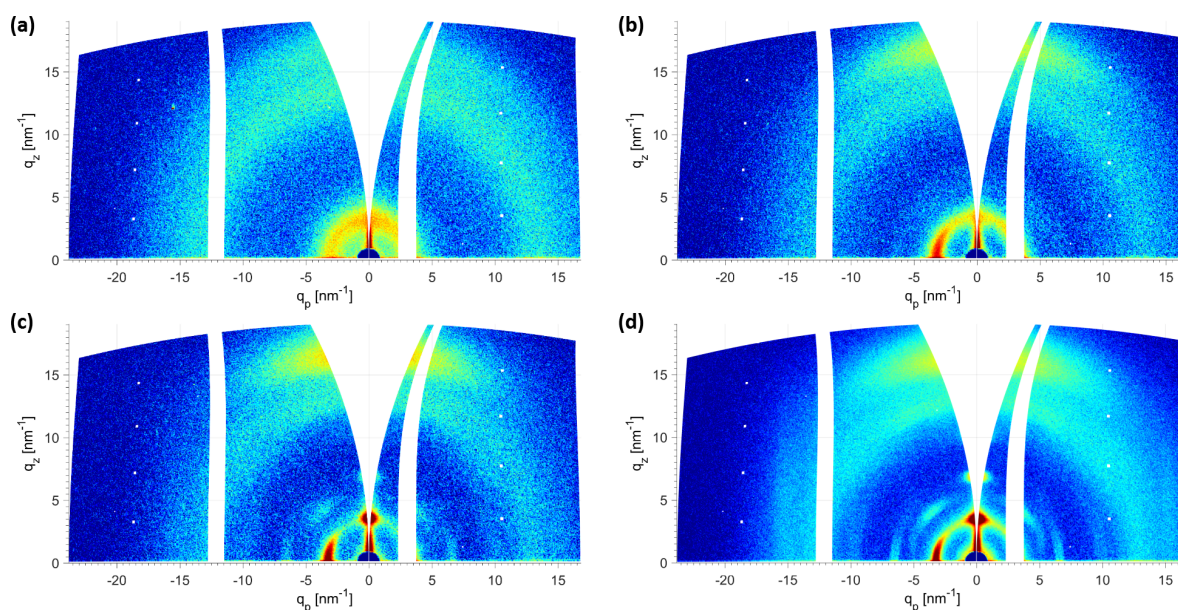
Figure 6.3.: GIWAXS measurements on thin films of PDPP[Py]$_2$-T recorded at room temperature of a) the as-cast film and after annealing at b) 179 °C and c) 239 °C. d)Fresh sample measured after stepwise annealing with a maximum annealing temperature of 269 °C. Panels a-c)Reprinted with permission from [213]. Copyright 2024 American Chemical Society.

ries of GIWAXS measurements was performed employing different annealing temperatures. For these measurements a thin film of PDPP[Py]$_2$-T was annealed for 12 min at ever increasing temperatures in a range of 130 °C to 240 °C and the resulting crystal orientation was measured at room temperature via GIWAXS after each annealing step.

As the observed degree of crystal orientation was still insufficient even after annealing at 239 °C a fresh sample was heated in steps and annealed at 269 °C for 5 min. Figure 6.3 shows some selected GIWAXS patterns of this measurement series measured at room temperature of the as-cast sample and after annealing at different temperatures. The as-cast sample is poorly ordered and poorly oriented as can be seen from the broad and isotropically distributed (100) peak seen at $q \approx 3\,\mathrm{nm}^{-1}$(cf. fig. 6.3a). As seen from the steadily increasing intensity and the number of visible peaks, the overall crystallinity of the sample and the order within the crystals increase steadily with increasing annealing temperature. In contrast, the crystal orientation does not change steadily with the annealing temperature. At lower annealing temperatures primarily the amount of face-on oriented crystals increases and the originally isotropic film becomes predominantly face-on oriented. At higher annealing temperatures the amount of edge-on crystals starts to increase resulting in a bimodal orientation distribution of crystals in the film. As can be seen in figure 6.3d, even annealing a PDPP[Py]$_2$-T film at 269 °C only resulted in a bimodal instead of uniform orientation. Therefore, a final sample was prepared and annealed at 289 °C for 6 min. In order to increase the crystallinity the sample was cooled with $10\,\mathrm{K\,min}^{-1}$ and two isothermal steps, a

first step at $259\,°C$ of 6 min length and a second step at $130\,°C$ of 12 min length. These specific temperatures for the isothermal steps were chosen as in temperature dependent powder WAXS measurements PDPP[Py]$_2$-T showed the highest degree of ordering at $259\,°C$ and the first signs of reorganization at $130\,°C$. This resulted in a well ordered and strongly edge-on oriented film suitable for structure determination. The GIWAXS measurement of this film is therefore shown and discussed in more detail in section 6.2. For comparison, similar measurements were performed for the PDPP[T]$_2$ and PDPP[T]$_2$-T$_{DEG}$ samples. During the annealing at elevated temperatures all samples were monitored using in-situ GIWAXS measurements to determine whether the samples had molten or not. The first complete melting in PDPP[T]$_2$ was observed during the annealing step at $289\,°C$, which is in good agreement with the melting temperature of $T_m =289.1\,°C$ determined from DSC measurements. In contrast PDPP[T]$_2$-T$_{DEG}$ and PDPP[Py]$_2$-T melting behaviour in these measurements showed a slight offset to their melting points ($T_m =244.3\,°C$ and $T_m =284.7\,°C$ respectively) determined from DSC measurements. While for PDPP[T]$_2$-T$_{DEG}$ the first complete melting was already observed during the annealing step at $239\,°C$, for PDPP[Py]$_2$-T a (100) reflection was still visible at $289\,°C$. These minor offsets most likely originate from differences in thermal contact and a small error in the temperature calibration of the GIWAXS sample stage.
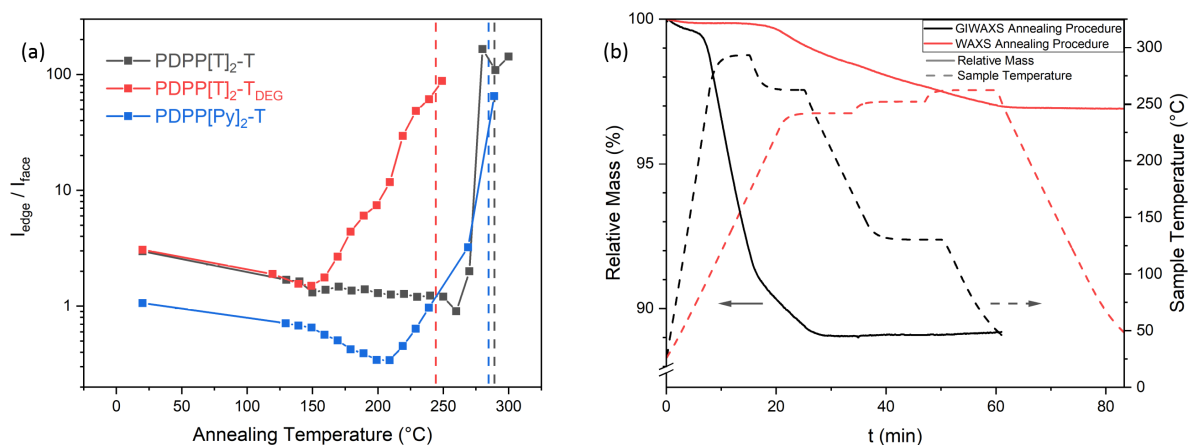

Figure 6.4.: a) Ratio of intensities I_{edge}/I_{face} of the (100) reflection in GIWAXS measurements of thin films as a function of annealing temperature. Dashed vertical lines indicate melting temperatures determined from DSC measurements. b)TGA measurement of PDPP[Py]$_2$-T following the same temperature program as used for annealing in WAXS(red) and GIWAXS(black) measurements. Solid lines show relative sample mass and dashed lines show sample temperature. Panel b) reprinted with permission from [213]. Copyright 2024 American Chemical Society.

A summary of the measurement series employing different annealing temperatures for all investigated PDPPs is given in figure 6.4a which shows a plot of the ratio of the maximum intensity of the edge-on (100) peak over the maximum intensity of the face-on (100) peak as a function of annealing temperature for each of the three investigated

PDPPs. Overall all three PDPPs show similar trends. Annealing at temperatures far below the melting temperature results in predominantly face-on oriented films indicating, that the spin-coating process resulted in chains being preferably oriented face-on for all three PDPPs. In all samples, reorientation from predominant face-on to almost exclusive edge-on orientation occurred only upon annealing the samples fairly close to the melting temperature. In PDPP[T]$_2$-T$_{DEG}$ the change from face-on to edge-on is more gradual than in PDPP[T]$_2$-T and PDPP[Py]$_2$-T, suggesting that the face-on oriented crystals in PDPP[T]$_2$-T$_{DEG}$ are thermally less stable than the face-on crystals in the other two polymers. Overall, cooling from the melt resulted in the most edge-on oriented films. Nonetheless, a significant reorientation from face-on to edge-on already occurs upon annealing the films close to the melting temperature in all three PDPPs. From these results, it is clear, that in order to obtain a well oriented thin film of PDPP[Py]$_2$-T annealing close to the melting temperature and thus a certain amount of sample degradation cannot be avoided. To determine the extent of degradation in the PDPP[Py]$_2$-T samples when subjected to the chosen annealing programs, TGA measurements following the same annealing programs as used for preparation of WAXS and GIWAXS samples were performed. The results of these measurements are shown in figure 6.4b. While the annealing program used for the WAXS sample resulted in a mass loss ($<5\,\%$) only, the annealing program used for the GIWAXS sample led to a more significant mass loss of $>10\,\%$. Consequently, the WAXS measurements of PDPP[Py]$_2$-T are most likely unaffected by thermal degradation. Furthermore, based on the good agreement between the positions of the observed peaks in WAXS and GIWAXS measurements, as shown and discussed in section 6.2, it is possible to conclude, that the thermal degradation in the GIWAXS sample did not have a significant influence on the crystal structure.

6.2. Intermolecular Ordering in Bulk and Thin Films

The WAXS patterns of the three investigated PDPPs in comparison to that of P3HT measured at room temperature are shown in figure 6.5. The powder scattering patterns were measured after the samples underwent a thermal treatment. The PDPP[T]$_2$-T, PDPP[T]$_2$-T$_{DEG}$ and P3HT samples were ordered during cooling from the melt. The PDPP[Py]$_2$-T sample was ordered by annealing at a temperature below the melting temperature as discussed in section 6.1.2 (cf. fig. 6.4). The observed scattering peaks for each sample are numbered in ascending order based on their q-position. The numbering also takes into account the peaks observed in the GIWAXS measurements shown further below.

The scattering patterns of the investigated PDPPs and the scattering pattern of P3HT share certain similar features: a series of equidistant peaks in the q range from $0.3\,\text{Å}^{-1}$ to $1.2\,\text{Å}^{-1}$ and at least one additional peak in the q range from $1.5\,\text{Å}^{-1}$ to $1.8\,\text{Å}^{-1}$. These similarities can be understood in terms of the similarities of the general chain architecture of PDPPs and P3HT: both consist of rigid conjugated backbones of ring-like or fused-ring-like structures and flexible side chains attached to this backbone. Certain
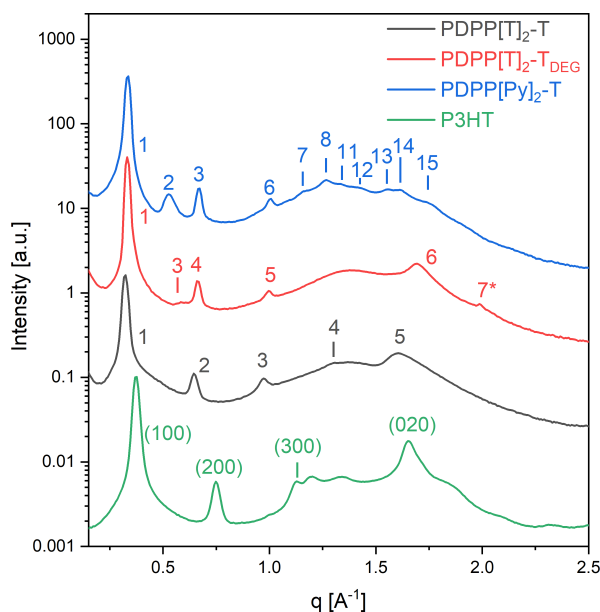
Figure 6.5.: Powder WAXS patterns of PDPP[T]$_2$-T (black) and PDPP[T]$_2$-T$_{DEG}$ (red) after crystallization by cooling from the melt and PDPP[Py]$_2$-T (blue) after annealing at 260 °C. A powder WAXS measurement of P3HT (green) crystallized from the melt is shown for comparison to emphasize similarities of molecular ordering in board-like semiconducting polymers. Curves are shifted on y-axis for better visibility. All measurements were performed at room temperature. Reprinted with permission from [213]. Copyright 2024 American Chemical Society.

motifs of molecular arrangement that are found in P3HT and are directly related to this architecture can therefore also be expected to be found in the investigated PDPPs. These packing motifs are: the periodic π-π-stacking of the ring-like structures of the conjugated backbones, giving rise to the $(0k0)$ reflection on one hand, and a regularly layered structure formed by layers of stacked backbones separated by layers of side chains, giving rise to a series of equidistant $(h00)$ reflections on the other hand.

In P3HT certain reflections can only be explained by modeling the crystal structure by a unit cell containing two monomers in the π-π-stacking direction. This results in the π-π-stacking peak being indexed as (020) reflection instead of (010) reflection [217]. In the investigated PDPPs all diffraction peaks observed in WAXS and GIWAXS measurements can be indexed without assuming more than one monomer per unit cell. Accordingly, the reflections ascribed to the π-π-stacking are indexed as (010) reflections. Based on the assumption of similar motifs of molecular arrangement of board-like chain molecules, some of the peaks in the scattering patterns of the investigated PDPPs can be indexed based on comparison to the scattering pattern of P3HT. Namely, the series of equidistant peaks can be identified as $(h00)$ reflections and one of the additional peaks in the q-range from $1.5\,\text{Å}^{-1}$ to $1.8\,\text{Å}^{-1}$ can be identified as (010) reflections. The d_{100} and d_{010} spacings determined from the WAXS measurements are given in table 6.1.
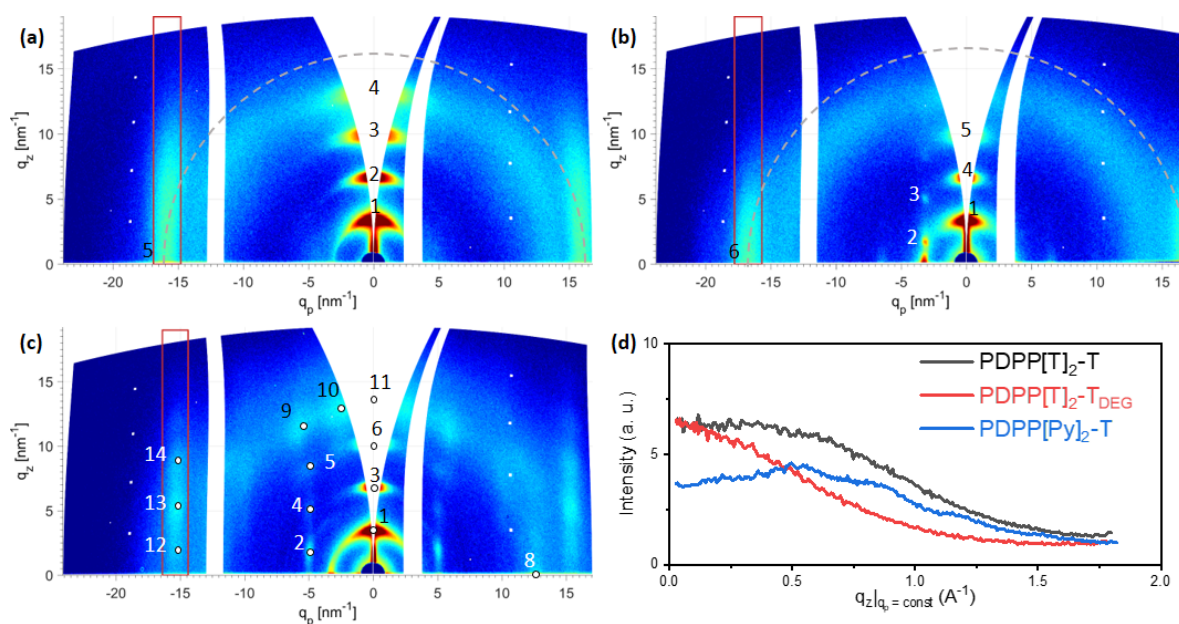
Figure 6.6.: GIWAXS measurements on thin films of (a) PDPP[T]$_2$-T and (b)PDPP[T]$_2$-T$_{DEG}$ after cooling from melt and (c) PDPP[Py]$_2$-T after annealing at 289 °C. Measurements were performed at an angle of incidence of 0.18°. (d) Intensity profiles in q_z direction of the π-π stacking peaks of the three polymers. Gray dashed circles in a) and b) show expected intensity distribution of peaks 5 and 6 respectively for completely randomly oriented crystals. Red rectangles in (a-c) indicates the area integrated to extract intensity profiles plotted in d). The integration range in b) and c) was similar but shifted in q_p according to the position of the π-π stacking peaks. Reprinted with permission from [213]. Copyright 2024 American Chemical Society.

The determined π-π-stacking distances of the investigated PDPPs are quite similar to that of P3HT ($d_{020,P3HT} = 3.81$ Å). In contrast, the d_{100} spacings of the PDPPs are significantly larger than that found in P3HT($d_{100,P3HT} = 16.68$ Å), which is to be expected based on the longer side-chains in the PDPPs. The indexing of the remaining peaks is not possible based on the observed similarity of the scattering patterns to that of P3HT alone. The remaining peaks can only be indexed with additional, more precise information about the position of the observed reflections in reciprocal space which can most easily be obtained from oriented samples. Therefore, GIWAXS-measurements on thin film samples were performed, taking advantage of the alignment effects promoting crystal orientation in thin films as discussed in the methods section.

The results of the GIWAXS measurements on thin film samples of PDPP[T]$_2$-T, PDPP[T]$_2$-T$_{DEG}$ and PDPP[Py]$_2$-T are shown in figure 6.6a-c. The PDPP[T]$_2$-T and PDPP[T]$_2$-T$_{DEG}$ thin films were ordered during cooling from the melt, while the PDPP[Py]$_2$-T thin film was ordered by annealing it at a temperature close to the melting temperature as discussed in more detail in section 6.1.2.
The GIWAXS patterns of all three samples show as series of (h00) reflections of high

intensity on the meridian. In contrast, the (h00) reflections on the equator, if visible at all, have signifiacntly lower intensity. Based on these strongly oriented (h00) reflections it is apparent, that all three PDPPs show a strong preference for edge-on orientation in thin films on silicon substrates when ordered from the melt or ordered at temperatures close to the melt. A similar preference for edge-on orientation in films of PDPP[T]$_2$-T and PDPP[Py]$_2$-T annealed at lower temperatures was also observed by Mueller and coworkers [210]. This preference for edge-on orientation is likely caused by the alkyl side chains, which are known to promote edge-on orientation at the interface to vacuum [31, 34], which is also observed in chapter 4. Additionally, as observed in chapter 5 in polythiophenes, ethylene glycol side chains also seem to induce edge-on orientation in thin films.

A further noteworthy feature is the clearly visible broadening of the (010) peaks of PDPP[T]$_2$-T and PDPP[T]$_2$-T$_{DEG}$ (peaks 5 and 6, respectively) in the GIWAXS patterns. Overall, these peaks are rather broad streaks parallel to the meridian instead of sharp localized peaks. In contrast, the scattering pattern of PDPP[Py]$_2$-T exhibits a certain variation in intensity along the q_z direction (peaks 12-14). The corresponding intensity profiles in q_z direction are shown in figure 6.6 d. The intensity profiles were extracted from the GIWAXS patterns by plotting the intensity integrated in a certain q_p range as a function of q_z. As the q_p position and the width of the (010) peak differed between the samples, the range of integration in q_p direction was chosen for each sample individually. The chosen integration ranges are indicated by the red rectangles in figure 6.6a-c.

6.2.1. Intermolecular Ordering of PDPP[T]$_2$-T

The scattering pattern of PDPP[T]$_2$-T is by far the least complex of the three investigated PDPPs. Following the arguments given above, the indexing of all visible peaks in the WAXS and GIWAXS patterns is straightforward: peaks 1-4 are (h00) reflections, and peak 5 is the (010) reflection. Based on these reflections the chains in PDPP[T]$_2$-T order such that the polymer backbones are arranged in stacks separated by layers of side chains, leading to a regularly spaced layered structure of backbone containing and side chain containing layers. Within one stack the backbones lie flat on top of one another and are regularly spaced in stacking direction.

The broadening of the intensity distribution of the (010) peak in q_z direction clearly deviates from a circular shape which one would have expected to observe if the broadening was caused by a broad orientational distribution. Instead the broadening has a more streak-like appearance, which clearly indicates that the broadening is at least partially caused by a limited correlation length. Specifically, as the broadening occurs in the q_z direction and the sample is edge-on oriented, it can be concluded that the (010) planes have a limited extent in the direction of the side chains. This implies, that neighbouring stacks of π-π-stacked backbones are randomly shifted against one another as sketched in figure 6.7a.

With the absence of any further visible peaks in WAXS as well as GIWAXS measurements there is no evidence for a periodic arrangement in the backbone direction and no
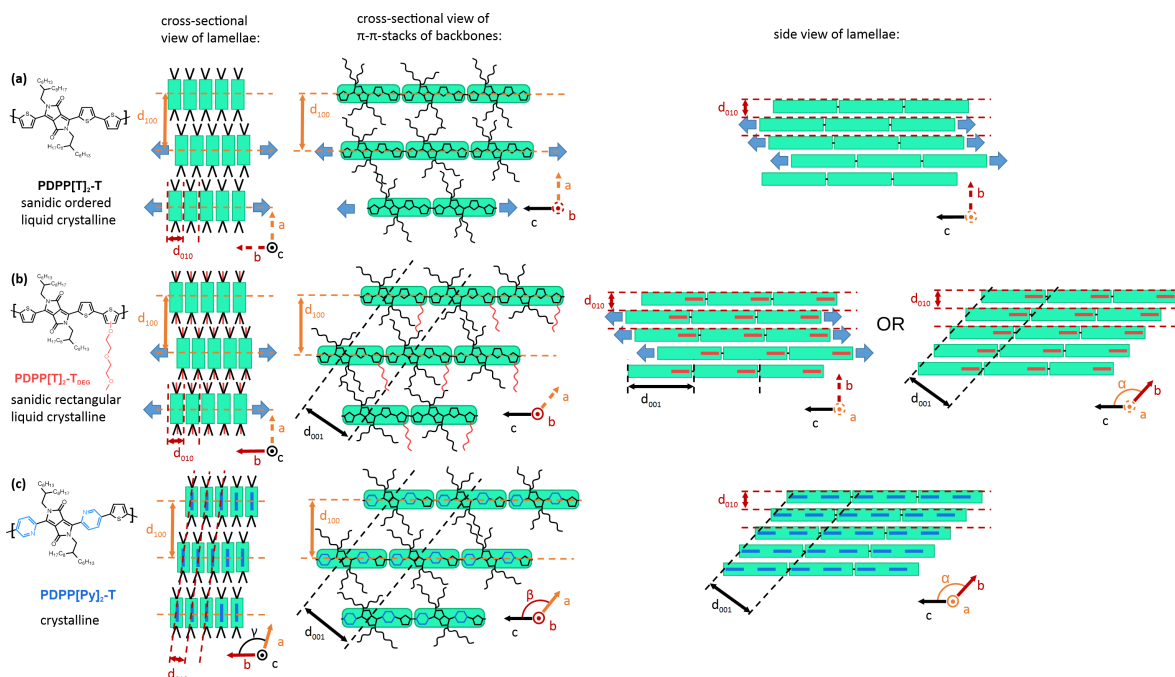
Figure 6.7.: Sketches of suggested molecular arrangements in PDPP[T]$_2$-T (top), PDPP[T]$_2$-T$_{DEG}$ (middle) and PDPP[Py]$_2$-T (bottom) that would give similar scattering patterns as the ones observed. Blue arrows indicate random shifts of neighbouring stacks or chains. Vectors a, b and c are shown to clarify the shown perspective and orientation. Vectors are drawn solid if the direction to the next monomer is well defined and dashed if only a approximation can be given due to lacking order. In PDPP[T]$_2$-T neighbouring stacked backbones are shifted randomly against one another in b and c direction. In PDPP[T]$_2$-T$_{DEG}$ neighbouring stacks are randomly shifted in b direction but registered in c direction. In PDPP[Py]$_2$-T neighbouring stacks are registered in b and c direction. Adapted with permission from [213]. Copyright 2024 American Chemical Society.

evidence for any coupling between the ordering in the (100) and (010) directions. Similar results were obtained by Zhang et al. [218] measuring transmission WAXS patterns from free-standing thin films of PDPP[T]$_2$-T. In those measurements also no reflections with mixed indices were observed and an additional (001) reflection was observed only upon mechanically straining the sample.

Concluding from these results, the ordering in PDPP[T]$_2$-T is of limited extent and can be classified as liquid crystalline. More precisely, the ordering in PDPP[T]$_2$-T can be classified as a sanidic ordered structure Σ_o according to the classification of liquid crystalline phases of board-like molecules introduced by Ebert et al. [45] and discussed in more detail in section 2.1.1.

The extracted positions of all peaks observed in the WAXS and GIWAXS measurements of PDPP[T]$_2$-T are given in table E.1.

6.2.2. Intermolecular Ordering of PDPP[T]$_2$-T$_{DEG}$

In the WAXS pattern of PDPP[T]$_2$-T$_{DEG}$ the peak labelled as peak 7* exhibits a series of unexpected properties. First of all, it is unusually sharp compared to the other peaks in the WAXS pattern. Second of all, it does not disappear upon heating the sample above the melting temperature. Last of all, no equivalent peak can be observed in the GIWAXS measurements. These aspects make it clear, that peak 7* does not originate from scattering from the polymer sample itself but is likely the result of scattering from a crystalline impurity instead.

Most of the remaining reflections observed in the WAXS and GIWAXS patterns of PDPP[T]$_2$-T$_{DEG}$ can readily be indexed based on the similarities to the scattering patterns of PDPP[T]$_2$-T. Namely, the peaks 1, 4 and 5 can be identified as $(h00)$ reflections and peak 6 as the (010) reflection. Analogous as for PDPP[T]$_2$-T these reflections indicate that the PDPP[T]$_2$-T$_{DEG}$ chains order in a way forming regularly spaced alternating layers of side chains and regularly stacked backbones. While the broadening in q_z-direction of the (010) peak in the GIWAXS measurement of PDPP[T]$_2$-T$_{DEG}$ is not as pronounced as for the (010) peak of PDPP[T]$_2$-T it still is more streak-like rather than a sharp peak. Therefore, the correlation length of the (010) planes in PDPP[T]$_2$-T$_{DEG}$ is still somewhat limited even if it is larger than the correlation length of the (010) planes in PDPP[T]$_2$-T.

In comparison to the WAXS measurement, the GIWAXS measurement of PDPP[T]$_2$-T$_{DEG}$ shows an additional reflection labelled as peak 2 in figure 6.6b. In the WAXS measurements this reflection is not visible as a separate peak because it is hidden within the right flank of the much more intense (100) reflection as these two peaks lie quite closely together on the $|\vec{q}|$ axis. As the sample is strongly edge-on oriented, evidenced by the fact that the $(h00)$ reflections found on the equator are significantly less intense than the $(h00)$ reflections found on the meridian, peaks 2 and 3 can clearly be attributed to edge-on oriented crystals. For edge-on oriented crystals all $(h00)$ reflections are located on the meridian and therefore peaks 2 and 3 must belong to a series of reflections with either k or $l \neq 0$. As the q_p value of the (010) reflection is quite large compared to the q_p values of peaks 2 and 3, the indices of peaks 2 and 3 have to contain an $l \neq 0$. Based on this, the simplest assumption is to index peak 2 as (001) reflection. Consequently, peak 3 then has to be indexed as (101) reflection. The existence of an (001) reflection indicates that the arrangement of the polymer chains is periodic along the backbone direction. The additional appearance of a peak with mixed (101) indices evidences that this ordering along the backbone direction is correlated across side chain layers. As the (001) reflection is not directly situated on the meridian but has a $q_z \neq 0$, it can be concluded that the backbones are shifted regularly from one stack to the next (cf. middle column in fig. 6.7b). Interestingly, a recently published article reports the observation of similar ordering in simulations of a conjugated polymer [49].

The angles $\beta^* \approx 61.8°$ (between (100) and (001) reflection) and $\gamma^* \approx 90°$ (between (100) and (010) reflection) can be directly taken from the GIWAXS measurement.

Regarding the ordering of backbones within one stack, there are two possible scenarios as sketched in the rightmost column in figure 6.7b. Either neighbouring backbones

within the same stack are shifted randomly against one another in chain direction or neighbouring chains within a stack are registered and the shift in chain direction from one chain to the next is regular and well defined. As there are no reflections with mixed k and l indices, there is no direct evidence for registration between chains within the same stack. However, if the chains within one stack were not registered, one would expect a certain broadening of the (001) reflection in q_p direction due to a limited correlation length of the (001) planes in the stacking direction. Therefore, as the (001) peak is rather sharp in q_p direction (cf. fig. 6.6b) the registration of chains within the same stack seems to be the more likely scenario.

Overall the PDPP[T]$_2$-T$_{DEG}$ sample exhibits a higher degree of order than the PDPP[T]$_2$-T sample. While neighbouring stacks are still shifted randomly against one another in π-π stacking direction, they are registered in chain direction. The driving force behind this registration cannot be derived from the measured data and can only be speculated on. Potentially, the registration between neighbouring stacks in PDPP[T]$_2$-T$_{DEG}$ is induced by a demixing tendency of the additional hydrophilic DEG side chains and the hydrophobic alkyl side chains.

Based on the appearance of the mixed (101) reflection, the structure of PDPP[T]$_2$-T$_{DEG}$ is quite similar to the sanidic rectangular phase Σ_r classified by Ebert [45], although in his case the correlation is observed between b and c direction instead. Additionally, in the case of PDPP[T]$_2$-T$_{DEG}$, the angle between the correlated directions, namely the a and c directions, is not equal to 90°. Therefore, a more precise name for the structure of PDPP[T]$_2$-T$_{DEG}$ would probably be sanidic oblique.

The extracted positions of all peaks observed in the WAXS and GIWAXS measurements of PDPP[T]$_2$-T$_{DEG}$ can be found in table E.2.

6.2.3. Intermolecular Ordering of PDPP[Py]$_2$-T

Based on the large number of visible reflections in the scattering patterns of PDPP[Py]$_2$-T this polymer appears to form a real 3-dimensional crystal. Again, the peaks 1, 3, 6, and 11 are readily identified as a series of (h00) reflections based on their position and regular spacing in the WAXS pattern. In contrast to the previous samples, the (010) can not be identified based on the WAXS pattern alone due to a multitude of different peaks that roughly match the expected q value, namely, peaks 12, 13 and 14. In the GIWAXS measurement these three peaks all lie on a line parallel to the q_z axis and have a regular spacing corresponding to q_{100}. Therefore, these three peaks clearly form a series of (h10) reflections. In similar cases involving other semiconducting polymer showing a series of (h10) reflections reported in literature, typically the most intense reflection is indexed as (010) reflection. [141, 31] Following these examples, peak 13 is indexed as (010) reflection. The peaks 12 and 14 are consequently indexed as ($\bar{1}$10) and (110) reflections respectively. The series of (h10) reflections shows, that in contrast to the previous two PDPP samples, the neighbouring stacks of π-π stacked backbones in PDPP[Py]$_2$-T are shifted regularly against one another in stacking direction (cf. left column in fig. 6.7c).

Following the same argumentation as presented for PDPP[T]$_2$-T$_{DEG}$ regarding the
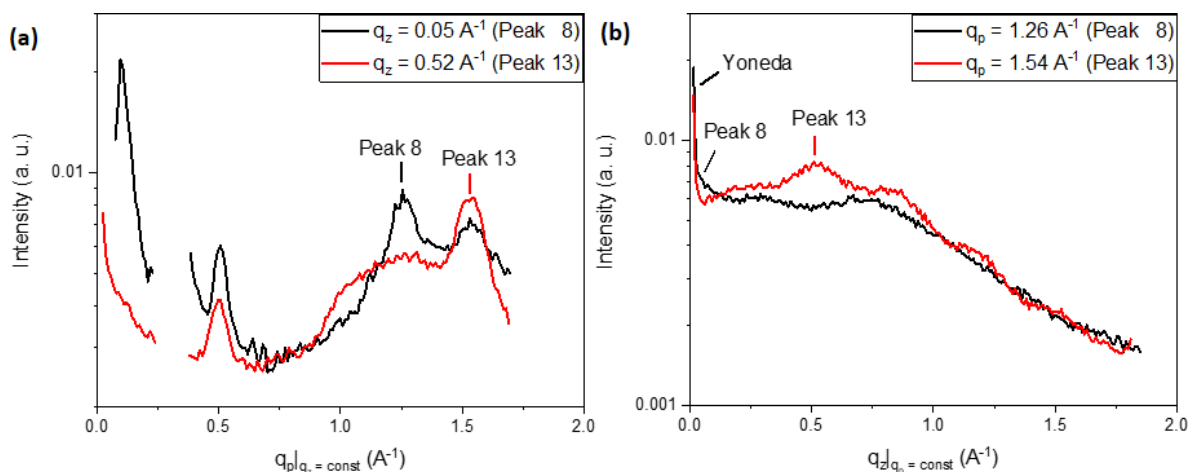
Figure 6.8.: Intensity line profiles in (a) q_p and (b) q_z direction extracted from GIWAXS measurement on thin film of PDPP[Py]$_2$-T. The width of the integration area was $0.1\,\text{Å}^{-1}$. Reprinted with permission from [213]. Copyright 2024 American Chemical Society.

peaks 2 and 3, the peaks 2, 4, and 5 in PDPP[Py]$_2$-T can be identified as a series of ($h01$) reflections and are therefore indexed as (001), (101) and (201) respectively. From the existence of a series of ($h01$) reflections, it is clear that the PDPP[Py]$_2$-T chains have a periodic ordering along the backbone direction and that this ordering is correlated across side chain layers. The non-zero q_z value of the (001) reflection indicates that the (001) and (100) planes are not perpendicular to one another (cf. middle column in fig. 6.7c).

The observed correlations between the ordering in all three directions allow to conclude, that PDPP[Py]$_2$-T is indeed crystalline. Based on the reflections indexed so far, all parameters of the reciprocal unit cell except for the angle α^* (the angle between b^* and c^*) can be determined. The determination of α^* requires a reflection with mixed k and l indices. Peak 8 can clearly be identified as a reflection with mixed k and l indices based on its q_p position in the GIWAXS measurement, as it lies in between the q_p positions of the (010) and (001) reflections but is no integer multiple of the q_p position of the (001) reflection. Therefore, in the following the focus shifts towards the determination of the exact position of peak 8 and its indexing, both of which are more complicated than for the previously discussed peaks.

Although peak 8 is not well visible in the 2D-image of the GIWAXS measurement, its existence can easily be confirmed in the q_p and q_z line profiles extracted from said image as shown in figure 6.8. Comparing the line profiles in q_p direction of peak 8 and the (010) reflection (peak 13) it is evident that peak 8 is actually a well defined peak with similar intensity as peak 13 (cf. fig. 6.8a). While the q_p position of peak 8 can easily be determined its q_z position is harder to localize exactly as can be seen in figure 6.8b. Both the q_z line profiles of peak 8 and peak 13 show increased intensity close to $q_z = 0$ caused by the Yoneda effect [219]. However, the differences between the two

Table 6.2.: Possible Miller indices of peak 8 and resulting α^* and resulting best fits for Peak 7 ($q = 1.164\,\text{Å}^{-1}$).

Peak 8 Indexing	resulting	Peak 7 Indexing	Peak 7 calculated
$(h\ k\ l)$	$\alpha^*[°]$	$(h\ k\ l)$	$|q|[\text{Å}^{-1}]$
$\bar{3}\ 1\ 3$	118.6	$3\ \bar{1}\ \bar{2}$	1.159
$\bar{2}\ 1\ 1$	119.8	$\bar{2}\ 1\ 2$	1.145
$\bar{1}\ 1\ \bar{1}$	44.2	$3\ 0\ \bar{2}$	1.185
$0\ \bar{1}\ 3$	45.7	$1\ \bar{1}\ 2$	1.164
$\bar{1}\ 2\ \bar{4}$	14.0	$0\ \bar{1}\ 5$	1.147

curves with regard to the decay of this increased intensity with increasing q_z evidences an additional intensity contribution around $q_z \approx 0\,\text{Å}^{-1}$ in the q_z line profile of peak 8 that can be attributed to peak 8. The overlap of peak 8 and the increased intensity due to the Yoneda effect prevents an accurate determination of the q_z position of peak 8 which can only be narrowed down to an approximate range of $q_z \approx 0.0\,\text{Å}^{-1}$ to $0.05\,\text{Å}^{-1}$. Based on the determined position of peak 8 and the known q_p and q_z components of $\vec{G}_{100}$, $\vec{G}_{010}$ and $\vec{G}_{00l}$ a list of possible Miller indices can be identified. By iterating h, k and l from -5 to 5 and collecting all resulting $\vec{G}_{hkl}$ with a q_z component in the range of $0.0\,\text{Å}^{-1}$ to $0.05\,\text{Å}^{-1}$. The determined Miller indices can then be used to determine α^* as described in Appendix C.

Not all determined indices result in a valid solution for α^*. For example, for some hkl-combinations the q_p value of $\vec{G}_{hkl}$ is larger than the q_p value of peak 8 for any given angle α^*. The five hkl-combinations that yielded a valid α^* are listed in table 6.2. The most plausible of these five unit cells can be determined by calculating the reciprocal lattice vector $\vec{G}_{hkl}$ that gives the best fit for peak 7 ($q = 1.164\,\text{Å}^{-1}$) seen in the WAXS pattern for each individual unit cell and then determining which unit cell results in the best fit of peak 7 overall. As can be seen from table 6.2, the best fit for peak 7 was obtained with $\alpha^* = 45.7°$ and therefore, the most plausible indexing of peak 8 is $(0\bar{1}3)$. The reciprocal lengths a^*, b^* and c^* for the final reciprocal unit cell were determined from the WAXS pattern as the peaks there are sharper compared to the GIWAXS pattern and their position therefore can be determined more accurately. The parameters of the final reciprocal and resulting real unit cells are given in table 6.3.

The determined unit cell is triclinic, which is in contrast to the orthorhombic unit cells suggested for other PDPPs in the literature, although without presenting clear evidence or detailed explanation. [38, 39] While all peaks visible in the WAXS pattern of PDPP[Py]$_2$-T could be indexed, no (hkl) reflection corresponding to peaks 9 and 10 in the GIWAXS pattern could be found. These two peaks show qualitative differences

Table 6.3.: Unit Cell Parameters of the Investigated PDPPs

	$a^*[\text{Å}^{-1}]$	$b^*[\text{Å}^{-1}]$	$c^*[\text{Å}^{-1}]$	$\alpha^*[°]$	$\beta^*[°]$	$\gamma^*[°]$
Reciprocal Unit Cell						
PDPP[T]$_2$-T	0.324	1.605	-	-	-	≈ 90
PDPP[T]$_2$-T$_{DEG}$	0.331	1.698	0.366	-	61.8	≈ 90
PDPP[Py]$_2$-T	0.334	1.620	0.530	45.7	70.1	71.3
Real Unit Cell						
	$a[\text{Å}]$	$b[\text{Å}]$	$c[\text{Å}]$	$\alpha[°]$	$\beta[°]$	$\gamma[°]$
PDPP[Py]$_2$-T	20.16	5.46	16.81	131.4	99.9	97.1

compared to the other peaks observable in the GIWAXS pattern, as they are less intense and are relatively broad. While the exact origin of these peaks is unclear they might potentially be a result of diffuse scattering. The introduction of a further chemical heterogeneity, namely the pyridine rings, along the chain in PDPP[Py]$_2$-T compared to PDPP[T]$_2$-T, apparently led to an increased registration of order between different directions.

The extracted positions of all peaks observed in the WAXS and GIWAXS measurements of PDPP[Py]$_2$-T are given in table E.3, together with the expected positions calculated according to the determined unit cell.

6.3. Thin Film Morphology

The surface morphologies of the same thin film samples on silicon substrates that were investigated using GIWAXS were studied with peak force AFM. The obtained height and adhesion images (Fig. 6.9) revealed significant differences in the surface morphologies of the different samples. The PDPP[T]$_2$-T sample, which showed the least amount of ordering in the GIWAXS measurements, has a granular surface morphology (cf. fig. 6.9a and d). The majority of the grains are approximately circular in shape and only a few grains are somewhat elongated. The grains have an average diameter of 63 nm and presumably are ordered domains surrounded by amorphous material.
In contrast, the two more ordered samples PDPP[T]$_2$-T$_{DEG}$ and PDPP[Py]$_2$-T show elongated lamellae (cf. fig. 6.9b,e, and d,f), a feature commonly found in semicrystalline polymers. Based on these observations, the regular ordering of the polymer chains in backbone directions, as evidenced by the (001) reflections in the GIWAXS measurements, seems to be a prerequisite for the formation of elongated lamellae. Despite both PDPP[T]$_2$-T$_{DEG}$ and PDPP[Py]$_2$-T showing lamellar structures their overall morphologies differ significantly. While the PDPP[T]$_2$-T$_{DEG}$ film exhibits very long and stacked lamellae with an average long period of 56 nm, the morphology of the PDPP[Py]$_2$-T film consists mostly of shorter individual lamellae surrounded by larger amorphous regions and only few instances of stacked lamellae with an average long period of 30 nm.
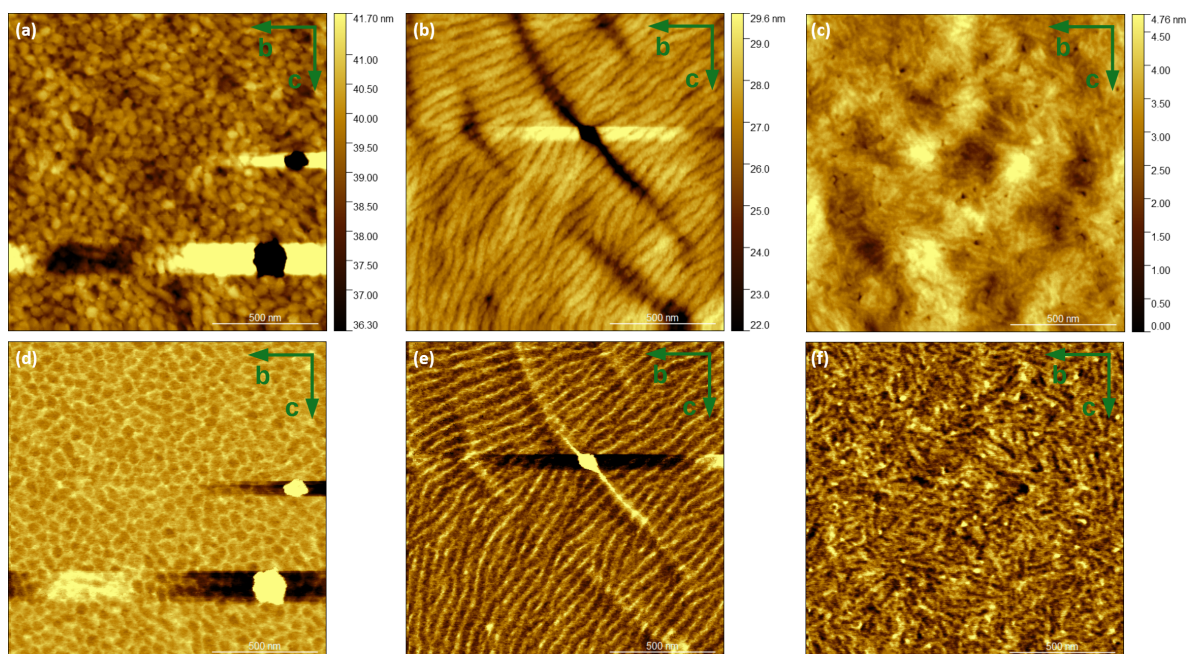
Figure 6.9.: AFM height (a, b, c) and adhesion (d, e, f) images of PDPP[T]$_2$-T (a, d), PDPP[T]$_2$-T$_{DEG}$ (b, e) and PDPP[Py]$_2$-T (c, f) on silicon after thermal treatment. The bright and dark horizontal streaks are artifacts caused by sudden large height variations. The green arrows illustrate the chain orientation relative to the imaging plane. As the chain direction is always roughly perpendicular and the π-π stacking direction roughly parallel to the long axis of the lamellae, the specific directions of b and c vary throughout the images.Reprinted with permission from [213]. Copyright 2024 American Chemical Society.

At first glance, these morphological differences seem counter-intuitive, as PDPP[Py]$_2$-T is more ordered on a molecular scale as evidenced by the scattering results. The morphological differences between these two films are possibly caused by differences in molecular weight and by the fact that the PDPP[Py]$_2$-T film was only annealed below the melting temperature in contrast to being ordered during cooling from the melt as was the case for the PDPP[T]$_2$-T$_{DEG}$ film.

An additionally noteworthy feature are the cracks visible on the surface of the PDPP[T]$_2$-T$_{DEG}$ film. While their exact origin is unclear, one plausible explanation might be that they result from internal stresses in the film caused by thermal contraction upon cooling during the thermal program used to order the sample. Strikingly, a common feature of all visible cracks is that they run perpendicular to the lamellae and are therefore parallel to the chain direction. Based on the dominant edge-on orientation of this film (cf. fig. 6.6b) it is possible to conclude that the lamellae broke apart along the π-π-stacking planes.

6.4. Conclusion

In this chapter the molecular ordering of three different PDPPs was investigated in detail by measuring WAXS patterns of isotropic bulk samples and GIWAXS patterns of highly oriented thin films. Additionally the relation between annealing temperature and crystal orientation in thin films was investigated to find an appropriate annealing program that results in highly oriented films while keeping the extent of thermal degradation in an acceptable range. In these measurements all samples showed a strong dependence of the preferred crystal orientation in thin films on silicon substrates on the annealing temperature. As seen in section 6.1.2, the originally spin-coated films showed a preference for face-on alignment when annealed at lower temperatures. With increasing annealing temperature the films first exhibited a bimodal orientation distribution of face-on and edge-on oriented crystals before becoming almost exclusively edge-on oriented when annealed close to the melting temperature.

The molecular arrangement of the investigated PDPPs exhibit certain common features despite significantly differing in the degree of order. All investigated PDPPs show regular π-π stacking and regular spacing in the side-chain direction. PDPP[T]$_2$-T arranges in a sanidic ordered liquid crystalline phase. Similarly, PDPP[T]$_2$-T$_{DEG}$ also shows liquid crystalline order but arranges in a more ordered sanidic rectangular or oblique liquid crystalline phase. In contrast, PDPP[Py]$_2$-T is crystalline and has a triclinic unit cell and therefore is the most ordered of the three. While the exact mechanism behind the increase in order is unclear, one can speculate that the introduced chemical modifications present certain heterogeneities along the backbone that promote a better registration between neighbouring stacks of backbones.

Clear difference between the mesoscopic morphology of the thin PDPP films were observed in AFM experiments. Only the thin films of the two more ordered PDPPs show a lamellar morphology commonly observed in semicrystalline polymers.

Overall the results presented in this chapter contribute to closing the gap in knowledge on the molecular arrangement in the solid state of PDPPs which so far was only available for a few selected PDPPs. Furthermore, similarly detailed investigations of the structure of sanidic mesophases in conjugated polymers have so far not been reported in literature. Additionally the results demonstrate that the molecular ordering in PDPPs can be quite sensitive to chemical modifications of the chains, underlining that deducing the molecular arrangement in a specific PDPP based on the molecular arrangement in chemically similar PDPP is not generally possible. This emphasizes the necessity of further structural investigations in other PDPPs to further the understanding of how the molecular ordering is influenced by different modifications to the chemical structure.

7. Summary

In this thesis three different series of semiconducting polymers were investigated in bulk and in thin films. Their phase behavior in bulk was studied using calorimetry (DSC) and powder x-ray scattering (WAXS), while their ordering, preferred crystal orientation and surface morphology in thin films was investigated using grazing incidence x-ray scattering (GIWAXS) and surface imaging (AFM).

The first series was investigated to elucidate the effect of polar end groups of the side chains on the crystal orientation in thin films of semiconducting polymers using polythiophenes as a model system. In this series four polythiophenes with differently polar end groups on their side chains were investigated. It was possible to prove the initial hypothesis, that the addition of polar end groups to the side chains hinders the formation of edge-on oriented crystals at the interface to vacuum. In P3CNHT, the polythiophene with end group with the largest dipole moment, the formation of edge-on crystals in thin films was suppressed completely. This allowed to produce films of upto 200 nm thickness on graphene substrates with a complete face-on crystal orientation. These results are especially relevant for organic photovoltaic devices in which edge-on oriented crystals are considered to be unfavorable for charge transport.

Further it was shown, that the molecular arrangement in the crystalline phase was almost unaffected by the different end groups. The unit cells determined for the investigated polythiophenes were quite similar and mainly showed a variation in the regular spacing in the side chain direction which is to be expected given the different lengths of the side chains. Overall, the polar end groups do not appear to significantly effect the molecular packing of polythiophenes in the crystalline phase.

Furthermore, initial experiments on thin films of a modified PDPP strongly suggest that this method of suppressing edge-on oriented crystallization in thin films is not limited to polythiophenes but can likely be transferred to many other semiconducting polymers.

Based on the results obtained in the second series of polythiophenes with ethylene glycol side chains, it can also be concluded, that it is truly the dipole moment of the end group that is important for controlling the crystal orientation and not the hydrophilicity of the side chain in general.

The major advantage of the approach of using chemical modifications to control the dominant crystal orientation in thin films of polythiophenes compared to other methods is, that the obtained distribution of crystal orientations is a result of self organization upon cooling from the melt. Therefore, the resulting structures and crystal orientations can be expected to be closer to thermodynamic equilibrium and thus thermodynamically more stable.

In the second series the influence the linkage of ethylene glycole (EG) side chains to the backbone in polythiophenes has on crystal structure and performance in OECT devices was investigated. This series consisted of three different polythiophenes in which EG side chains were attached to the polythiophene backbone via alkyl spacers of different lengths. It was found, that the crystallinity and many other parameters (e.g. charge carrier mobility, volumetric capacitance and transconductance in OECT) of these polymers are strongly affected by the length of the alkyl spacer, showing a clear improvement in most parameters with increasing spacer length. Accordingly P3MEEET, the polymer with the longest alkyl spacer in the series, was found to have one of the highest hole mobilities reported for a polythiophene homopolymer with polar side chains ($\mu_{OFET} = 5 \times 10^{-3}\,\mathrm{cm^2/(V\,s)}$) and also showed the best performance in OECT devices within the investigated series. Overall, the results of the investigations of the different polythiophenes with EG side chains demonstrate how significantly seemingly minor modifications to the chemical structure of the side chains can influence the intermolecular ordering and the performance of these material in electronic devices.

In the third series three different PDPPs were investigated. It was shown, that in general the degree of ordering in PDPPs can vary significantly, ranging from various sanidic liquid crystalline phases to crystalline phases. Furthermore, it was demonstrated that chemical modifications commonly used to alter the electronic, optic and solubility properties of semiconudcting polymers can also have a strong effect on the intermolecular ordering in these materials. Additionally, the crystal unit cell of PDPP[Py]$_2$-T could be determined. While a large number of different PDPPs have been synthesized and reported in literature [37], the molecular ordering has only been investigated for a few select PDPPs. Therefore, the in-depth investigation of the intermolecular ordering in PDPP presented in this thesis contributes to closing the gap in knowledge regarding the molecular ordering in PDPPs and to which extend the ordering can be affected by introduced chemical modifications.

In general, the results presented in this thesis clearly demonstrate that the ordering in semiconducting polymers can be significantly affected by even seemingly minor modifications to their chemical structure. On one hand, this implies that specific aspects of the intermolecular arrangement, for example the preferred crystal orientation in thin films, can be controlled through targeted modifications of the chemical structure of the polymers. In this regard, side chain engineering seems especially promising as the side chains typically have a rather limited direct effect on the electronic properties of the backbones. On the other hand, this highlights that detailed investigations of the molecular arrangement in semiconducting polymers are a crucial, yet often neglected, step in understanding the relationship between introduced chemical modifications and observed material properties.

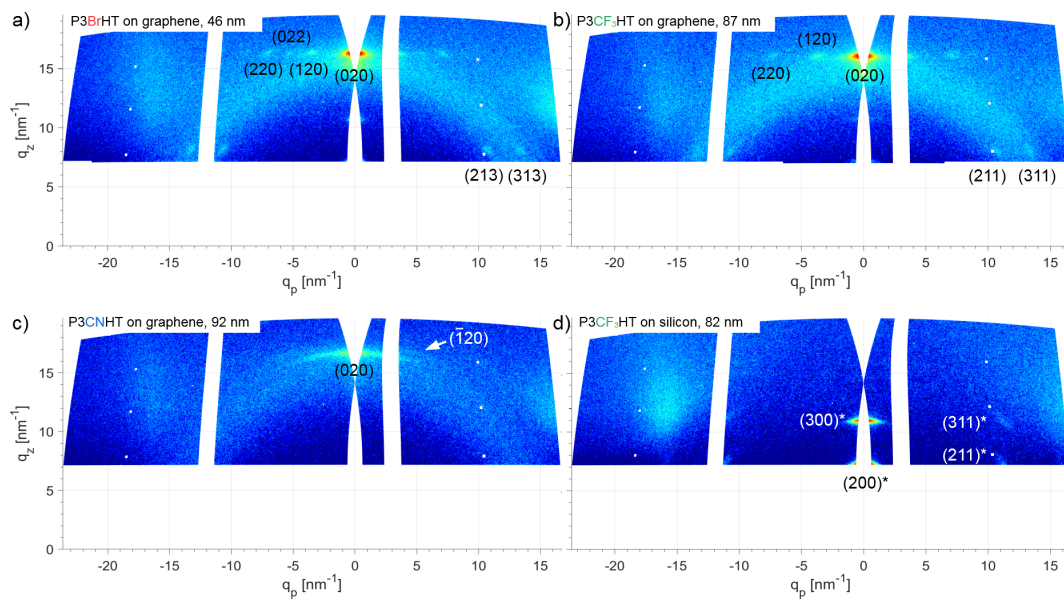# A. Additional WAXS and GIWAXS Measurements of P3BrHT, P3CF$_3$HT and P3CNHT

Figure A.1.: WAXS patterns of thin films of a) P3BrHT, b) P3CF$_3$HT and c) P3CNHT on graphene and d) P3CF$_3$HT on silicon substrates measured at an angle of incidence of $\alpha_i = 10°$. Samples were measured after crystallization by cooling from the melt. Reflections originating from edge-on oriented crystals are indicated with * in d).

Measuring the x-ray scattering pattern of thin films at higher angles of incidence α_i allows to probe regions of the reciprocal space that are not accessible at lower angles of incidence. As a consequence of the measurement geometry the reciprocal space perpendicular to the substrate (q_z-axis) is only probed at the one point where the scattering angle 2Θ is equal to $2\alpha_i$. Thus to probe the q_z-axis at higher q_z-value, it is necessary to increase the angle of incidence. In the scattering patterns converted to q_z-q_p space this can be seen by the shifting of the origin of the "wedge" located on the q_z-axis to higher q_z values.

Scattering patterns of thin films of P3BrHT, P3CF$_3$HT and P3CNHT measured at an angle of incidence of $\alpha_i = 10°$ are shown in figure A.1. The GIWAXS measuremetns

of the same samples at measured at smaller α_i are shown in figure 4.3b-e) in section 4.1. As seen from the measurements obtained at $\alpha_i = 10°$ the (020) reflection that was not visible in the measurements at small α_i is now visible.

There are several further advantages of measurements at high angles of incidence. For one, the intensity of the reflected primary beam is significantly weaker than at small α_i and therefore scattering from the reflected primary beam gives no significant contribution to the observed scattering pattern. Secondly, the larger angles of incidence also result in the footprint of the primary beam becoming much smaller than the sample length, resulting in much narrower peaks. Additionally the smaller foot print of the primary beam on the sample means that small offsets in sample placement in beam direction will have no effect as only some middle part of the sample will contribute to the scattering.
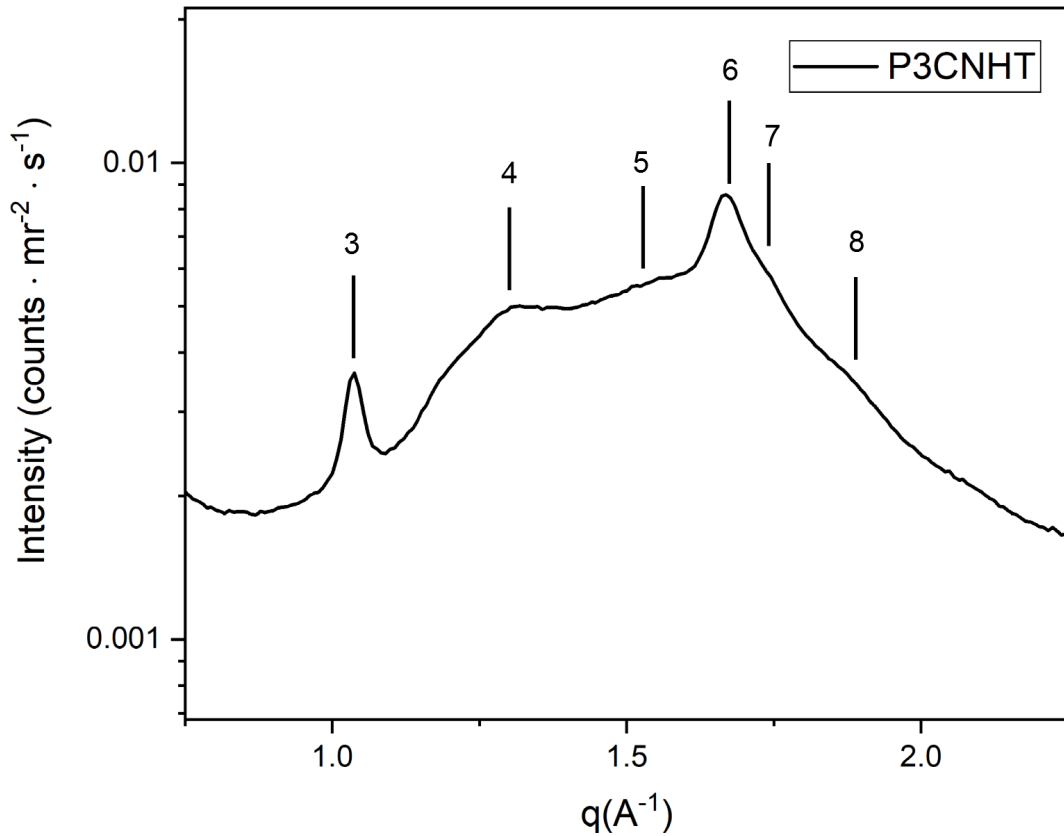

Figure A.2.: Enlarged section of the WAXS patterns of P3CNHT after crystallization from the melt. Besides the (300) and (020) reflections labeled with 3 and 6 respectively, multiple other peaks with low intensity are visible. The black vertical lines represent the estimated positions of the peaks.

Figure A.2 shows an enlarged section of the WAXS pattern of P3CNHT shown in figure 4.3a) in section 4.1. The enlarged scattering patterns illustrates, that there are several additional features visible besides the (h00) and (020) reflections (i.e. peaks 3 and 6). And while these features are most likely crystalline reflections they are of low

intensity and quite broad making it impossible to accurately determine their position. Additionally peak 5 looks exceptionally broad and is most likely a superposition of multiple peaks.

All scattering peak positions observed in the powder WAXS measurements and thin film measurements (fig. 4.3 in section4.1 and fig. A.1) are tabulated in appendix D. Where possible, the peak positions in thin film measurements were determined from the measurements at 10 as they are more accurate.

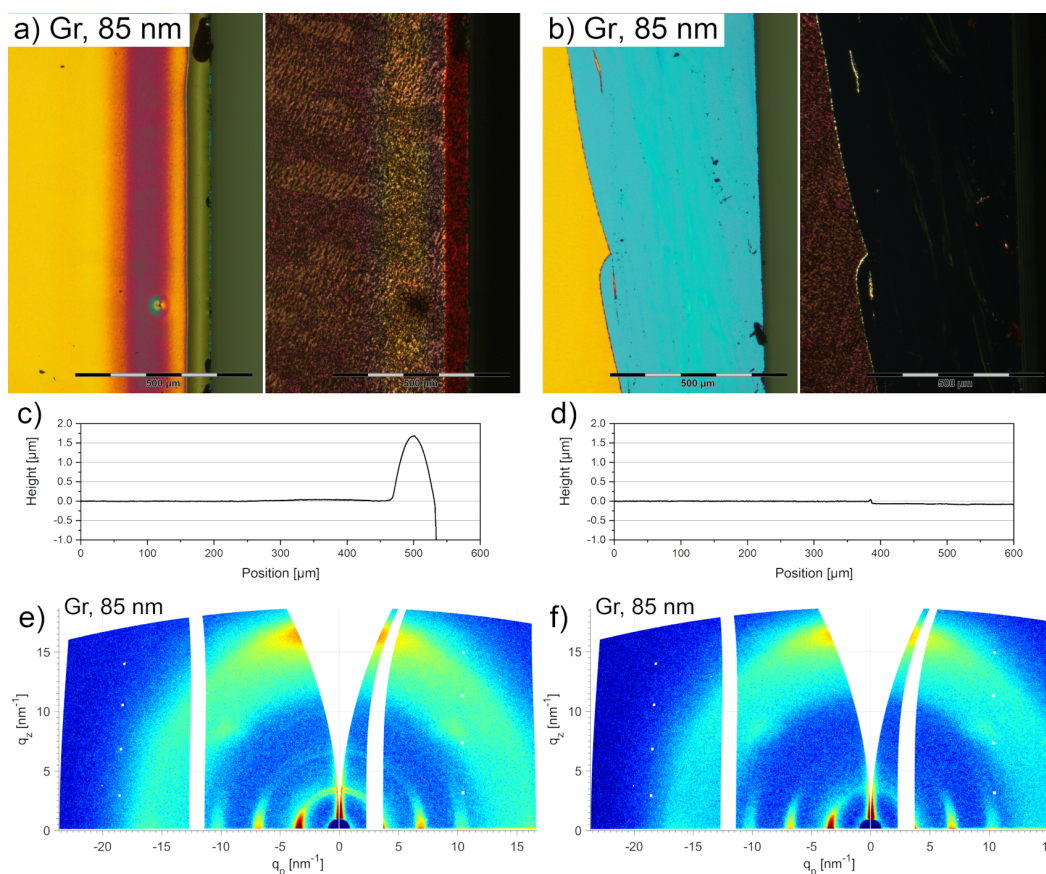# B. Influence of the Edges of Spin-Coated Films on GIWAXS Patterns

Figure B.1.: Optical microscopy images of the edge of a 85 nm thick P3CNHT film on graphene a) before and b) after removing the edges with a scalpel. Left and right halves of the microscopy images depict the same regions recorded with open (left) and crossed polarizers (right). c-d) Corresponding height profiles measured with a profilometer. The height here is given relative to the surface of the homogeneous film in the central areas of the substrate. e-f) Corresponding GIWAXS patterns.

All thin films prepared in the context of this thesis were prepared via spin-coating of polymer solution of different concentrations onto solid substrates. While the central areas of films prepared through spin-coating usually are quite smooth and are of relatively uniform thickness, the edges of the films tend to show significant thickness variations. For measurement techniques probing the thin films locally such as AFM and optical microscopy the edges can easily be avoided and thus have no influence on the measurement results. In contrast, for measurement techniques probing the sample by averaging over large areas of the sample, such as GIWAXS, the edges cannot be avoided. Therefore, if the properties of the material on the edges differs significantly from the properties of the material in the continuous film, the edges can have a non-negligible influence on the measurement result. This is demonstrated on the example of a 85 nm thick P3CNHT film on graphene in figure B.1.

Figure B.1 a) shows the edge of the film crystallized from the melt. The left half was recorded with open polarizers, while the right half shows the same area recorded with crossed polarizers. Based on the coloration of the image recorded with open polarizers and the corresponding height information obtained from a profilometer measurement (cf. fig. B.1 c) a series of different areas can be discerned. Going from left to right these are: continuous film of uniform thickness (yellow area), slightly thicker film (broad dark red stripe), thin stripe of thinner film (thin orange/yellow stripe), high ridge of polymer material at edge of film (thin stripe of various green shades), background beyond the edge of the substrate (uniform green area). From the image recorded with crossed polarizers it can be concluded that all regions on the substrate contain crystalline material since they are all birefringent. As can be seen from the profilometer measurement (cf. fig. B.1 c), the ridge, while less then 100 µm wide, can reach heights of upto 20 times the thickness of the uniform film. The two ridges on opposing edges of the substrate therefore represent a relevant fraction of the total scattering volume in GIWAXS experiments and thus their contribution to the scattering pattern cannot be neglected. Accordingly, the rims can have a significant influence on the measured scattering patterns, especially if the polymer crystals in the rim differ from those in the continuous film in terms of orientation or unit cell parameters. This can be seen in the GIWAXS pattern shown in (cf. fig. B.1 e). Besides the strong $(h00)$ reflections on the horizon coming from the face-on oriented crystals in the homogeneous film, additional (100) and (200) reflections are visible on the meridian indicating the presence of edge-on oriented crystals. Both of these reflections are clearly split into two individual intensity peaks with slightly different q-values. This splitting is not caused by the presence of crystals with different unit cell parameters (i.e. polymorphs) but by different sample to detector distances of the same type of crystals. Thus the edge-on oriented crystals giving rise to the split (100) and (200) reflections on the meridian can be located to the rims at the edges of the sample.

The microscopy images of an edge of the same P3CNHT sample after removing the rims and the slightly thicker area of the film with a scalpel can be seen in figure B.1 b). Based on the coloration of the image recorded with open polarizers and the corresponding height information obtained from a profilometer measurement (cf. fig. B.1 d) three different areas can be discerned: the continuous film of uniform thickness (yellow

area), the mostly bare substrate (light blue) and the background beyond the edge of the substrate (uniform green area). From the image recorded with crossed polarizer it is evident that most of the birefringent crystalline material on the edge of the substrate has been removed successfully. The GIWAXS pattern obtained from the sample after removal of the material on the edges of the substrate is shown in figure B.1 f). The clear absence of the split (100) and (200) reflections previously visible on the meridian proves that associating the corresponding edge-on crystals with the high rims on the edges of the thin film was indeed correct.

In conclusion, the spin-coating process results in films with rims at the edges of the substrate that can be significantly higher than the film thickness of the continuous film of homogeneous thickness in the central areas of the substrate. In cases where the crystals formed in these rims have a different orientation or a different unit cell compared to the crystals found in the continuous film, these rims should be mechanically removed before measuring GIWAXS patterns as to prevent obtaining potentially misleading data. In cases where the crystals in the rims do not significantly differ from the crystals in the continuous film the removal of the rims is usually not necessary as the presence of the rims does not significantly alter the obtained scattering patterns. One exception to this are surface sensitive GIWAXS measurements as the angle of incidence is not well controlled for the rims. For example, an average slope in the rim corresponding to a height increase of $1.5\,\mu m$ per $50\,\mu m$ would lead to an offset in the angle of incidence of $\Delta\alpha_i = \arcsin 1.5/50 = 1.72°$. Consequently, at angles of incidence below the critical angle of the polymer where only the upper layers of the continuous film contribute to the scattering, the rims would still contribute in their entirety.
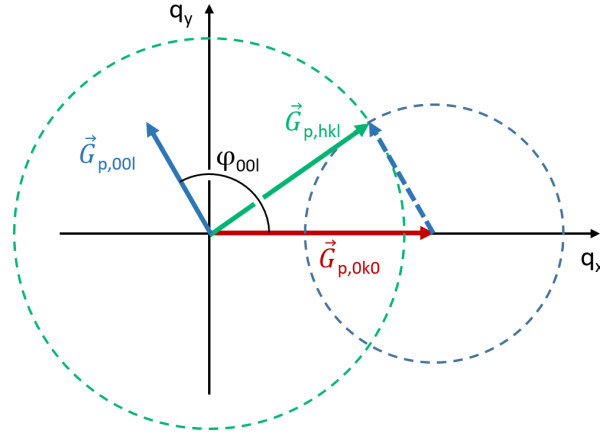
C. Determination of α^* for PDPP[Py]$_2$-T

Figure C.1.: Sketch of the q_x-q_y-plane in reciprocal space with the projections of the $\vec{G}_{0k0}$, $\vec{G}_{00l}$ and $\vec{G}_{hkl}$ vectors onto the plane. As $\vec{G}_{h00}$ is parallel to the q_z axis the direction of the $\vec{G}_{p,hkl}$ is solely given by the vectorial addition of $\vec{G}_{p,0k0}$ and $\vec{G}_{p,00l}$. The vector $\vec{G}_{p,hkl}$ has to lie on the green circle with the radius of $|\vec{G}_{p,hkl}|$ determined from GIWAXS measurements. Additionally $\vec{G}_{p,hkl}$ has to lie on the blue circle with radius $|\vec{G}_{p,00l}|$ (also determined from GIWAXS) around the tip of $\vec{G}_{p,0k0}$. The intersect of both circles defines the directions of $\vec{G}_{p,hkl}$ and $\vec{G}_{p,00l}$. Therefore, if $|\vec{G}_{p,0k0}|$, $|\vec{G}_{p,00l}|$ and $|\vec{G}_{p,hkl}|$ are known, one can determine the azimuthal angle ϕ_{00l} of the reciprocal lattice vector $\vec{G}_{00l}$. All measurements were performed at room temperature. Reprinted with permission from [213]. Copyright 2024 American Chemical Society.

As discussed in section 3.4.3, the reciprocal space of the oriented thin film samples has a cylindrical symmetry. Accordingly, the reciprocal lattice vectors $\vec{G}_{hkl}$ can be described using cylindrical coordinates, i.e. by the radial length $G_{p,hkl}$, the height $G_{z,hkl}$ and the azimuthal angle ϕ_{hkl}. The values of $G_{p,hkl}$ and $G_{z,hkl}$ can be directly determined from the q_p- and q_z-position of a (hkl)-reflection observed in a GIWAXS measurement.

As discussed in section 6.2, the thin films of PDPP[Py]$_2$-T on silicon substrates show a strong edge-on orientation of crystals. Based on the (100) reflection visible on the q_z-axis and the also visible (010) and (001) reflections, all parameters of the reciprocal unit cell of PDPP[Py]$_2$-T except for α^* can be determined. The a^*, b^* and c^* parameters

can be directly are equivalent to $|\vec{G}_{100}|$, $|\vec{G}_{010}|$ and $|\vec{G}_{001}|$ respectively. The angle β^*, between $\vec{a}^*$ and $\vec{c}^*$, and the angle γ^*, between $\vec{a}^*$ and $\vec{b}^*$, can be determined by the following relationships:

$$\beta^* = \arctan(G_{p,001}/G_{z,001}) \tag{C.1}$$

$$\gamma^* = \arctan(G_{p,010}/G_{z,010}) \tag{C.2}$$

The angle α^* between $\vec{b}^*$ and $\vec{c}^*$ cannot be determined as the azimuthal angles ϕ_{0k0} and ϕ_{00l} of the reciprocal lattice vectors $\vec{G}_{0k0}$ and $\vec{G}_{00l}$ in the coordinate system of a single crystal are unknown. However, the orientation of coordinate system of the reciprocal space of the single crystal can be chosen freely. Accordingly, the angle ϕ_{0k0} can be set to 0 by orienting the coordinate system such that the reciprocal lattice vectors $\vec{G}_{0k0}$ lie in the q_x-q_z-plane. The angle ϕ_{00l} can than be determined based on the position of a reflection with mixed indices with $k \neq 0$ and $l \neq 0$. The lattice vector $\vec{G}_{hkl}$ corresponding to such a reflection is defined by:

$$\vec{G}_{hkl} = h \cdot \vec{G}_{100} + k \cdot \vec{G}_{010} + l \cdot \vec{G}_{001} \tag{C.3}$$

This equation also holds for $\vec{G}_{p,hkl}$, the projections of the $\vec{G}_{hkl}$ onto the q_x-q_y-plane:

$$\vec{G}_{p,hkl} = \vec{G}_{p,0k0} + \vec{G}_{p,00l} \tag{C.4}$$

As the reciprocal lattice vector $\vec{G}_{h00}$ is parallel to the q_z-axis, its projection onto the q_x-q_y-plane ($\vec{G}_{p,h00}$) is equal to zero and does not contribute. The sketch in figure C.1 illustrates that the vector $\vec{G}_{p,hkl}$ has to fulfill two conditions. Firstly, it has to have the length $|\vec{G}_{p,hkl}|$ that was determined from the GIWAXS measurement. This is illustrated by the green dashed circle in figure C.1. Secondly, in order to fulfill equation C.4 the tip of $\vec{G}_{p,hkl}$ has to have a distance of $|\vec{G}_{p,00l}|$ from the tip of $\vec{G}_{p,0k0}$. This condition is illustrated by the blue dashed circle in figure C.1. As seen from the sketch, both conditions are fulfilled only at the intersects of the two circles. In general, both intersects represent valid solutions. However, the two resulting unit cells are simply mirror images of one another (mirrored at the q_x-$q-z$-plane). As seen from the sketch these two conditions clearly define the orientation of $\vec{G}_{p,hkl}$ and thus also the orientation of $\vec{G}_{p,00l}$. The azimuthal angle ϕ_{00l} can then be determine using the law of cosines:

$$\phi_{00l} = 180° - \arccos\left(\frac{|\vec{G}_{p,0k0}|^2 + |\vec{G}_{p,00l}|^2 - |\vec{G}_{p,hkl}|^2}{2 \cdot |\vec{G}_{p,0k0}| \cdot |\vec{G}_{p,00l}|}\right) \tag{C.5}$$

$$= 180° - \arccos\left(\frac{k^2 \cdot q_{p,010}^2 + l^2 \cdot q_{p,001}^2 - q_{p,hkl}^2}{2kl \cdot q_{p,010} \cdot q_{p,001}}\right) \tag{C.6}$$

The angle α^* of the reciprocal unit cell is then be determined from the dot product of $\vec{G}_{010}$ and $\vec{G}_{001}$.

$$\alpha^* = \arccos\left(\frac{\vec{G}_{0k0} \cdot \vec{G}_{00l}}{|\vec{G}_{0k0}| \cdot |\vec{G}_{00l}|}\right) \tag{C.7}$$

$$= \arccos\left(\frac{1}{|\vec{G}_{0k0}| \cdot |\vec{G}_{00l}|} \begin{pmatrix} |\vec{G}_{p,0k0}| \cos(\phi_{00l}) \\ |\vec{G}_{p,0k0}| \sin(\phi_{00l}) \\ G_{z,0k0} \end{pmatrix} \cdot \begin{pmatrix} |\vec{G}_{p,00l}| \\ 0 \\ G_{z,00l} \end{pmatrix}\right) \tag{C.8}$$

$$= \arccos\left(\frac{|\vec{G}_{p,0k0}| \cos(\phi_{00l}) \cdot |\vec{G}_{p,00l}| + G_{z,00l} \cdot G_{z,0k0}}{|\vec{G}_{0k0}| \cdot |\vec{G}_{00l}|}\right) \tag{C.9}$$

$$= \arccos\left(\frac{q_{p,010} \cos(\phi_{00l}) \cdot q_{p,001} + q_{z,001} \cdot q_{z,010}}{q_{010} \cdot q_{001}}\right) \tag{C.10}$$

D. Scattering Peak Positions of P3BrHT, P3CF$_3$HT and P3CNHT

Table D.1.: Peak positions of P3BrHT determined from WAXS and GIWAXS measurements on face-on oriented sample and peak positions calculated from the suggested unit cell: $a = 17.65\,\text{Å}$, $b = 7.78\,\text{Å}$, $c = 23.36\,\text{Å}$, $\alpha = \beta = \gamma = 90°$

Peak	WAXS	GIWAXS (face-on)			calculated (face-on)			
No.	$q[\text{Å}^{-1}]$	$q_p[\text{Å}^{-1}]$	$q_z\,[\text{Å}^{-1}]$	$\|q\|\,[\text{Å}^{-1}]$	$(h\ k\ l)$	$q_p[\text{Å}^{-1}]$	$q_z\,[\text{Å}^{-1}]$	$\|q\|\,[\text{Å}^{-1}]$
1	0.356	-	-	-	1 0 0	0.356	0.000	0.356
2	0.711	0.712	0.000	0.712	2 0 0	0.712	0.000	0.712
3	1.068	1.071	0.000	1.071	3 0 0	1.068	0.000	1.068
4	1.344	1.073*	0.814*	1.347*	2 1 3	1.076	0.808	1.346
5	1.565	1.332*	0.813*	1.560*	3 1 3	1.339	0.808	1.564
6	1.615	0.000*	1.628*	1.628*	0 2 0	0.000	1.616	1.616
7	1.654	0.347*	1.632*	1.668*	1 2 0	0.356	1.616	1.655
8	1.700	0.526*	1.627*	1.710*	0 2 2	0.538	1.616	1.703
9	1.767	0.711*	1.621*	1.770*	2 2 0	0.712	1.616	1.766
10	1.847	0.877	1.629	1.850	1 2 3	0.882	1.616	1.841

*Peak positions determined from measurements on thin films at an angle of incidence of $\alpha_i = 10°$ instead of measurements at $\alpha_i = 0.20°$ due to higher accuracy.

Table D.2.: Peak positions of P3CF₃HT determined from WAXS and GIWAXS measurements on face-on oriented sample and peak positions calculated from the suggested unit cell: $a = 17.26\,\text{Å}$, $b = 7.79\,\text{Å}$, $c = 7.89\,\text{Å}$, $\alpha = \beta = \gamma = 90°$

Peak	WAXS	GIWAXS (face-on)			calculated (face-on)			
No.	$q[\text{Å}^{-1}]$	$q_p[\text{Å}^{-1}]$	$q_z\,[\text{Å}^{-1}]$	$\|q\|\,[\text{Å}^{-1}]$	$(h\ k\ l)$	$q_p[\text{Å}^{-1}]$	$q_z\,[\text{Å}^{-1}]$	$\|q\|\,[\text{Å}^{-1}]$
1	0.364	0.368	0.000	0.368	1 0 0	0.364	0.000	0.364
2	0.728	0.739	0.000	0.739	2 0 0	0.728	0.000	0.728
3	1.092	1.098	0.000	1.098	3 0 0	1.092	0.000	1.092
4	1.347	1.062*	0.812*	1.337*	2 1 1	1.079	0.807	1.347
5	1.576	1.331*	0.812*	1.559*	3 1 1	1.351	0.807	1.574
6	1.613	0.000*	1.617*	1.617*	0 2 0	0.000	1.614	1.614
7	1.652	0.361*	1.617*	1.657*	1 2 0	0.364	1.614	1.655
8	1.773	0.721*	1.620*	1.773*	2 2 0	0.728	1.614	1.771
9	-	0.918	1.656	1.893	1 2 1	0.875	1.614	1.836
10	1.849	-	-	-	4 1 1	1.659	0.807	1.845
11	1.948	1.098	1.659	1.989	3 2 0	1.092	1.614	1.949

*Peak positions determined from measurements on thin films at an angle of incidence of $\alpha_i = 10°$ instead of measurements at $\alpha_i = 0.18°$ due to higher accuracy.

Table D.3.: Peak positions of P3CF$_3$HT determined from WAXS and GIWAXS measurements on edge-on oriented sample and peak positions calculated from the suggested unit cell: $a = 17.26$ Å, $b = 7.79$ Å, $c = 7.89$ Å, $\alpha = \beta = \gamma = 90°$

Peak	WAXS	GIWAXS (edge-on)			calculated (edge-on)			
No.	$q[\text{Å}^{-1}]$	$q_p[\text{Å}^{-1}]$	$q_z\,[\text{Å}^{-1}]$	$\lvert q\rvert\,[\text{Å}^{-1}]$	$(h\ k\ l)$	$q_p[\text{Å}^{-1}]$	$q_z\,[\text{Å}^{-1}]$	$\lvert q\rvert\,[\text{Å}^{-1}]$
1	0.364	0.000	0.376	0.376	1 0 0	0.000	0.364	0.364
2	0.728	0.000	0.750	0.750	2 0 0	0.000	0.728	0.728
3	1.092	0.000[*]	1.094[*]	1.094[*]	3 0 0	0.000	1.092	1.092
4	1.347	1.153	0.746	1.373	2 1 1	1.134	0.728	1.347
5	1.576	1.114[*]	1.102[*]	1.567[*]	3 1 1	1.134	1.092	1.574
6	1.613	0.000	1.630	1.630	0 2 0	1.614	0.000	1.614
7	1.652	0.367	1.627	1.668	1 2 0	1.614	0.364	1.655
8	1.773	1.632	0.7611	1.801	2 2 0	1.614	0.728	1.771
9	-	-	-	-	1 2 1	1.800	0.364	1.836
10	1.849	-	-	-	4 1 1	1.134	1.456	1.845
11	1.948	-	-	-	3 2 0	1.614	1.092	1.949

[*]Peak positions determined from measurements on thin films at an angle of incidence of $\alpha_i = 10°$ instead of measurements at $\alpha_i = 0.18°$ due to higher accuracy.

Table D.4.: Peak positions of P3CNHT determined from WAXS and GIWAXS measurements on face-on oriented sample and peak positions calculated from the suggested orthorhombic unit cell: $a = 18.16$ Å, $b = 7.51$ Å, $c = 8.60$ Å, $\alpha = \beta = \gamma = 90°$

Peak	WAXS	GIWAXS (face-on)			calculated (face-on)			
No.	$q[\text{Å}^{-1}]$	$q_p[\text{Å}^{-1}]$	$q_z\,[\text{Å}^{-1}]$	$\lvert q\rvert\,[\text{Å}^{-1}]$	$(h\ k\ l)$	$q_p[\text{Å}^{-1}]$	$q_z\,[\text{Å}^{-1}]$	$\lvert q\rvert\,[\text{Å}^{-1}]$
1	0.345	0.347	0.000	0.347	1 0 0	0.346	0.000	0.346
2	0.691	0.696	0.000	0.696	2 0 0	0.692	0.000	0.692
3	1.036	1.046	0.000	1.046	3 0 0	1.038	0.000	1.038
4	1.301[**]	0.983	0.864	1.309	2 1 1	1.007	0.837	1.309
5	1.674	0.000[*]	1.667[*]	1.667[*]	0 2 0	0.000	1.674	1.674
6	1.741[**]	-	-	1.735[*]	1 2 0	0.346	1.674	1.709
7	1.889[**]	0.889	1.665	1.888	1 2 1	0.809	1.674	1.859
					2 2 1	1.007	1.674	1.953

[*]Peak positions determined from measurements on thin films at an angle of incidence of $\alpha_i = 10°$ instead of measurements at $\alpha_i = 0.18°$ due to higher accuracy. [**] Peak positions determined manually instead of through peak fitting.

Table D.5.: Peak positions of P3CNHT determined from WAXS and GIWAXS measurements on face-on oriented sample and peak positions calculated from the suggested monoclinic unit cell: $a = 18.20\,\text{Å}$, $b = 7.53\,\text{Å}$, $c = 9.34\,\text{Å}$, $\alpha = \beta = 90°$, $\gamma = 86°$

Peak	WAXS	GIWAXS (face-on)			calculated (face-on)			
No.	$q[\text{Å}^{-1}]$	$q_p[\text{Å}^{-1}]$	$q_z\,[\text{Å}^{-1}]$	$\lvert q\rvert\,[\text{Å}^{-1}]$	$(h\ k\ l)$	$q_p[\text{Å}^{-1}]$	$q_z\,[\text{Å}^{-1}]$	$\lvert q\rvert\,[\text{Å}^{-1}]$
1	0.345	0.347	0.000	0.347	1 0 0	0.345	0.024	0.346
2	0.691	0.696	0.000	0.696	2 0 0	0.690	0.048	0.692
3	1.036	1.046	0.000	1.046	3 0 0	1.035	0.072	1.038
4	1.301**	0.983	0.864	1.309	$\bar{2}$ 1 1	0.964	0.885	1.309
5	1.674	0.000*	1.667*	1.667*	0 2 0	0.000	1.674	1.674
6	1.741**	-	-	1.735*	1 2 0	0.345	1.698	1.733
7	1.889**	0.889	1.665	1.888	2 2 1	0.964	1.626	1.890

*Peak positions determined from measurements on thin films at an angle of incidence of $\alpha_i = 10°$ instead of measurements at $\alpha_i = 0.18°$ due to higher accuracy. ** Peak positions determined manually instead of through peak fitting.

Table D.6.: Peak positions of P3CNHT determined from WAXS and GIWAXS measurements on face-on oriented sample and peak positions calculated from the suggested monoclinic unit cell: $a = 18.17\,\text{Å}$, $b = 7.51\,\text{Å}$, $c = 8.12\,\text{Å}$, $\alpha = \beta = 90°$, $\gamma = 87.9°$

Peak	WAXS	GIWAXS (face-on)			calculated (face-on)			
No.	$q[\text{Å}^{-1}]$	$q_p[\text{Å}^{-1}]$	$q_z\,[\text{Å}^{-1}]$	$\lvert q\rvert\,[\text{Å}^{-1}]$	$(h\ k\ l)$	$q_p[\text{Å}^{-1}]$	$q_z\,[\text{Å}^{-1}]$	$\lvert q\rvert\,[\text{Å}^{-1}]$
1	0.345	0.347	0.000	0.347	1 0 0	0.346	0.013	0.346
2	0.691	0.696	0.000	0.696	2 0 0	0.692	0.025	0.692
3	1.036	1.046	0.000	1.046	3 0 0	1.037	0.038	1.038
4	1.301**	0.983	0.864	1.309	3 1 1	1,037	0.799	1.309
5	1.674	0.000*	1.667*	1.667*	0 2 0	0.000	1.674	1.674
6	1.741**	-	-	1.735*	$\bar{1}$ 2 0	0.346	1.687	1.722
7	1.889**	0.889	1.665	1.888	$\bar{1}$ 2 1	0.848	1.687	1.888

*Peak positions determined from measurements on thin films at an angle of incidence of $\alpha_i = 10°$ instead of measurements at $\alpha_i = 0.18°$ due to higher accuracy. ** Peak positions determined manually instead of through peak fitting.

E. Scattering Peak Positions of the Investigated PDPPs

Table E.1.: Peak positions of PDPP[T]$_2$-T determined from WAXS and GIWAXS measurements

Peak	WAXS	GIWAXS			Indexing
No.	$q[\text{Å}^{-1}]$	$q_p[\text{Å}^{-1}]$	q_z $[\text{Å}^{-1}]$	$\lvert q \rvert$ $[\text{Å}^{-1}]$	$(h\ k\ l)$
1	0.322	0.000	0.339	0.339	1 0 0
2	0.647	0.000	0.673	0.673	2 0 0
3	0.972	0.000	1.006	1.006	3 0 0
4	≈ 1.30	0.000	1.331	1.331	4 0 0
5	1.605	1.635	0.000	1.635	0 1 0

Table E.2.: Peak positions of PDPP[T]$_2$-T$_{DEG}$ determined from WAXS and GIWAXS measurements.

Peak	WAXS	GIWAXS			Indexing
No.	$q[\text{Å}^{-1}]$	$q_p[\text{Å}^{-1}]$	q_z [Å^{-1}]	$\|q\|$ [Å^{-1}]	$(h\ k\ l)$
1	0.332	0.000	0.336	0.336	1 0 0
2	-	0.322	0.173	0.366	0 0 1
3	≈ 0.59	0.323	0.509	0.603	1 0 1
4	0.664	0.000	0.669	0.669	2 0 0
5	0.992	0.000	1.000	1.000	3 0 0
6	1.698	1.717	0.000	1.717	0 1 0

Table E.3.: Peak positions of PDPP[Py]$_2$-T determined from WAXS and GIWAXS measurements and peak positions calculated from the suggested unit cell: $a = 20.17\,\text{Å}$, $b = 5.46\,\text{Å}$, $c = 16.82\,\text{Å}$ $\alpha \approx 131.4°$, $\beta \approx 100.0°$, $\gamma \approx 97.0°$

Peak	WAXS	GIWAXS			Indexing	calculated		
No.	$q[\text{Å}^{-1}]$	$q_p[\text{Å}^{-1}]$	q_z [Å^{-1}]	$\|q\|$ [Å^{-1}]	$(h\ k\ l)$	$q_p[\text{Å}^{-1}]$	q_z [Å^{-1}]	$\|q\|$ [Å^{-1}]
1	0.334	0.000	0.342	0.342	1 0 0	0.000	0.334	0.334
2	0.530	0.502	0.183	0.534	0 0 1	0.498	0.181	0.530
3	0.669	0.000	0.677	0.677	2 0 0	0.000	0.668	0.668
4	-	0.501	0.516	0.719	1 0 1	0.498	0.515	0.717
5	-	0.539	0.800	0.965	2 0 1	0.498	0.849	0.985
6	1.000	0.000	1.023	1.023	3 0 0	0.000	1.002	1.002
7	1.164	-	-	-	1 $\bar{1}$ 2	1.151	0.177	1.165
8	1.267	1.255	0.000	1.255	0 $\bar{1}$ 3	1.247	0.024	1.247
9	-	0.573	1.131	1.268	-	-	-	-
10	-	0.250	1.277	1.301	-	-	-	-
11	1.337	0.000	1.354	1.354	4 0 0	0.000	1.336	1.336
12	1.555	1.544	0.162	1.552	$\bar{1}$ 1 0	1.534	0.185	1.546
13	1.620	1.542	0.522	1.628	0 1 0	1.534	0.519	1.620
14	1.732	1.534	0.852	1.755	1 1 0	1.534	0.853	1.756

Bibliography

[1] H. Shirakawa et al. "Synthesis of electrically conducting organic polymers: halogen derivatives of polyacetylene, (CH)". In: *Journal of the Chemical Society, Chemical Communications* (16 1977), pp. 578–580.

[2] A. Salleo. "Charge transport in polymeric transistors". In: *Materials Today* 10.3 (2007), pp. 38–45.

[3] H. Sirringhaus. "25th Anniversary Article: Organic Field-Effect Transistors: The Path Beyond Amorphous Silicon". In: *Advanced Materials* 26.9 (2014), pp. 1319–1335.

[4] J. Yang et al. "Insight into High-Performance Conjugated Polymers for Organic Field-Effect Transistors". In: *Chem* 4.12 (2018), pp. 2748–2785.

[5] R. S. Gurney, D. G. Lidzey, and T. Wang. "A review of non-fullerene polymer solar cells: from device physics to morphology control". In: *Reports on Progress in Physics* 82.3 (2019), p. 036601.

[6] X. Li et al. "Review and perspective of materials for flexible solar cells". In: *Materials Reports: Energy* 1.1 (2021), p. 100001.

[7] J. Rivnay et al. "Organic electrochemical transistors". In: *Nature Reviews Materials* 3.17086 (2018).

[8] P. Schmode et al. "High-Performance Organic Electrochemical Transistors Based on Conjugated Polyelectrolyte Copolymers". In: *Chemistry of Materials* 31.14 (2019), pp. 5286–5295.

[9] D. Kabra et al. "Efficient Single-Layer Polymer Light-Emitting Diodes". In: *Advanced Materials* 22.29 (2010), pp. 3194–3198.

[10] C. Sekine et al. "Recent progress of high performance polymer OLED and OPV materials for organic printed electronics". In: *Science and Technology of Advanced Materials* 15.3 (2014), p. 034203.

[11] M. Shin et al. "Highly Stretchable Polymer Transistors Consisting Entirely of Stretchable Device Components". In: *Advanced Materials* 26.22 (2014), pp. 3706–3711.

[12] A. Chortos, J. Liu, and Z. Bao. "Pursuing prosthetic electronic skin". In: *Nature Materials* 15.9 (2016), pp. 937–950.

[13] M. Ashizawa et al. "Intrinsically stretchable conjugated polymer semiconductors in field effect transistors". In: *Progress in Polymer Science* 100 (2020), p. 101181.

[14] U. Würfel et al. "Impact of charge transport on current–voltage characteristics and power-conversion efficiency of organic solar cells". In: *Nature Communications* 6.1 (2015), p. 6951.

[15] A. Spies et al. "Impact of Charge Carrier Mobility and Electrode Selectivity on the Performance of Organic Solar Cells". In: *Elementary Processes in Organic Photovoltaics*. Ed. by K. Leo. Cham: Springer International Publishing, 2017, pp. 401–418.

[16] R. Noriega et al. "A general relationship between disorder, aggregation and charge transport in conjugated polymers". In: *Nature Materials* 12.11 (2013), pp. 1038–1044.

[17] S. A. Mollinger et al. "Percolation, Tie-Molecules, and the Microstructural Determinants of Charge Transport in Semicrystalline Conjugated Polymers". In: *ACS Macro Letters* 4.7 (2015), pp. 708–712.

[18] K. Gu et al. "Assessing the Huang-Brown Description of Tie Chains for Charge Transport in Conjugated Polymers". In: *ACS Macro Letters* 7.11 (2018), pp. 1333–1338.

[19] H. Sirringhaus et al. "Two-dimensional charge transport in self-organized, high-mobility conjugated polymers". In: *Nature* 401.6754 (1999), pp. 685–688.

[20] M. L. Chabinyc et al. "X-ray Scattering Study of Thin Films of Poly(2,5-bis(3-alkylthiophen-2-yl)thieno[3,2-b]thiophene)". In: *Journal of the American Chemical Society* 129.11 (2007), pp. 3226–3237.

[21] J. Rivnay et al. "Unconventional Face-On Texture and Exceptional In-Plane Order of a High Mobility n-Type Polymer". In: *Advanced Materials* 22.39 (2010), pp. 4359–4363.

[22] H. Yang et al. "Molecular Packing and Orientation Transition of Crystalline Poly(2,5-dihexyloxy-p-phenylene)". In: *Macromolecular Chemistry and Physics* 215.5 (2014), pp. 405–411.

[23] M. Brinkmann et al. "Segregated versus Mixed Interchain Stacking in Highly Oriented Films of Naphthalene Diimide Bithiophene Copolymers". In: *ACS Nano* 6.11 (2012), pp. 10319–10326.

[24] C. Poelking and D. Andrienko. "Effect of Polymorphism, Regioregularity and Paracrystallinity on Charge Transport in Poly(3-hexylthiophene) [P3HT] Nanofibers". In: *Macromolecules* 46.22 (2013), pp. 8941–8956.

[25] Y. Olivier et al. "25th Anniversary Article: High-Mobility Hole and Electron Transport Conjugated Polymers: How Structure Defines Function". In: *Advanced Materials* 26.14 (2014), pp. 2119–2136.

[26] Y. Zhong et al. "Segregated versus Disordered Stacking in Two Low Bandgap Alternated Copolymers for Photovoltaic Applications: Impact of Polymorphism on Optical Properties". In: *Macromolecules* 51.11 (2018), pp. 4238–4249.

[27] S. Ludwigs. *P3HT Revisited - from Molecular Scale to Solar Cell Devices*. Berlin [u.a.]: Springer, 2014.

[28] A. T. Kleinschmidt, S. E. Root, and D. J. Lipomi. "Poly(3-hexylthiophene) (P3HT): fruit fly or outlier in organic solar cell research?" In: *J. Mater. Chem. A* 5 (23 2017), pp. 11396–11400.

[29] C. Yang et al. "Achieving over 10Organic Solar Cells via Solid Additives". In: *ChemSusChem* 14.17 (2021), pp. 3607–3613.

[30] C. Yang, S. Zhang, and J. Hou. "Low-cost and efficient organic solar cells based on polythiophene- and poly(thiophene vinylene)-related donors". In: *Aggregate* 3.3 (2022), e111.

[31] J. Balko et al. "Surface induced orientation and vertically layered morphology in thin films of poly(3-hexylthiophene) crystallized from the melt". In: *Journal of Materials Research* 32.10 (2017), pp. 1957–1968.

[32] V. Skrypnychuk et al. "Enhanced Vertical Charge Transport in a Semiconducting P3HT Thin Film on Single Layer Graphene". In: *Advanced Functional Materials* 25.5 (2015), pp. 664–670.

[33] N. Boulanger et al. "In situ probing of the crystallization kinetics of rr-P3HT on single layer graphene as a function of temperature". In: *Phys. Chem. Chem. Phys.* 19 (12 2017), pp. 8496–8503.

[34] O. Dolynchuk et al. "Elucidating the Effect of Interfacial Interactions on Crystal Orientations in Thin Films of Polythiophenes". In: *Macromolecules* 54.12 (2021), pp. 5429–5439.

[35] I. Kang et al. "Record High Hole Mobility in Polymer Semiconductors via Side-Chain Engineering". In: *Journal of the American Chemical Society* 135.40 (2013), pp. 14896–14899.

[36] J. Yao et al. "Significant Improvement of Semiconducting Performance of the Diketopyrrolopyrrole-Quaterthiophene Conjugated Polymer through Side-Chain Engineering via Hydrogen-Bonding". In: *Journal of the American Chemical Society* 138.1 (2016), pp. 173–185.

[37] H. J. Cheon, T. K. An, and Y.-H. Kim. "Diketopyrrolopyrrole (DPP)-Based Polymers and Their Organic Field-Effect Transistor Applications: A Review". In: *Macromolecular Research* 30.2 (2022), pp. 71–84.

[38] J. H. Kim et al. "Novel Polymer Nanowire Crystals of Diketopyrrolopyrrole-Based Copolymer with Excellent Charge Transport Properties". In: *Advanced Materials* 25.30 (2013), pp. 4102–4106.

[39] C. Xiao et al. "High Performance Polymer Nanowire Field-Effect Transistors with Distinct Molecular Orientations". In: *Advanced Materials* 27.34 (2015), pp. 4963–4968.

[40] A. Hoffmann, F. Brömmel, and H. Finkelmann. "Thermotropic Systems: Biaxial Nematic Polymers". In: *Biaxial Nematic Liquid Crystals*. John Wiley & Sons, Ltd, 2015. Chap. 13, pp. 319–331.

[41] D. R. Greer et al. "Liquid-Crystalline Phase Behavior in Polypeptoid Diblock Copolymers". In: *Macromolecules* 51.23 (2018), pp. 9519–9525.

[42] Z. Wu et al. "Temperature and Molecular Weight Dependent Hierarchical Equilibrium Structures in Semiconducting Poly(3-hexylthiophene)". In: *Macromolecules* 43.10 (2010), pp. 4646–4653.

[43] O. Herrmann-Schönherr et al. "Structure of an aromatic polyamide with disc-like mesogens in the main chain". In: *Die Makromolekulare Chemie, Rapid Communications* 7.12 (1986), pp. 791–796.

[44] M. Ebert et al. "Evidence for a biaxial nematic phase in sanidic aromatic polyamides with 1,4,7-trioxaoctyl side chains". In: *Die Makromolekulare Chemie, Rapid Communications* 9.6 (1988), pp. 445–451.

[45] M. Ebert et al. "Sanidics: A new class of mesophases, displayed by highly substituted rigid-rod polyesters and polyamides". In: *Liquid Crystals* 7.1 (1990), pp. 63–79.

[46] D. M. DeLongchamp et al. "Molecular Basis of Mesophase Ordering in a Thiophene-Based Copolymer". In: *Macromolecules* 41.15 (2008), pp. 5709–5715.

[47] P. Gemünden et al. "Nematic Ordering, Conjugation, and Density of States of Soluble Polymeric Semiconductors". In: *Macromolecules* 46.14 (2013), pp. 5762–5774.

[48] C. Greco et al. "Generic Model for Lamellar Self-Assembly in Conjugated Polymers: Linking Mesoscopic Morphology and Charge Transport in P3HT". In: *Macromolecules* 52.3 (2019), pp. 968–981.

[49] E. L. Wood et al. "Mesoscopic Modeling of a Highly-Ordered Sanidic Polymer Mesophase and Comparison With Experimental Data". In: *The Journal of Physical Chemistry B* 126.11 (2022), pp. 2285–2298.

[50] D. I. Bower. *An Introduction to Polymer Physics*. Cambridge University Press, 2002.

[51] G. Strobl. *The physics of polymers. Concepts for understanding their structures and behavior*. 3., rev. and expanded ed. Berlin [u.a.]: Springer, 2007, XIII, 518 S.

[52] U. W. Gedde and M. S. Hedenqvist. *Fundamental Polymer Science*. Cham: Springer Cham, 2019.

[53] M. Schulz et al. "The Underestimated Effect of Intracrystalline Chain Dynamics on the Morphology and Stability of Semicrystalline Polymers". In: *Macromolecules* 51.21 (2018), pp. 8377–8385.

[54] M. Schulz et al. "Competition between crystal growth and intracrystalline chain diffusion determines the lamellar thickness in semicrystalline polymers". In: *Nature Communications* 13.1 (2022), p. 119.

[55] D. A. Ivanov, Z. Amalou, and S. N. Magonov. "Real-Time Evolution of the Lamellar Organization of Poly(ethylene terephthalate) during Crystallization from the Melt: High-Temperature Atomic Force Microscopy Study". In: *Macromolecules* 34.26 (2001), pp. 8944–8952.

[56] B. Crist and J. M. Schultz. "Polymer spherulites: A critical review". In: *Progress in Polymer Science* 56 (2016), pp. 1–63.

[57] V. Skrypnychuk et al. "Ultrahigh Mobility in an Organic Semiconductor by Vertical Chain Alignment". In: *Advanced Materials* 28.12 (2016), pp. 2359–2366.

[58] E. J. W. Crossland et al. "Anisotropic Charge Transport in Spherulitic Poly(3-hexylthiophene) Films". In: *Advanced Materials* 24.6 (2012), pp. 839–844.

[59] Y. Yao et al. "Approaching Intra- and Interchain Charge Transport of Conjugated Polymers Facilely by Topochemical Polymerized Single Crystals". In: *Advanced Materials* 29.29 (2017), p. 1701251.

[60] I. Osaka and K. Takimiya. "Backbone orientation in semiconducting polymers". In: *Polymer* 59 (2015), A1–A15.

[61] V. Vohra and T. Anzai. "Molecular Orientation of Conjugated Polymer Chains in Nanostructures and Thin Films: Review of Processes and Application to Optoelectronics". In: *Journal of Nanomaterials* 2017.1 (2017), p. 3624750.

[62] I. Markov. *Crystal Growth for Beginners: Fundamentals of Nucleation, Crystal Growth and Epitaxy.* Singapore: World Scientific Publishing Co. Pte. Ltd., 2003.

[63] V. Kalikmanov. *Nucleation Theory.* Dordrecht: Springer Netherlands, 2013.

[64] O. Dolynchuk, M. Tariq, and T. Thurn-Albrecht. "Phenomenological Theory of First-Order Prefreezing". In: *J Phys Chem Lett* 10 (2019), pp. 1942–1946.

[65] V. P. Modak, B. E. Wyslouzil, and S. J. Singer. "Mechanism of surface freezing of alkanes". In: *The Journal of Chemical Physics* 153.22 (2020), p. 224501.

[66] A.-K. Flieger, M. Schulz, and T. Thurn-Albrecht. "Interface-Induced Crystallization of Polycaprolactone on Graphite via First-Order Prewetting of the Crystalline Phase". In: *Macromolecules* 51.1 (2018), pp. 189–194.

[67] X. Z. Wu et al. "Surface crystallization of liquid normal-alkanes". In: *Physical Review Letters* 70.7 (1993), pp. 958–961.

[68] B. Ocko et al. "Surface freezing in chain molecules: Normal alkanes". In: *Physical Review e* 55.3 (1997), pp. 3164–3182.

[69] O. Gang et al. "Surface freezing in chain molecules. II. Neat and hydrated alcohols". In: *Phys. Rev. E* 58 (5 1998), pp. 6086–6100.

[70] K. S. Gautam and A. Dhinojwala. "Melting at Alkyl Side Chain Comb Polymer Interfaces". In: *Phys. Rev. Lett.* 88 (14 2002), p. 145501.

[71]   K. Gautam et al. "Observation of novel liquid-crystalline phase above the bulk-melting temperature". In: *Physical Review Letters* 90.21 (2003), pp. 215501+.

[72]   S. Prasad, L. Hanne, and A. Dhinojwala. "Thermodynamic study of a novel surface ordered phase above the bulk melting temperature in alkyl side chain acrylate polymers". In: *Macromolecules* 38.7 (2005), pp. 2541–2543.

[73]   S. Prasad et al. "Partial Crystallinity in Alkyl Side Chain Polymers Dictates Surface Freezing". In: *Phys. Rev. Lett.* 101 (6 2008), p. 065505.

[74]   A. V. Tkachenko and Y. Rabin. "Fluctuation-Stabilized Surface Freezing of Chain Molecules". In: *Phys. Rev. Lett.* 76 (14 1996), pp. 2527–2530.

[75]   A. V. Tkachenko and Y. Rabin. "Theory of surface freezing of alkanes". In: *Phys. Rev. E* 55 (1 1997), pp. 778–784.

[76]   A. Tkachenko and Y. Rabin. "Tkachenko and Rabin Reply:" in: *Phys. Rev. Lett.* 79 (3 1997), pp. 532–532.

[77]   E. B. Sirota et al. "What Drives the Surface Freezing in Alkanes?" In: *Phys. Rev. Lett.* 79 (3 1997), pp. 531–531.

[78]   G. Hadziioannou G.;Malliaras, ed. *Semiconducting Polymers: Chemistry, Physics and Engineering.* Vol. 2. Weinheim: WILEY-VCH Verlag GmbH & Co. KGaA, 2007.

[79]   A. Heeger, N. Sariciftci, and E. Namdas. *Semiconducting and Metallic Polymers.* Oxford: Oxford University Press, 2010.

[80]   A. Mishra. "Interfacial Materials for Organic Solar Cells". In: *Solar Energy: Systems, Challenges, and Opportunities.* Ed. by H. Tyagi et al. Singapore: Springer Singapore, 2020, pp. 373–423.

[81]   J. T. Friedlein, R. R. McLeod, and J. Rivnay. "Device physics of organic electrochemical transistors". In: *Organic Electronics* 63 (2018), pp. 398–414.

[82]   L.-M. Chen et al. "Interface investigation and engineering – achieving high performance polymer photovoltaic devices". In: *J. Mater. Chem.* 20 (13 2010), pp. 2575–2598.

[83]   H. Ma et al. "Interface Engineering for Organic Electronics". In: *Advanced Functional Materials* 20.9 (2010), pp. 1371–1388.

[84]   V. Vohra et al. "Efficient inverted polymer solar cells employing favourable molecular orientation". In: *Nature Photonics* 9.6 (2015), pp. 403–408.

[85]   M. Saito, T. Koganezawa, and I. Osaka. "Correlation between Distribution of Polymer Orientation and Cell Structure in Organic Photovoltaics". In: *ACS Applied Materials & Interfaces* 10.38 (2018), pp. 32420–32425.

[86]   H. Hoppe and N. S. Sariciftci. "Organic solar cells: An overview". In: *Journal of Materials Research* 19.7 (2004), pp. 1924–1945.

[87]   J. Huang et al. "19.5via multifunctional interface engineering featuring radical scavenger". In: *Nature Communications* 15.1 (2024), p. 10565.

[88] R. Basu et al. "Large-area organic photovoltaic modules with 14.5world record efficiency". In: *Joule* 8.4 (2024), pp. 970–978.

[89] K. Liu et al. "Advances in flexible organic field-effect transistors and their applications for flexible electronics". In: *npj Flexible Electronics* 6.1 (2022), p. 1.

[90] B. D. Paulsen et al. "Organic mixed ionic-electronic conductors". In: *Nature Materials* 19.1 (2020), pp. 13–26.

[91] J. Rivnay et al. "High-performance transistors for bioelectronics through tuning of channel thickness". In: *Science Advances* 1.4 (2015), e1400251.

[92] S. Inal, G. G. Malliaras, and J. Rivnay. "Benchmarking organic mixed conductors for transistors". In: *Nature Communications* 8.1 (2017), p. 1767.

[93] D. Bernards and G. Malliaras. "Steady-State and Transient Behavior of Organic Electrochemical Transistors". In: *Advanced Functional Materials* 17.17 (2007), pp. 3538–3544.

[94] X. Strakosas, M. Bongo, and R. M. Owens. "The organic electrochemical transistor for biological applications". In: *Journal of Applied Polymer Science* 132.15 (2015).

[95] D. Khodagholy et al. "In vivo recordings of brain activity using organic transistors". In: *Nature Communications* 4.1 (2013), p. 1575.

[96] A. Williamson et al. "Localized Neuron Stimulation with Organic Electrochemical Transistors on Delaminating Depth Probes". In: *Advanced Materials* 27.30 (2015), pp. 4405–4410.

[97] P.-O. Svensson et al. "A sensor circuit using reference-based conductance switching in organic electrochemical transistors". In: *Applied Physics Letters* 93.20 (2008), p. 203301.

[98] Z. Mousavi et al. "Ion-Selective Organic Electrochemical Junction Transistors Based on Poly(3,4-ethylenedioxythiophene) Doped with Poly(styrene sulfonate)". In: *Electroanalysis* 21.3-5 (2009), pp. 472–479.

[99] C. Liao et al. "Flexible Organic Electrochemical Transistors for Highly Selective Enzyme Biosensors and Used for Saliva Testing". In: *Advanced Materials* 27.4 (2015), pp. 676–681.

[100] Z.-T. Zhu et al. "A simple poly(3,4-ethylene dioxythiophene)/poly(styrene sulfonic acid) transistor for glucose sensing at neutral pH". In: *Chem. Commun.* (13 2004), pp. 1556–1557.

[101] C. Liao et al. "Highly selective and sensitive glucose sensors based on organic electrochemical transistors with graphene-modified gate electrodes". In: *J. Mater. Chem. B* 1 (31 2013), pp. 3820–3829.

[102] P. Lin et al. "Organic Electrochemical Transistors Integrated in Flexible Microfluidic Systems and Used for Label-Free DNA Sensing". In: *Advanced Materials* 23.35 (2011), pp. 4035–4040.

[103] B. Wunderlich. *Thermal analysis of polymeric materials*. Berlin: Springer, 2005.

[104] G. Höhne, W. Hemminger, and H. Flammersheim. *Differential Scanning Calorimetry*. 2nd ed. Berlin: Springer, 2003.

[105] P. C. Robinson and S. Bradbury. *Qualitative Polarized-Light Microscopy*. Oxford: Oxford University Press, 1992.

[106] L. C. Sawyer, D. T. Grubb, and G. F. Meyers. *Polymer Microscopy*. 3rd ed. New York, NY: Springer New York, 2008, pp. 1–539.

[107] R. Reifenberger. *Fundamentals of Atomic Force Microscopy*. WORLD SCIENTIFIC, 2015.

[108] P. Eaton and P. West. *Atomic Force Microscopy*. Oxford: Oxford University Press, 2010.

[109] P. Trtik, J. Kaufmann, and U. Volz. "On the use of peak-force tapping atomic force microscopy for quantification of the local elastic modulus in hardened cement paste". In: *Cement and Concrete Research* 42.1 (2012), pp. 215–221.

[110] B. Pittenger, N. Erina, and C. su. "Quantitative mechanical property mapping at the nanoscale with PeakForce QNM". In: *Bruker Application Note* 128 (2010).

[111] S. B. Kaemmer. "Introduction to Bruker's ScanAsyst and PeakForce Tapping AFM Technology". In: *Bruker Application Note* 133 (2011).

[112] D. Nečas and P. Klapetek. "Gwyddion: an open-source software for SPM data analysis". In: *Open Physics* 10.1 (2012), pp. 181–188.

[113] R. Roe. *Methods of X-ray and neutron scattering in polymer science / Ryong-Joon Roe*. Topics in polymer science. New York: Oxford Univ. Press, 2000.

[114] M. Birkholz. *Thin film analysis by x-ray scattering*. Weinheim: Wiley-VCH Verlag GmbH & Co. KGaA, 2006.

[115] D. Als-Nielsen Jens; McMorrow. "X-rays and their interaction with matter". In: *Elements of Modern X-ray Physics*. John Wiley & Sons Ltd., 2011.

[116] C. Dong and J. I. Langford. " LAPODS: a computer program for refinement of lattice parameters using optimal regression". In: *Journal of Applied Crystallography* 33.4 (2000), pp. 1177–1179.

[117] A. A. Coelho. "Indexing of powder diffraction patterns by iterative use of singular value decomposition". In: *Journal of Applied Crystallography* 36.1 (2003), pp. 86–95.

[118] M. Tolan. *X-Ray Scattering from Soft-Matter Thin Films : Materials Science and Basic Research*. Springer tracts in modern physics: 148. Springer, 1999.

[119] E. Schäfer. *Technische Optik*. Technischen Optik: Mathematische und Physikalische Grundlagen. Wiesbaden: Vieweg+Teubner Verlag, 1997.

[120] L. Hartmann et al. "2D Versus 3D Crystalline Order in Thin Films of Regioregular Poly(3-hexylthiophene) Oriented by Mechanical Rubbing and Epitaxy". In: *Advanced Functional Materials* 21.21 (2011), pp. 4047–4057.

[121] B. T. O'Connor et al. "Morphological Origin of Charge Transport Anisotropy in Aligned Polythiophene Thin Films". In: *Advanced Functional Materials* 24.22 (2014), pp. 3422–3431.

[122] Y. Yang et al. "Nanoimprinted Polymer Solar Cell". In: *ACS Nano* 6.4 (2012), pp. 2877–2892.

[123] Y. Yang et al. "Effects of nanostructure geometry on nanoimprinted polymer photovoltaics". In: *Nanoscale* 6 (13 2014), pp. 7576–7584.

[124] G. Derue et al. "Nanorubbing of Polythiophene Surfaces". In: *Journal of the American Chemical Society* 127.22 (2005), pp. 8018–8019.

[125] B. O'Connor et al. "Anisotropic Structure and Charge Transport in Highly Strain-Aligned Regioregular Poly(3-hexylthiophene)". In: *Advanced Functional Materials* 21.19 (2011), pp. 3697–3705.

[126] D. Gargi et al. "Charge Transport in Highly Face-On Poly(3-hexylthiophene) Films". In: *The Journal of Physical Chemistry C* 117.34 (2013), pp. 17421–17428.

[127] N. Shioya et al. "Controlling Mechanism of Molecular Orientation of Poly(3-alkylthiophene) in a Thin Film Revealed by Using pMAIRS". In: *Macromolecules* 50.13 (2017), pp. 5090–5097.

[128] E. Mena-Osteritz et al. "Two-Dimensional Crystals of Poly(3-Alkyl- thiophene)s: Direct Visualization of Polymer Folds in Submolecular Resolution". In: *Angewandte Chemie International Edition* 39.15 (2000), pp. 2679–2684.

[129] D. H. Kim et al. "Graphene surface induced specific self-assembly of poly(3-hexylthiophene) for nanohybrid optoelectronics: from first-principles calculation to experimental characterizations". In: *Soft Matter* 9 (22 2013), pp. 5355–5360.

[130] V. Skrypnychuk et al. "Reduced crystallinity and enhanced charge transport by melt annealing of an organic semiconductor on single layer graphene". In: *J. Mater. Chem. C* 4 (19 2016), pp. 4143–4149.

[131] S. Chae et al. "Favorable Face-on Orientation of a Conjugated Polymer on Roll-to-Roll-Transferred Graphene Interface". In: *Advanced Materials Interfaces* 4.23 (2017), p. 1701099.

[132] Y. Y. Yimer, A. Dhinojwala, and M. Tsige. "Interfacial properties of free-standing poly(3-hexylthiophene) films". In: *The Journal of Chemical Physics* 137.4 (2012), p. 044703.

[133] Y. Sun et al. "Improved thin film morphology and bulk-heterojunction solar cell performance through systematic tuning of the surface energy of conjugated polymers". In: *J. Mater. Chem.* 22 (12 2012), pp. 5587–5595.

[134] J. B. Howard et al. "Fine Tuning Surface Energy of Poly(3-hexylthiophene) by Heteroatom Modification of the Alkyl Side Chains". In: *ACS Macro Letters* 4.7 (2015), pp. 725–730.

[135] A. Schmitt, S. Samal, and B. C. Thompson. "Tuning the surface energies in a family of poly-3-alkylthiophenes bearing hydrophilic side-chains synthesized via direct arylation polymerization (DArP)". In: *Polym. Chem.* 12 (19 2021), pp. 2840–2847.

[136] A. J. Much. "Crystal Orientation in Thin Films of Poly-(3- (6 -trifluorohexyl)thiophene) Crystallised on Silicon and Graphene Substrates". Thesis. 2023.

[137] A. Averkova. "Molekulare Orientierung in dünnen Filmen von Poly[3-(6-cyanohexyl) thiophene] auf Si". Thesis. 2021.

[138] O. Dolynchuk et al. "Controlling Crystal Orientation in Films of Conjugated Polymers by Tuning the Surface Energy". In: *Macromolecules* 57.21 (2024), pp. 10399–10409.

[139] J. Balko et al. "Determination of the Crystallinity of Semicrystalline Poly(3-hexylthiophene) by Means of Wide-Angle X-ray Scattering". In: *Macromolecules* 46.24 (2013), pp. 9642–9651.

[140] *NIST Computational Chemistry Comparison and Benchmark Database.*

[141] P. Schmode et al. "Influence of ω-Bromo Substitution on Structure and Optoelectronic Properties of Homopolymers and Gradient Copolymers of 3-Hexylthiophene". In: *Macromolecules* 53.7 (2020), pp. 2474–2484.

[142] T. J. Prosa et al. "X-ray structural studies of poly(3-alkylthiophenes): an example of an inverse comb". In: *Macromolecules* 25.17 (1992), pp. 4364–4372.

[143] K. Tashiro et al. "Crystal structural change in poly(3-alkyl thiophene)s induced by iodine doping as studied by an organized combination of X-ray diffraction, infrared/Raman spectroscopy and computer simulation techniques". In: *Polymer* 38.12 (1997), pp. 2867–2879.

[144] N. Kayunkid, S. Uttiya, and M. Brinkmann. "Structural Model of Regioregular Poly(3-hexylthiophene) Obtained by Electron Diffraction Analysis". In: *Macromolecules* 43.11 (2010), pp. 4961–4967.

[145] S. Joshi, S. Grigorian, and U. Pietsch. "X-ray structural and crystallinity studies of low and high molecular weight poly(3-hexylthiophene)". In: *physica status solidi (a)* 205.3 (2008), pp. 488–496.

[146] S. Joshi et al. "Thickness Dependence of the Crystalline Structure and Hole Mobility in Thin Films of Low Molecular Weight Poly(3-hexylthiophene)". In: *Macromolecules* 41.18 (2008), pp. 6800–6808.

[147] S. Joshi et al. "Bimodal Temperature Behavior of Structure and Mobility in High Molecular Weight P3HT Thin Films". In: *Macromolecules* 42.13 (2009), pp. 4651–4660.

[148] M. Brinkmann. "Structure and morphology control in thin films of regioregular poly(3-hexylthiophene)". In: *Journal of Polymer Science Part B: Polymer Physics* 49.17 (2011), pp. 1218–1233.

[149] S. Thankaraj Salammal et al. "Influence of alkyl side chain length on the in-plane stacking of room temperature and low temperature cast poly(3-alkylthiophene) thin films". In: *European Polymer Journal* 67 (2015), pp. 199–212.

[150] D. Dudenko et al. "A Strategy for Revealing the Packing in Semicrystalline π-Conjugated Polymers: Crystal Structure of Bulk Poly-3-hexyl-thiophene (P3HT)". In: *Angewandte Chemie International Edition* 51.44 (2012), pp. 11068–11072.

[151] A.-K. Löhmann, T. Henze, and T. Thurn-Albrecht. "Direct observation of prefreezing at the interface melt–solid in polymer crystallization". In: *Proceedings of the National Academy of Sciences* 111.49 (2014), pp. 17368–17372.

[152] M. Tariq, O. Dolynchuk, and T. Thurn-Albrecht. "Effect of Substrate Interaction on Thermodynamics of Prefreezing". In: *Macromolecules* 52.23 (2019), pp. 9140–9148.

[153] E. F. Hare and W. A. Zisman. "Autophobic Liquids and the Properties of their Adsorbed Films". In: *The Journal of Physical Chemistry* 59.4 (1955), pp. 335–340.

[154] K. J. Ihn, J. Moulton, and P. Smith. "Whiskers of poly(3-alkylthiophene)s". In: *Journal of Polymer Science Part B: Polymer Physics* 31.6 (1993), pp. 735–742.

[155] H. Yang et al. "Effect of mesoscale crystalline structure on the field-effect mobility of regioregular poly(3-hexyl thiophene) in thin-film transistors". In: *Advanced Functional Materials* 15.4 (2005), pp. 671–676.

[156] G. Reiter and J.-U. Sommer. "Crystallization of Adsorbed Polymer Monolayers". In: *Phys. Rev. Lett.* 80 (17 1998), pp. 3771–3774.

[157] A. Sharma and R. Khanna. "Pattern formation in unstable thin liquid films under the influence of antagonistic short- and long-range forces". In: *The Journal of Chemical Physics* 110.10 (1999), pp. 4929–4936.

[158] G. Reiter. "Model experiments for a molecular understanding of polymer crystallization". In: *Journal of Polymer Science Part B: Polymer Physics* 41.16 (2003), pp. 1869–1877.

[159] V. H. Mareau and R. E. Prud'homme. "In-Situ Hot Stage Atomic Force Microscopy Study of Poly(ε-caprolactone) Crystal Growth in Ultrathin Films". In: *Macromolecules* 38.2 (2005), pp. 398–408.

[160] V. H. Mareau and R. E. Prud'homme. "Crystallization of ultrathin poly(ε-caprolactone) films in the presence of residual solvent, an in situ atomic force microscopy study". In: *Polymer* 46.18 (2005), pp. 7255–7265.

[161] Z. Ma et al. "Fractal crystal growth of poly(ethylene oxide) crystals from its amorphous monolayers". In: *Polymer* 49.6 (2008), pp. 1629–1634.

[162] C. Guo and H. Huo. "Poor solvent as a nucleating agent to induce poly(ε-caprolactone) ultrathin film crystallization on poly(vinylpyrrolidone) substrate". In: *Colloid and Polymer Science* 294.4 (2016), pp. 767–776.

[163] E. Brener, H. Müller-Krumbhaar, and D. Temkin. "Structure formation and the morphology diagram of possible structures in two-dimensional diffusional growth". In: *Phys. Rev. E* 54 (3 1996), pp. 2714–2722.

[164] J.-U. Sommer and G. Reiter. "Polymer crystallization in quasi-two dimensions. II. Kinetic models and computer simulations". In: *The Journal of Chemical Physics* 112.9 (2000), pp. 4384–4393.

[165] G. Reiter et al. "Morphologies of Polymer Crystals in Thin Films". In: *Progress in Understanding of Polymer Crystallization*. Ed. by G. Reiter and G. R. Strobl. Berlin, Heidelberg: Springer Berlin Heidelberg, 2007, pp. 179–200.

[166] G.-l. Zhang et al. "Molecular weight dependence of crystal pattern transitions of poly(ethylene oxide)". In: *Chinese Journal of Polymer Science* 31.5 (2013), pp. 798–808.

[167] Y. Jiang et al. "Lamellar Branching of Poly(bisphenol A-co-decane) Spherulites at Different Temperatures Studied by High-Temperature AFM". In: *Macromolecules* 36.10 (2003), pp. 3652–3655.

[168] C.-M. Chan and L. Li. "Direct Observation of the Growth of Lamellae and Spherulites by AFM". In: *Intrinsic Molecular Mobility and Toughness of Polymers II*. Ed. by H.-H. Kausch. Berlin, Heidelberg: Springer Berlin Heidelberg, 2005, pp. 1–41.

[169] R. Pearce and G. J. Vancso. "Imaging of Melting and Crystallization of Poly(ethylene oxide) in Real-Time by Hot-Stage Atomic Force Microscopy". In: *Macromolecules* 30.19 (1997), pp. 5843–5848.

[170] K. Taguchi, Y. Miyamoto, and A. Toda. "Molecular Weight Dependence of Crystal Growth in Isotactic Polystyrene Ultrathin Films". In: *ACS Macro Letters* 8.10 (2019), pp. 1227–1232.

[171] S. Majumder et al. "Growth Kinetics of Stacks of Lamellar Polymer Crystals". In: *Macromolecules* 51.21 (2018), pp. 8738–8745.

[172] B. Li et al. "Relaxation behavior of polymer thin films: Effects of free surface, buried interface, and geometrical confinement". In: *Progress in Polymer Science* 120 (2021), p. 101431.

[173] M. Tariq, T. Thurn-Albrecht, and O. Dolynchuk. "Heterogeneous Crystal Nucleation from the Melt in Polyethylene Oxide Droplets on Graphite: Kinetics and Microscopic Structure". In: *Crystals* 11.8 (2021).

[174] M. Tariq, O. Dolynchuk, and T. Thurn-Albrecht. "Independent Variation of Transition Temperature and Prefrozen Layer Thickness at the Prefreezing Transition". In: *The Journal of Physical Chemistry C* 124.48 (2020), 26184–26192.

[175] Y. Qiu and V. Molinero. "Strength of Alkane–Fluid Attraction Determines the Interfacial Orientation of Liquid Alkanes and Their Crystallization through Heterogeneous or Homogeneous Mechanisms". In: *Crystals* 7.3 (2017).

[176] J. C. Brendel et al. "Controlled Synthesis of Water-Soluble Conjugated Polyelectrolytes Leading to Excellent Hole Transport Mobility". In: *Chemistry of Materials* 26.6 (2014), pp. 1992–1998.

[177] M. M. Schmidt et al. "Smaller Counter Cation for Higher Transconductance in Anionic Conjugated Polyelectrolytes". In: *Macromolecular Chemistry and Physics* 219.2 (2018), p. 1700374.

[178] A. Giovannitti et al. "Controlling the mode of operation of organic transistors through side-chain engineering". In: *Proceedings of the National Academy of Sciences* 113.43 (2016), pp. 12017–12022.

[179] A. Giovannitti et al. "The Role of the Side Chain on the Performance of N-type Conjugated Polymers in Aqueous Electrolytes". In: *Chemistry of Materials* 30.9 (2018), pp. 2945–2953.

[180] S. Inal et al. "Conjugated Polymers in Bioelectronics". In: *Accounts of Chemical Research* 51.6 (2018), pp. 1368–1376.

[181] H. Zhao et al. "Oligoethylene-Glycol-Functionalized Polyoxythiophenes for Cell Engineering: Syntheses, Characterizations, and Cell Compatibilities". In: *ACS Applied Materials & Interfaces* 4.2 (2012), pp. 680–686.

[182] A. Yokoyama, R. Miyakoshi, and T. Yokozawa. "Chain-Growth Polymerization for Poly(3-hexylthiophene) with a Defined Molecular Weight and a Low Polydispersity". In: *Macromolecules* 37.4 (2004), pp. 1169–1171.

[183] M. C. Iovu et al. "Experimental Evidence for the Quasi-"Living" Nature of the Grignard Metathesis Method for the Synthesis of Regioregular Poly(3-alkylthiophenes)". In: *Macromolecules* 38.21 (2005), pp. 8649–8656.

[184] R. H. Lohwasser and M. Thelakkat. "Toward Perfect Control of End Groups and Polydispersity in Poly(3-hexylthiophene) via Catalyst Transfer Polymerization". In: *Macromolecules* 44.9 (2011), pp. 3388–3397.

[185] C. Cendra et al. "Role of the Anion on the Transport and Structure of Organic Mixed Conductors". In: *Advanced Functional Materials* 29.5 (2019), p. 1807034.

[186] A. Savva et al. "Influence of Water on the Performance of Organic Electrochemical Transistors". In: *Chemistry of Materials* 31.3 (2019), pp. 927–937.

[187] B. X. Dong et al. "Influence of Side-Chain Chemistry on Structure and Ionic Conduction Characteristics of Polythiophene Derivatives: A Computational and Experimental Study". In: *Chemistry of Materials* 31.4 (2019), pp. 1418–1429.

[188] L. Q. Flagg et al. "Polymer Crystallinity Controls Water Uptake in Glycol Side-Chain Polymer Organic Electrochemical Transistors". In: *Journal of the American Chemical Society* 141.10 (2019), pp. 4345–4354.

[189] P. Schmode et al. "The Key Role of Side Chain Linkage in Structure Formation and Mixed Conduction of Ethylene Glycol Substituted Polythiophenes". In: *ACS Applied Materials & Interfaces* 12.11 (2020), pp. 13029–13039.

[190] E. Verploegen et al. "Effects of Thermal Annealing Upon the Morphology of Polymer–Fullerene Blends". In: *Advanced Functional Materials* 20.20 (2010), pp. 3519–3529.

[191] J. Rivnay et al. "Drastic Control of Texture in a High Performance n-Type Polymeric Semiconductor and Implications for Charge Transport". In: *Macromolecules* 44.13 (2011), pp. 5246–5255.

[192] D. Johannsmann. *The Quartz Crystal Microbalance in Soft Matter Research: Fundamentals and Modeling.* Cham: Springer International Publishing, 2015.

[193] M. V. Voinova et al. "Viscoelastic Acoustic Response of Layered Polymer Films at Fluid-Solid Interfaces: Continuum Mechanics Approach". In: *Physica Scripta* 59.5 (1999), p. 391.

[194] M. ElMahmoudy et al. "Tailoring the Electrochemical and Mechanical Properties of PEDOT:PSS Films for Bioelectronics". In: *Macromolecular Materials and Engineering* 302.5 (2017), p. 1600497.

[195] J. E. B. Randles. "Kinetics of rapid electrode reactions". In: *Discuss. Faraday Soc.* 1 (0 1947), pp. 11–19.

[196] W. Choi et al. "Modeling and Applications of Electrochemical Impedance Spectroscopy (EIS) for Lithium-ion Batteries". In: *J. Electrochem. Sci. Technol* 11.1 (2020), pp. 1–13.

[197] M. Moser et al. "Ethylene Glycol-Based Side Chain Length Engineering in Polythiophenes and its Impact on Organic Electrochemical Transistor Performance". In: *Chemistry of Materials* 32.15 (2020), pp. 6618–6628.

[198] P. Sivaraman et al. "Effect of regioregularity on specific capacitance of poly(3-hexylthiophene)". In: *Electrochimica Acta* 69 (2012), pp. 134–138.

[199] C. M. Proctor, J. Rivnay, and G. G. Malliaras. "Understanding volumetric capacitance in conducting polymers". In: *Journal of Polymer Science Part B: Polymer Physics* 54.15 (2016), pp. 1433–1436.

[200] Z. Bao, A. Dodabalapur, and A. J. Lovinger. "Soluble and processable regioregular poly(3-hexylthiophene) for thin film field-effect transistor applications with high mobility". In: *Applied Physics Letters* 69.26 (1996), pp. 4108–4110.

[201] J.-F. Chang et al. "Enhanced Mobility of Poly(3-hexylthiophene) Transistors by Spin-Coating from High-Boiling-Point Solvents". In: *Chem. Mater.* 16.23 (2004), pp. 4772–4776.

[202] C. D. Heinrich and M. Thelakkat. "Poly-(3-hexylthiophene) bottlebrush copolymers with tailored side-chain lengths and high charge carrier mobilities". In: *J. Mater. Chem. C* 4 (23 2016), pp. 5370–5378.

[203] P. A. Finn et al. "Effect of polar side chains on neutral and p-doped polythiophene". In: *J. Mater. Chem. C* 8 (45 2020), pp. 16216–16223.

[204] H. Yu et al. "The Influence of Alkyl Spacers and Molecular Weight on the Charge Transport and Storage Properties of Oxy-Bithiophene-Based Conjugated Polymers". In: *Angewandte Chemie International Edition* 64.6 (2025), e202417897.

[205] J. Mei et al. "Siloxane-Terminated Solubilizing Side Chains: Bringing Conjugated Polymer Backbones Closer and Boosting Hole Mobilities in Thin-Film Transistors". In: *Journal of the American Chemical Society* 133.50 (2011), pp. 20130–20133.

[206] C. R. Singh et al. "Correlation of charge transport with structural order in highly ordered melt-crystallized poly(3-hexylthiophene) thin films". In: *Journal of Polymer Science Part B: Polymer Physics* 51.12 (2013), pp. 943–951.

[207] K. H. Hendriks et al. "Band Gap Control in Diketopyrrolopyrrole-Based Polymer Solar Cells Using Electron Donating Side Chains". In: *Advanced Energy Materials* 3.5 (2013), pp. 674–679.

[208] M.-F. Falzon et al. "Diketopyrrolopyrrole-based acceptor polymers for photovoltaic application". In: *Physical Chemistry Chemical Physics* 13.19 (2011), pp. 8931–8939.

[209] C. J. Mueller et al. "High Bulk Electron Mobility Diketopyrrolopyrrole Copolymers with Perfluorothiophene". In: *Advanced Functional Materials* 25.18 (2015), pp. 2725–2736.

[210] C. J. Mueller et al. "Control of Molecular Orientation in Polydiketopyrrolopyrrole Copolymers via Diffusive Noncovalent Interactions". In: *Chemistry of Materials* 28.19 (2016), pp. 7088–7097.

[211] C. Mueller, C. Singh, and M. Thelakkat. "EDOT-diketopyrrolopyrrole copolymers for high bulk hole mobility and near infrared absorption". In: *Journal of Polymer Science Part B-Polymer Physics* 54.6 (2016), pp. 639–648.

[212] G. Krauss et al. "Polydiketopyrrolopyrroles Carrying Ethylene Glycol Substituents as Efficient Mixed Ion-Electron Conductors for Biocompatible Organic Electrochemical Transistors". In: *Advanced Functional Materials* 31.20 (2021), p. 2010048.

[213] R. T. Kahl et al. "Effect of Chemical Modification on Molecular Ordering in Polydiketopyrrolopyrrole Copolymers: From Liquid Crystalline to Crystalline". In: *Macromolecules* 57.11 (2024), pp. 5243–5252.

[214] P. Dhar et al. "Annealing-Induced Changes in the Molecular Orientation of Poly-3-hexylthiophene at Buried Interfaces". In: *The Journal of Physical Chemistry C* 117.29 (2013), pp. 15213–15220.

[215] S. Y. Son et al. "Control of Crystallite Orientation in Diketopyrrolopyrrole-Based Semiconducting Polymers via Tuning of Intermolecular Interactions". In: *ACS Applied Materials & Interfaces* 11.11 (2019), pp. 10751–10757.

[216] S. Y. Son, T. Park, and W. You. "Understanding of Face-On Crystallites Transitioning to Edge-On Crystallites in Thiophene-Based Conjugated Polymers". In: *Chemistry of Materials* 33.12 (2021), pp. 4541–4550.

[217]   M. Brinkmann et al. "Highly Oriented and Nanotextured Films of Regioregular Poly(3-hexylthiophene) Grown by Epitaxy on the Nanostructured Surface of an Aromatic Substrate". In: *Macromolecules* 43.18 (2010), pp. 7604–7610.

[218]   S. Zhang et al. "Molecular Origin of Strain-Induced Chain Alignment in PDPP-Based Semiconducting Polymeric Thin Films". In: *Advanced Functional Materials* 31.21 (2021), p. 2100161.

[219]   Y. Yoneda. "Anomalous Surface Reflection of X Rays". In: *Physical Review* 131.5 (1963), p. 2010.

Publications

1. P. Schmode, A.Savva, R. Kahl, D. Ohayon, F. Meichsner, O. Dolynchuk, T. Thurn-Albrecht, S. Inal, M. Thelakkat: "The Key Role of Side Chain Linkage in Structure Formation and Mixed Conduction of Ethylene Glycol Substituted Polythiophenes". In: *ACS Applied Materials & Interfaces* 12.11 (2020), pp. 13029-13039.

2. R. T. Kahl, A. Erhardt, G. Krauss, F. Seibold, O. Dolynchuk, M. Thelakkat, T. Thurn-Albrecht: "Effect of Chemical Modification on Molecular Ordering in Polydiketopyrrolopyrrole Copolymers: From Liquid Crystalline to Crystalline". In: *Macromolecules* 57.11 (2024), pp. 5243-5252.

3. O. Dolynchuk, R. T. Kahl, F. Meichsner, A.J. Much, A. Pechevystyi, A. Averkova, A. Erhardt, M. Thelakkat, T. Thurn-Albrecht: "Controlling Crystal Orientation in Films of Conjugated Polymers by Tuning the Surface Energy". In: *Macromolecules* 57.21 (2024), pp. 10399-10409.

Eidesstattliche Erklärung

Hiermit versichere ich, dass ich die vorliegende Arbeit selbstständig und ohne Benutzung anderer als der im beigefügten Literaturverzeichnis angegebenen Hilfsmittel angefertigt habe. Alle Stellen, die wörtlich oder sinngemäß aus Veröffentlichungen entnommen wurden, sind als solche kenntlich gemacht.

Ferner habe ich nicht versucht, anderweitig mit oder ohne Erfolg eine Dissertation einzureichen oder mich einer Doktorprüfung zu unterziehen.

Halle(Saale), 01. Juli 2025

_____   _____
Ort, Datum   Unterschrift

Curriculum Vitae

Personal Data

Name:	Robert Thomas Kahl
Date of Birth:	-
Place of Birth:	-
Sex:	male
Nationality:	german

Eductaion

Since 03/2019	Ph.D. at Institute of Physics Martin Luther University Halle-Wittenberg (Supervised by Prof. Dr. Thomas Thurn-Albrecht) Halle (Saale), Germany
10/2014 - 11/2018	Medical Physics (Master of Science) Martin Luther University Halle-Wittenberg Halle (Saale), Germany
10/2011 - 09/2014	Medical Engineering Science (Bachelor of Science) Univertsity of Lübeck Lübeck, Germany

There are no previous convictions and no preliminary investigation has been initiated.

Halle(Saale), 01. Juli 2025 2025

_____   _____
Ort, Datum   Unterschrift

Acknowledgement